UC Riverside

UC Riverside Electronic Theses and Dissertations

Title

Interfacial Design and Modification for Next-Generation Lithium-Ion Batteries

Permalink

https://escholarship.org/uc/item/6d57k4tw

Author

Shang, Ruoxu

Publication Date

2024

Peer reviewed|Thesis/dissertation

eScholarship.org Powered by the California Digital Library
University of California

UNIVERSITY OF CALIFORNIA
RIVERSIDE

Interfacial Design and Modification for Next-Generation Lithium-Ion Batteries

A Dissertation submitted in partial satisfaction
of the requirements for the degree of

Doctor of Philosophy

in

Materials Science and Engineering

by

Ruoxu Shang

September 2024

Dissertation Committee:
Dr. Cengiz S. Ozkan, Co-Chairperson
Dr. Mihrimah Ozkan, Co-Chairperson
Dr. Kambiz Vafai
Dr. Guanshui Xu

Copyright by
Ruoxu Shang
2024

The Dissertation of Ruoxu Shang is approved:

_____

_____

_____

Committee Co-Chairperson

_____

Committee Co-Chairperson

University of California, Riverside

Acknowledgements

I would like to thank my research co-advisors Dr. Cengiz S. Ozkan and Dr. Mihrimah Ozkan for accepting and supporting me as their Ph.D student. With their encouragement and instruction over the years, I was able to learn and use various precision instruments systematically and make progress in my scientific research and studies successfully. I am grateful to Dr. Kambiz Vafai and Dr. Guanshui Xu for serving as my committee members for my final defense.

I would like to thank the past and present members of the Ozkan research group for their support and contributions to my work, including Yi Ma, Dr. Amir-Ali Sadat Akhavi, William C. Coley, Dr. Pedro Pena, Dr. Miguel Isarraraz, Dr. Taner Zerrin, Dr. Arash Mirjalili, Dr. Bo Dong, Dr. Yige Li, Dr. Daisy Patino, Dr. Jingjing Liu, Dr. Fabian Villalobos, and Dr. Rachel Ye. I am grateful to Dr. Dong Yan, Dr. Krassimir N. Bozhilov, and Matthew M. Dickson for their assistance in cleanroom training, ALD, magnetron sputtering, TEM, FIB and STEM. I would like to thank Dr. Mustafa Kurban for his contribution in DFT calculations to my work. I am grateful to my excellent undergraduates Aotian Zhang and Mei Teng Wu for their hard work.

I especially would like to thank my husband Haoping Wang for his love and support, I would not have completed my degree without him always by my side. I am grateful to my friends Yiqing Chen and Xi Ding for their accompany and encouragement, our friendship makes my life better in the US.

I would like to thank my parents, Yuqin Sun and Lianhe Wang, especially my mother, I wouldn't be who I am today without her unwavering love and support. I am

grateful to my grandparents, aunts, uncles and cousins, I wouldn't be where I am today without my family members.

The text of this dissertation, in part or in full, is a reprint of the material as it appears in the following publications:

[1] Shang, Ruoxu, Taner Zerrin, Bo Dong, Cengiz S. Ozkan, and Mihrimah Ozkan. "Sustainable and Low-Cost Lithium-Ion Batteries: Nonconventional Electrode Chemistries and State of Health Characterization." Technology & Innovation 21, no. 4 (2020): 1-23.

[2] Shang, Ruoxu, Mustafa Kurban, Ma Yi, Mihrimah Ozkan, and Cengiz S. Ozkan. "Rational design of SnO2 thin film coated cathode with function of entrapping polysulfides for performance enhanced Li–S batteries." Journal of Power Sources 597 (2024): 234144.

ABSTRACT OF THE DISSERTATION

Interfacial Design and Modification for Next-Generation Lithium-Ion Batteries

by

Ruoxu Shang

Doctor of Philosophy, Graduate Program in Materials Science and Engineering
University of California, Riverside, September 2024
Dr. Cengiz S. Ozkan, Co-Chairperson
Dr. Mihrimah Ozkan, Co-Chairperson

In recent years, the trend of replacing traditional fuel vehicles with electric vehicles has become increasingly evident worldwide, aiming to reduce automobile exhaust emissions and address the gradual depletion of petroleum resources. However, traditional lithium-ion batteries are currently facing various problems which seriously hinder their further development. For example, the energy density of traditional lithium-ion batteries has reached a limit of about 300Wh/kg, which seriously limits the mileage of electric vehicles on a single charge. For another example, battery electrolyte is an organic liquid, which is flammable and poses a safety hazard. In order to solve these issues, the development of next-generation rechargeable batteries is imminent.

In order to improve battery capacity, the development and application of high-nickel cathodes have attracted much attention. Among them, $LiNi_{0.8}Mn_{0.1}Co_{0.1}O_2$ (NMC811) gains a lot of interest, because it has a capacity of more than 200 mAh/g and a

wide chemical window. However, NMC811 has not yet been commercialized due to the following problems: (1) Irreversible phase transition under high voltage. (2) Parasitic reactions at interface. (3) Hydrofluoric acid attack during cycling. Another type of new battery is lithium-sulfur batteries, which have a theoretical capacity of up to 1675 mAh/g. However, the shuttle effect of lithium-sulfur batteries leads to a significant reduction in its capacity and short cycle life. Besides, in order to solve the safety issue, solid electrolytes and all-solid-state batteries have attracted widespread attention. However, solid-state batteries currently also have some problems: (1) Battery short circuit caused by lithium dendrite growth. (2) Serious side reactions at the electrode-electrolyte interface. (3) Low electrolyte ionic conductivity. (4) Narrow electrolyte electrochemical window. (5) Poor contact between electrolyte and active materials in the cathode. These problems of the next-generation batteries can be improved by designing and modifying the electrode interface. In this study, we used nano-deposition technologies such as atomic layer deposition and magnetron sputtering to tailor the interface of high-nickel cathode, lithium-sulfur battery and all-solid-state battery, and improved the performance significantly. This also provides ideas and inspiration for other researchers and the commercialization of next-generation batteries.

Table of Contents

1 Introduction 1

1.1 Renewable Energy Storage Solutions 1

1.1.1 Renewable Silicon Materials 4

1.1.2 Bio-derived Carbon Materials 10

1.1.3 Upcycling Waste Materials 12

1.2 Backgrounds of Traditional Lithium-ion Battery 16

1.3 Backgrounds of Ni-rich Cathode 18

1.4 Backgrounds of Li-S Battery 19

1.5 Backgrounds of Solid Electrolyte and All-solid-state Battery 23

2 Experimental Methods and Instrumentation 28

2.1 HfO_2-based Artificial Cathode Electrolyte Interphase (CEI) through Atomic Layer Deposition for High Voltage Stable NMC811 Electrode 28

2.1.1 Cathode Preparation 28

2.1.2 HfO_2 Coating via ALD 29

2.1.3 Material Characterizations 29

2.1.4 Coin Cell Assembly 30

2.1.5 Electrochemical Measurements 31

2.1.6 Post-Mortem Characterization 31

2.2 Rational Design of SnO_2 Thin Film Coated Cathode with Function of Entrapping Polysulfides for Performance Enhanced Li-S Batteries 32

2.2.1 Preparation of Sulfur/Porous Carbon Cathodes 32

2.2.2 SnO_2 Thin Film Coating 33
2.2.3 Materials Characterization 33
2.2.4 Coin Cell Assembly 35
2.2.5 Electrochemical Measurements 36
2.2.6 Computational Methods 37
2.3 Interfacial Modification of Li_6PS_5Cl-based All-solid-state Li-S Batteries by Al_2O_3 Nano-layer Deposition 38
2.3.1 Li_6PS_5Cl-based Cathode Preparation 38
2.3.2 Al_2O_3 Coating via Atomic Layer Deposition 38
2.3.3 Materials Characterization 39
2.3.4 Symmetrical Cell Assembly 39
2.3.5 Electrochemical Measurements 40
2.3.6 Post-Mortem Characterization 40
3 HfO_2-based Artificial Cathode Electrolyte Interphase (CEI) through Atomic Layer Deposition for High Voltage Stable NMC811 Electrode 41
3.1 HfO_2 ALD Deposition Analysis 41
3.2 Cycling and Rate Test Results 47
3.3 Cyclic Voltammetry and Li ion Diffusion Coefficient Results 52
3.4 Electrochemical Impedance Spectroscopy Results 59
3.5 Scanning Electron Microscopy Results 62
4 Rational Design of SnO_2 Thin Film Coated Cathode with Function of Entrapping Polysulfides for Performance Enhanced Li-S Batteries 70

4.1 SnO_2 Magnetron Sputtering Analysis 70

4.2 Cycling and Electrochemical Results 75

4.3 DFT Calculation Results 83

4.4 Electrochemical Impedance Spectroscopy and Galvanostatic Intermittent Titration Technique Results 89

4.5 Scanning Electron Microscopy and Energy Dispersive X-ray Spectroscopy Results 93

5 Interfacial Modification of Li_6PS_5Cl-based All-solid-state Li-S Batteries by Al_2O_3 Nano-layer Deposition 98

5.1 Designed All-solid-state Battery Structure and ALD Deposition 98

5.2 Ion Conductivity of Solid Electrolyte 100

5.3 Electrochemical Results of Symmetrical Cells 101

5.4 EIS and SEM results of Symmetrical Cells 102

6 Conclusions and Recommendations for Future Work 104

6.1 Advancements in Material Science 104

6.2 Scalability and Manufacturing Processes 106

6.3 Optimization of Fast Charging Capabilities 107

6.4 Enhanced In-Operando Characterization Techniques 109

6.5 Synergy with Renewable Energy Technologies 111

6.6 Development of Regulatory and Safety Protocols 111

7 Bibliography 112

List of Figures

Figure 1.1 (a) Cost breakdown of a graphite-based LIB. Among the different components contributing to the overall cost, cathode (28%) and anode (24%) materials account for the highest proportions[4]. (b) LIB pack annual price drop with cost predictions until 2030. Prices are given in $/kWh[5]. 2

Figure 1.2 (a) Coin cell assembled using beach sand as the silicon precursor, which saves around 30% of the overall cost of anode materials[24]. (b) Utilizing mushroom, a type of biomass, as an alternative to graphite to assemble binder-free anodes of lithium-ion c coin cells results in around 6% weight saving and 15% cost saving for the anode[27]. (c) Coin cells and pouch cells assembled by waste glass bottles as silicon precursor saves around 30% of the total cost of anode material[28]. (d) Supercapacitors assembled by porous carbon materials derived from waste plastic bottles. Around 24% of the overall material cost of LIB is attributed to the anode. The sustainable and renewable materials demonstrated here could reduce the cost of LIB anodes[4]. 8

Figure 1.3 Representative schematic of the first LIB, consisting of a $LiCoO_2$ cathode, a graphite anode, and the electrolyte. During charge, lithium ions are forced to release the layered $LiCoO_2$ structure, and they move to the graphite anode. During discharge, lithium ions move back across the electrolyte to the cathode while producing a current on the outer circuit. In both charging and discharging processes, the liquid electrolyte enables the conduction of the ionic component of the chemical reactions between the two electrodes and forces the electrons to move through the outer circuit. The crystal structure images of $LiCoO_2$ and graphite are generated by using VESTA[46]. 17

Figure 1.4 Total number of (a) publications and (b) patents related to Li-S batteries after 2010. In the last ten years, the total number of publications has increased by a factor of 20, whereas the total number of issued patents has increased by a factor of four. The numbers listed here are obtained from Web of Science for the publications and Google Scholar for the issued patents. 22

Figure 1.5 Modifications in material and battery design across material, cell, and system tiers offer fresh avenues for enhancing safety strategies in SSBs[96]. 25

Figure 3.1 Schematic depiction of HfO_2 thin film coating procedure on NMC811 cathode by ALD. 43

Figure 3.2 (a) SEM image; (b-g) corresponding elemental mapping of Ni, Co, Mn, C, Hf and O; (h) EDS spectra and (i) Raman spectra for HfO_2 coated NMC811 cathode before cycling. 44

Figure 3.3 (a) SEM image; (b) EDS spectra; (c) elemental mapping and (d-h) corresponding elements of Ni, Co, Mn, C and O for uncoated NMC811 cathode before cycling. 45

Figure 3.4 Elemental concentration in weight percent and statistical error of C, Ni, O, F, Co, Mn, Hf, Pd for HfO_2 coated NMC811 cathode before cycling. 46

Figure 3.5 Elemental concentration in weight percent and statistical error of C, Ni, O, Co, F, Mn, Pd for uncoated NMC811 cathode before cycling. 47

Figure 3.6 (a) Cycling performance of HfO_2 coated and uncoated NMC811 cells at 0.5C over 200 cycles; Charge-discharge profiles for (b) HfO_2 coated and (c) uncoated NMC811 cells after 1st, 100th and 200th cycles at 0.5C; (d) Rate performance of HfO_2 coated and uncoated NMC811 cells from 0.1 to 5C; (e) Cycling performance of uncoated and HfO_2 coated NMC811 cells at 1C over 200 cycles. 49

Figure 3.7 CV curves of (a) uncoated and (b) HfO_2 coated NMC811 cells after 100th and 200th cycles at 1C; CV curves with increased scan rates from 0.1 mV/s to 1.0 mV/s for (c) uncoated and (d) HfO_2 coated NMC811 cells; Line plots of oxidation and reduction peak current obtained from (c) and (d) as a function of the square root of scan rate for (e) uncoated and (f) HfO_2 coated NMC811 cells. 52

Figure 3.8 (a) Estimated Li ion Diffusion Coefficient (D_{Li^+}) of uncoated and HfO_2 coated NMC811 cells; (b) The relative electrochemical reversibility of uncoated and HfO_2 coated NMC811 cells, which is calculated by the absolute value of the ratio of oxidation and reduction peak area minus one as the function of the scan rate. 56

Figure 3.9 Equivalent circuit fitting model for NMC811 batteries. R_E represents the electrolyte resistance, R_{CEI} represents the cathode/electrolyte interphase resistance and R_{CT} represents the charge transfer resistance at the interface between electrode and electrolyte. CPE_1 and CPE_2 are the constant phase related to the double layer capacitance. W_1 is Warburg resistance associated with diffusion of Li^{+}[130-133]. 59

Figure 3.10 EIS plots of uncoated and HfO_2 coated NMC811 cells (a) after condition cycles, (b) after 100 cycles, and (c) after 200 cycles at 0.5C from 2.5V to 4.6V; (d) Fitting results of impedance spectra for R_{CEI} and R_{CT}. 61

Figure 3.11 Scheme of the degradation mechanisms of (a) uncoated and (b) HfO_2 coated NMC811 electrodes; Surface morphologies of (c) uncoated and (d) HfO_2 coated NMC811 electrodes after 200 cycles at 0.5C; Cross sections of (e) uncoated and (f) HfO_2 coated NMC811 electrodes after 200 cycles at 0.5C; Surface morphologies of lithium anodes of (g) uncoated and (h) HfO_2 coated NMC811 electrodes after 200 cycles at 0.5C. 64

Figure 3.12 Elemental mapping and corresponding elements of Ni, Co, Mn, O, C and F for HfO_2 coated NMC811 cathode after 200 cycles at 0.5C..... 65

Figure 3.13 EDS spectra for HfO_2 coated NMC811 cathode after 200 cycles at 0.5C. .. 65

Figure 3.14 Elemental mapping and corresponding elements of Ni, Co, Mn, O, C and F for uncoated NMC811 cathode after 200 cycles at 0.5C. 66

Figure 3.15 EDS spectra for uncoated NMC811 cathode after 200 cycles at 0.5C. 67

Figure 3.16 EDS spectra for lithium anode of HfO_2 coated NMC811 cathode after 200 cycles at 0.5C. 68

Figure 3.17 EDS spectra for lithium anode of uncoated NMC811 cathode after 200 cycles at 0.5C. 69

Figure 4.1 Synthesis process of Sulfur/Porous carbon cathodes and SnO_2 thin film coating by magnetron sputtering. 72

Figure 4.2 (a) Surface morphology of 5 nm SnO_2 coated Sulfur/Porous carbon cathode; (b, c, d, e) Elemental mapping of S, C, Sn and O; (f) Raman spectrum of 5 nm SnO_2 coated Sulfur/Porous carbon cathode; (g) TGA curve of Sulfur and Porous carbon composites..... 73

Figure 4.3 Elemental concentration in weight percent and statistical error of C, S, O and Sn. 74

Figure 4.4 (a) High-angle annular dark field (HAADF) and (b) bright field STEM images of SnO_2 coated cathode in low magnification; (c) Elemental mapping of C, S, Sn for (d) HAADF image of SnO_2 coated cathode in high magnification; (e, f, g) Elemental mapping of O, Sn and C for (d) respectively. 75

Figure 4.5 (a) Cycle performance of uncoated, 2 nm, 5 nm and 10 nm SnO_2 coated Li-S cells at 0.1C over 100 cycles; (b) Cycle performance of uncoated and 5 nm SnO_2 coated Li-S cells at 0.5C over 100 cycles; (c) Rate performance of uncoated and 5 nm SnO_2 coated Li-S cells; (d) CV curves of uncoated and 5 nm SnO_2 coated Li-S cells after condition cycles; (e) CV curves of 5 nm SnO_2 coated Li-S cells after 1^{st}, 5^{th} and 15^{th} cycles at 0.5C; (f) Voltage profiles of uncoated and 5 nm SnO_2 coated Li-S cells after 1^{st}, 50^{th} and 100^{th} cycles at 0.1C; Tafel plots derived from the (g) anodic scan and (h) cathodic scan of CV curves; (i) digital photos of 2 mM Li_2S_6 solution and SnO_2 added 2 mM Li_2S_6 solution after 7 h of static adsorption..... 78

Figure 4.6 Optimized structures for (a) Li_2S, (b) Li_2S_2, (c) Li_2S_4, (d) Li_2S_6, (e) Li_2S_8, and (f) S_8 on the SnO_2 surface. Yellow, green, red, and blue colors indicate S, Li, O and Sn

atoms, respectively; (g) Binding energies of the LiPs, Li, S, and S_8 on the SnO_2 surface; Schematic diagram of polysulfides migration in (h) uncoated Li-S cell and (i) SnO_2 coated Li-S cell. 83

Figure 4.7 The optimized structures of (a) Li and (b) S atoms on the SnO_2 surface. 84

Figure 4.8 EIS plots of uncoated and 5 nm SnO_2 coated Li-S cells (a) before condition cycles, (b) after condition cycles, (c) after 100 cycles at 0.1C, and (d) after 100 cycles at 0.5C; GITT measurements of uncoated and 5 nm SnO_2 coated Li-S cells (e) during charging and (f) discharging. 89

Figure 4.9 Equivalent circuit fitting model for Li-S batteries (a) before cycles and (b) after cycles. R_e is the electrolyte resistance, R_{ct} is the charge-transfer resistance, and R_{int} is interface contact resistance. Q1 and Q2 are the constant phase related to the capacitance. W is Warburg resistance associated with diffusion of Li^{+158}. 92

Figure 4.10 (a) Surface morphology, cross sections (b) before condition cycles and (c) after 100 cycles at 0.1C of uncoated cathode; (d) Surface morphology, cross section (e) before condition cycles and (f) after 100 cycles at 0.1C of 5 nm SnO_2 coated cathode; Surface morphologies and elemental mapping of lithium anodes of (g) uncoated Li-S cell and (h) 5 nm SnO_2 coated Li-S cell; (i) Sulfur concentration on lithium anodes. 93

Figure 4.11 EDS mapping of (a) S, (b) O, (c) F and (d) C elements for the lithium anode paired with uncoated cathode. 95

Figure 4.12 EDS spectrum for the lithium anode paired with uncoated cathode. Elemental concentration in weight percent and statistical error of O, S, C and F. 96

Figure 4.13 EDS mapping of (a) S, (b) O, (c) F and (d) C elements for the lithium anode paired with 5 nm SnO_2 coated cathode. 96

Figure 4.14 EDS spectrum for the lithium anode paired with 5 nm SnO_2 coated cathode. Elemental concentration in weight percent and statistical error of O, S, C and F. 97

Figure 5.1 Designed Li_6PS_5Cl-based all-solid-state Li-S batteries (a) without or (b) with Al_2O_3 nano-layer deposition. 98

Figure 5.2 (a) SEM result and (b) EDS mapping for Al_2O_3 coated Indium foil with elemental analysis of (c) Al, (d) O and (e) In; (f) EDS spectra and (g) element weight percentage of Al_2O_3 coated Indium foil. 99

Figure 5.3 (a) EIS result and (b) the structure of designed symmetrical cell to calculate Li ion conductivity. 100

Figure 5.4 (a) Structure of Al_2O_3 coated symmetrical cell; (b) Cycling data of coated and uncoated symmetrical cells; Cycling data after (c) 15h, (d) 150h and (e) 328h of coated and uncoated symmetrical cells. 101

Figure 5.5 EIS results of (a) uncoated and (b) coated symmetrical cell after 150 cycles. 102

Figure 5.6 SEM results for electrodes of (a) uncoated and (b) coated symmetrical cells after cycling. 103

List of Tables

Table 3.1 Slope obtained from Figure 3.7e and f for uncoated and HfO_2 coated NMC811 cells and calculated Li ion Diffusion Coefficient D_{Li^+} (cm^2/s). 56

Table 3.2 Area of oxidation and reduction peaks obtained from Figure 3.7c and 3.7d for uncoated and HfO_2 coated NMC811 cells. 58

Table 3.3 EIS fitting results for uncoated and HfO_2 coated NMC811 batteries after conditions, after 100 cycles and after 200 cycles at 0.5C. 61

Table 3.4 Elemental concentration in weight percent and statistical error of C, O, Ni, F, Co, Mn, Hf for HfO_2 coated NMC811 cathode after 200 cycles at 0.5C. 66

Table 3.5 Elemental concentration in weight percent and statistical error of C, O, Ni, F, Co, Mn for uncoated NMC811 cathode after 200 cycles at 0.5C. 67

Table 3.6 Elemental concentration in weight percent and statistical error of O, C, F for lithium anode of HfO_2 coated NMC811 cathode after 200 cycles at 0.5C. 68

Table 3.7 Elemental concentration in weight percent and statistical error of O, C, F for lithium anode of uncoated NMC811 cathode after 200 cycles at 0.5C. 69

Table 4.1 Capacity contributions from different electrochemical reaction steps for uncoated and 5 nm SnO_2 coated Li-S batteries. 82

Table 4.2 The binding energies (in eV) of SnO_2 and polysulfides interactions and comparison with the previous reports. 86

Table 4.3 EIS fitting results for uncoated and 5 nm coated Li-S batteries before/after condition cycles, after 100th cycle at 0.1C and after 100th cycle at 0.5C[66]. 92

Chapter 1

1 Introduction

1.1 Renewable Energy Storage Solutions

Electrical energy storage systems play a key role in modern society by supplying continuous power and decreasing the consumption of fossil fuels[1]. Among all the electrical energy storage systems, batteries and supercapacitors attract the most attention due to their high energy density and high power density, respectively. Especially, lithium-ion batteries (LIBs) are widely used in electric vehicles (EVs) and smart buildings due to their relatively high energy densities[2]. According to the "Electric Vehicle Outlook 2019" by Bloomberg New Energy Finance, 57% of new car sales and 30% of the global car fleet will be electric by 2040[3]. However, the high cost of raw materials restricts the utilization of LIBs in larger-scale applications. As shown in Figure 1a, around 65% of total battery cost is dominated by the source materials, in which cathode and anode materials are the most expensive components, accounting for 28% and 24% of the total cost, respectively[4].

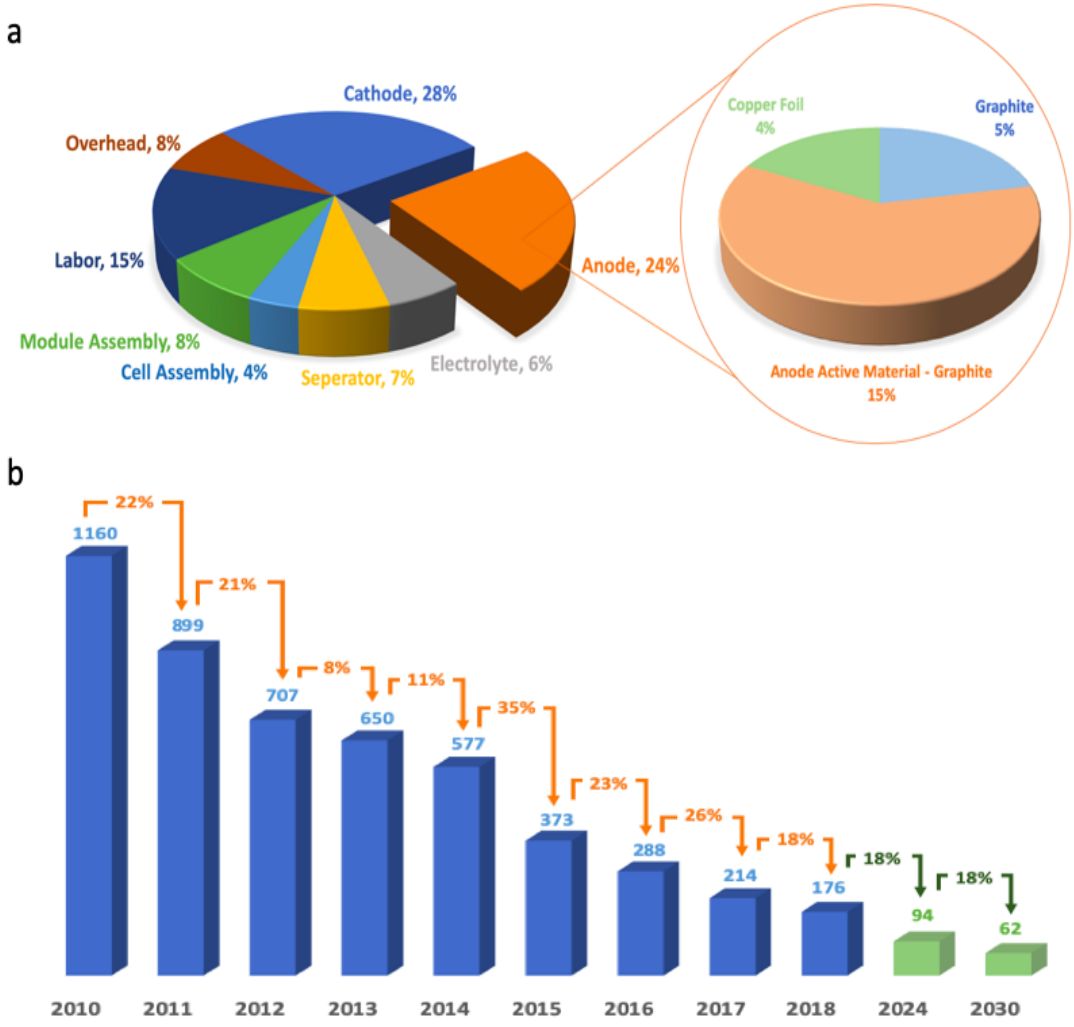


Figure 1.1 (a) Cost breakdown of a graphite-based LIB. Among the different components contributing to the overall cost, cathode (28%) and anode (24%) materials account for the highest proportions[4]. (b) LIB pack annual price drop with cost predictions until 2030. Prices are given in $/kWh[5].

Nowadays, most of the LIBs utilized in EVs use lithium nickel manganese cobalt oxide (NMC) or lithium nickel cobalt aluminum oxide (NCA) cathodes containing high proportions of the cobalt element, which is environmentally hazardous and expensive. $LiFePO_4$ (LFP) cells are good candidates for cobalt-free batteries because they have long cycle lives and good thermal stabilities. However, they are not comparable with cobalt-

based batteries in terms of other important performance parameters. Firstly, the capacity of LFP is lower than those including cobalt element. Also, their lower nominal voltage reduces the specific energy below that of cobalt-based cathodes. Another disadvantage of LFP cells is their higher self-discharge rate compared to other LIBs. The adoption rate of LFP batteries in EV applications is decreasing, whereas the adoption rate of cobalt-based NMC and NCA batteries is increasing. This is mainly because of the higher power rating and energy density of the cobalt-based cathodes compared to LFP. This difference originates from the lower lithium ion diffusion rate and electron mobility of LFP. Lithium ions in LFP can only move in one direction, whereas, for example, in NMC, they can move in two different directions. Because of this, lithium ion diffusion can be 10,000 times higher in NMC compared to LFP; similarly, electron mobility in NMC can be 1,000 times faster compared to LFP[6]. It is estimated by the U.S. International Trade Commission that the cobalt fraction in the positive electrodes used in EVs in 2017 was about 30%. In addition, the lithium cobalt oxide (LCO) cathode, which is widely used in cell phones, tablets, laptops, and cameras, contains a cobalt fraction as high as 60%, occupying 50% of the total weight of cathodes[7,8]. With such high amounts of cobalt fractions in LIBs, the price of battery-grade cobalt metal (at least 99.8%) is $17.675 per pound, which is more than three times the price of nickel and around 23 times the price of aluminum[7]. In addition, around 54,354 metric tons of cobalt entered the LIB industry in 2017, and this number is forecasted to reach 276,401 metric tons by 2028 due to the rapid growth of demand for cobalt[9]. According to the report given by the U.S. Geological Survey, approximately 140,000 metric tons of cobalt were mined globally in 2018. Even

with the contribution from recycled cobalt, the current mine output is still much lower than the cobalt amount required by the industry[9]. With the trend of EVs replacing traditional internal combustion engine vehicles, the demand for cobalt from the market will continue to rise; however, the cobalt resources on earth are limited, which may inevitably lead to a dramatic increase in the price of the cobalt metal. Although the LIB pack prices are predicted to drop in the short term, as shown in **Figure 1.1b**, the manufacturers may be obliged to use alternative cathode materials to cobalt due to a possible much higher demand for LIBs expected in the EV market in the long term.

In addition to the cost of the cathode materials, anode materials also account for a considerable proportion of the overall material cost of LIBs. As shown in **Figure 1.1a**, the graphite anode comprises 24% of the total battery cost[4]. Moreover, the manufacturing process of anode-grade graphite consumes a majority of fossil fuels and does not satisfy the requirement of developing an eco-friendly society. Therefore, in order to lower the cost of electrical energy storage systems and protect the ecosystem, it is vital to explore renewable and sustainable materials for the next generation of electrical energy storage systems.

1.1.1 Renewable Silicon Materials

EVs are expected to replace traditional vehicles to a great extent in the future due to their potential advantages, such as fewer greenhouse gas emissions and lower energy costs[10]. However, graphite-based anodes used in conventional LIBs have a limited theoretical capacity of 372 mAh/g, which greatly restricts the performance of the

batteries for high energy density applications[11]. Silicon is considered one of the most promising candidates for anode materials of next generation LIBs due to its low discharge potential (~0.1 V vs. Li/Li^+) and high theoretical capacity of 3572 mAh/g, owing to the formation of $Li_{15}Si_4$ phase at ambient temperature[12]. However, silicon suffers from severe problems as follows: (1) Drastic volume expansion up to 300% and huge stress generation are accompanied by the lithiation/delithiation process of silicon[13]; (2) the pulverization of active materials and deterioration of the conductive network are caused by the mechanical stresses during cycling[12,14,15]; and (3) the repeated expansion and shrinkage processes result in an unstable solid-electrolyte interphase (SEI) formation, which is considered a critical factor that influences battery performance[16].

In order to solve the aforementioned problems, tremendous efforts have been made on alleviating the volume change and improving the stability of the anode structure. The strategies that have been adopted include downscaling the dimensions of silicon particles, designing special structure of anode particles, compositing with stress relief buffer materials, and so on[12,14,17]. Despite the advantages of excellent electrochemical performance of the silicon anode, many of the methods used to synthesize them lack the ability of large-scale production owing to the high cost of precursors, expensive equipment construction, and highly toxic chemicals used during synthesis. For the realization of large-scale industrial manufacturing, magnesiothermic reduction process attracts a lot of attention and is considered an efficient method to reduce silicon dioxide (SiO_2) into nanostructured silicon[18]. Compared to the traditional carbothermal reduction method, which ruins the original morphology of SiO_2 at high temperatures, this process

uses much lower working temperatures, which saves a great amount of energy[19]. However, the precursors commonly used to obtain nano-silicon are silane, halo-silane, polysilane, and silicon wafers, which are highly toxic and relatively expensive[20-23]. Therefore, it is a viable option to acquire nano-silicon from highly abundant natural sources in order to make the process environmentally benign and cost-effective. Herein, our group demonstrated two scalable synthesis methods of nano-silicon to be used as the anode material of LIBs by using magnesiothermic reduction from natural sources such as beach sand and diatomite deposits[24,25].

Deriving nano-silicon from beach sand to make batteries can be an effective strategy for mass manufacturing, as sand is a highly abundant, non-toxic, and a low-cost silicon source whose main component is quartz (SiO_2), as shown in **Figure 1.2a**. According to our calculations, sand-based anode can save around 30% of the overall cost of anode materials compared to the graphite-based anode. To obtain pure porous nano-silicon, which can serve as the anode of the battery, we used thermal scavenger-assisted magnesiothermic reduction process. Details about the process can be found in our paper[24]. Crystalline silicon nanoparticles (SiNPs) retain the highly porous 3D network structure of SiO_2 due to the etching process after reduction. After carbon coating of SiNPs, half-cells prepared with the nano-silicon/carbon (nano-Si@C) anode and lithium metal counter-electrode are characterized by cyclic voltammetry (CV), electrochemical impedance spectroscopy (EIS), etc. The results of electrochemical characterizations show that the kinetic processes in the cells improved dramatically during the first few cycles under a low current density. Then the cell was cycled at a higher rate of C/2 and achieved

an excellent capacity of 1024 mAh/g and a Coulombic efficiency of 99.1% after 1,000 cycles. The nano-Si@ C electrode clearly demonstrates a remarkable performance and opens up new avenues for the fabrication of anode materials to achieve low cost and high-performance LIBs. It was reported that sand is being extracted faster than it can be replaced although it is abundant[26]. Extraction of sand from active sources can cause great environmental, social, and economic harm; therefore, reasonable monitoring and management should be considered for the sustainable commercialization of silicon electrodes through converting sand into battery grade silicon.

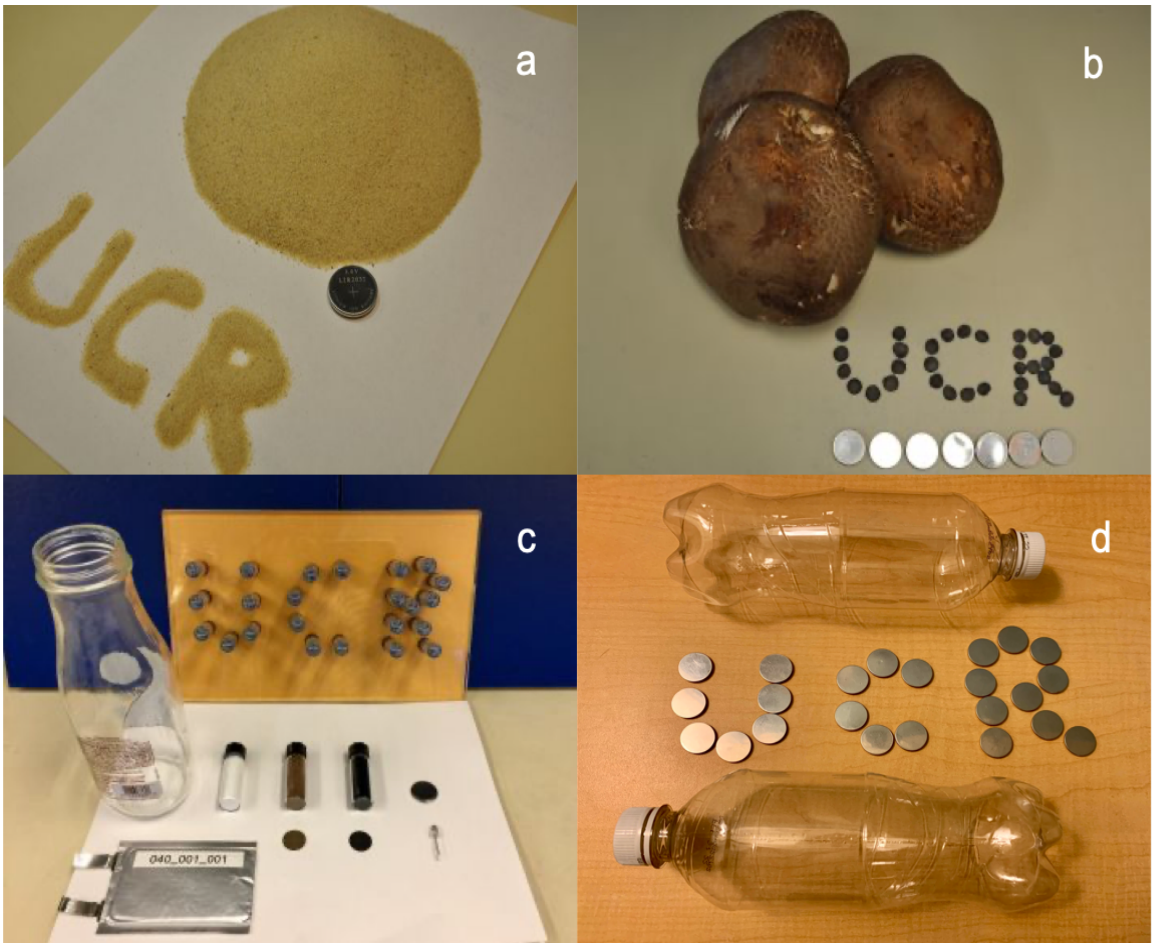


Figure 1.2 (a) Coin cell assembled using beach sand as the silicon precursor, which saves around 30% of the overall cost of anode materials[24]. (b) Utilizing mushroom, a type of biomass, as an alternative to graphite to assemble binder-free anodes of lithium-ion c coin cells results in around 6% weight saving and 15% cost saving for the anode[27]. (c) Coin cells and pouch cells assembled by waste glass bottles as silicon precursor saves around 30% of the total cost of anode material[28]. (d) Supercapacitors assembled by porous carbon materials derived from waste plastic bottles. Around 24% of the overall material cost of LIB is attributed to the anode. The sustainable and renewable materials demonstrated here could reduce the cost of LIB anodes[4].

Another precursor that we choose from natural sources to synthesize nano-silicon particles are diatomite deposits. Diatomaceous earth, also known as diatomite or DE, is a

sedimentary rock that is widespread in nature[29]. It mainly consists of fossilized frustules of algae called diatoms whose shells are mostly biomineralized as silica with small amounts of other impurities[30]. In 2019, total production of diatomite in the world was approximately 2,900 thousand metric tons, and the United States was the leading producer, accounting for ca. 980 thousand metric tons[31]. Therefore, diatomite can be considered a silicon source for the anode materials of LIBs, which has potential to be used in the manufacturing processes at the industry level.

Diatomite particles consist of a series of diatom shells with various microstructures, such as hexagonal honeycomb morphology and elongated fence-like morphology. The morphologies of diatoms frustules were conserved after being converted into elemental silicon, resulting in nano-silicon particle-composed diatom frustule structures. All of these special morphologies have macroporous architectures, which can enable the electrolyte to have easy access to the anode and provide extra room for volumetric expansion of silicon. Thus, half-cells demonstrated by the aforementioned magnesiothermic reduction process with diatomite-based anodes are even capable of handling very high current density rates, such as 4C (14.3 A/g_{si}). A specific capacity of 654.3 mAh/g can still be well maintained for diatomite-based anodes.

In summary, we demonstrated two renewable and scalable nano-silicon materials derived from natural sources via a magnesiothermic reduction process. The LIBs assembled using the nano-silicon anodes not only achieve higher specific capacities and longer cycle lives but also have significantly reduced costs compared to the graphite-based LIBs. As silicon has already been widely considered one of the most important

anode materials because of its high specific capacity, our strategy provides a promising method to develop low-cost, high performance, and environmentally benign silicon-based anode materials for LIBs.

1.1.2 Bio-derived Carbon Materials

Carbon materials are widely used in electrical energy storage systems as conductive additives, electrode materials, buffer materials, etc. The most important carbon material of LIBs is graphite, which is the traditional host material of the anode due to its layered structure, which enables the intercalation and deintercalation of lithium ions[11]. However, the industrial manufacturing process of graphite wastes a large amount of energy by heating raw materials to around 3000 °C or even higher[32]. In addition, graphite has a low theoretical specific capacity of 372 mAh/g due to its limited lithium ion storage capacity[11]. Therefore, researchers are committed to exploring new carbon materials as alternatives to graphite.

Hard carbon is considered a good candidate for the anode host material of LIBs because of its high capacity and natural abundance[33]. Buiel and Dahn reported that the hard carbon-based anode had higher specific capacity (over 500 mAh/g) than graphite[34]. However, the irreversible capacity tends to increase during cycling due to the reactions between hard carbon and electrolyte[34,35]. Another alternative to graphite is activated carbon; highly porous activated carbon with high specific surface area can be achieved by the potassium hydroxide (KOH) activation process of various precursors, such as petroleum coke, nutshell, and wood[36]. The KOH activation process mainly consists of

two mechanisms: The first one is catalyzation by potassium to create CO and CO_2 by consuming carbon and oxygen; the second one is the expansion of the carbon lattice by reduced potassium intercalation[36,37]. However, KOH is a strong base, which is a very strong and toxic etchant; therefore, it is necessary to explore stable, high capacity, and nontoxic carbon materials as a host material in the anode.

Next, we discuss the use of sustainable carbon materials derived from the cap skin tissue (CST) of the mature fruiting body of the fungus *A. bisporus*, also named as the portobello mushroom (PM), shown in **Figure 1.2b**[27]. Based on the calculations, a PM CSTs-based anode leads to about 6% weight savings and 15% cost savings compared to conventional graphite. The porous carbon materials are obtained by a pyrolysis procedure, details of which can be found in our paper on bio-derived, binderless, hierarchically porous carbon anodes for LIBs[27]. Original PM CSTs have ribbon-like microstructures, and carbon nanoribbons are obtained after dehydrating and stabilizing until the temperature reaches 500 °C. At the temperature of 1100 °C, PM CSTs are fully pyrolyzed, and hierarchically porous carbon nanoribbons are acquired. Based on scanning electron microscope images, PM CSTs display hierarchical porous structures consisting of macro-, meso-, and micro-pores when the temperature is higher than 900 °C. The large number of voids are able to offer numerous positions for the intercalation of lithium ions, which increases the capacity of PM CSTs-based battery cells dramatically. The high porosity is mainly caused by the reaction between oxygen and high concentrations of potassium chloride that are naturally present in PM CSTs, which is similar to the KOH activation process. The carbon materials derived from PM CSTs have been used as

freestanding anodes for binder-free and current collector free half-cells. Electrochemical performance results showed that PM CSTs-based anodes demonstrated excellent cycling performance, and the specific capacity of the electrode was 410 mAh/g at C/5 after 1,700 cycles. Even without the use of any polymer binders or conductive additives, the performance of PM CSTs-based anodes is comparable to that of conventional graphite-based anodes. Therefore, PM CSTs-based anodes could be a very good alternative to graphite since it performs similarly with the advantages of reduced overall cost and weight.

To sum up, a hierarchically porous carbon material derived from mushrooms is shown as an alternative to graphite to be used in LIBs. The coin cells assembled by mushroom-based anodes achieved around 6% weight savings and 15% cost savings compared to the traditional graphite-based anodes. Plenty of biomass materials, including coconut shells, have been successfully converted into carbon as electrode materials in the industry due to their low cost and abundance[38]. This work provides another promising approach to convert biomass into carbon electrode materials at the manufacturing level. The results obtained in our work on mushroom-based carbon materials may lead to further development in the research of low-cost and environmentally friendly anode materials.

1.1.3 Upcycling Waste Materials

In addition to the diatomite and sand precursors mentioned in the previous sections, there are other natural sources of electrode materials, such as rice husks, reed

leaves, and bamboo leaves, that can serve as silicon precursors[39-41]. However, strong acids and bases, such as hydrogen chloride, hydrogen fluoride, and sodium hydroxide, are still required to remove the impurities in the natural precursors during the etching processes, which results in the production of large amounts of toxic waste. In addition, since the silicon content of natural precursors varies in different regions, the silicon yield of natural precursors depends heavily on the geographic location of the samples, which may lead to low silicon yields for specific regions. To remedy these problems, our group proposed a non-etching, easy to collect, abundant, and high yield silicon precursor: upcycled waste glass bottles (**Figure 1.2c**)[28].

Millions of tons of waste glass are generated each year in the United States, more than 70% of which are disposed of in landfills[42]. However, as glass cannot decompose itself, it occupies thousands of square acres of landfills, and this costs a large amount of money and human resources. Therefore, recycling glass waste is of great significance for saving land sources and creating a greener environment. One alternative strategy of recycling glass bottles is to use them as a silicon precursor for anode materials of LIBs since they are easier to collect and the main content of glass bottles is SiO_2. Therefore, compared to natural silicon sources, higher yield of silicon and less toxic waste can be achieved by using waste glass bottles as the silicon precursor. Our research shows that the carbon-coated glass derived-silicon (gSi@C) electrode achieves around 30% cost savings compared to the conventional graphite-based anode, which reduces the overall cost of materials of LIBs remarkably. Furthermore, gSi@C-based anode demonstrates an outstanding electrochemical performance with an initial specific capacity of 1800 mAh/g

and a reversible capacity of 1420 mAh/g at C/2 after 400 cycles, which may be due to the highly interconnected silicon structure. In addition, excellent initial cycling stability has been demonstrated by full battery cells consisting of gSi@C anodes and $LiCoO_2$ cathodes with high energy densities. Because the full cells were tested in the lab scale, more tests and validations may be needed for commercialization. Nevertheless, these results demonstrate that there is potential in upcycling waste glass into electrode materials for large-scale applications.

Apart from glass waste, the amount of plastic waste generated yearly also has increased at a shocking rate with the dramatic development of economics and rapid progress of the industry[43]. It has been estimated that about 300 million tons of plastics are produced every year, and only around 9% of the discarded plastic is recycled[43,44]. Apart from recycled and incinerated plastic waste, about 79% of remaining plastic waste ends up in landfills[44]. However, it is commonly known that plastic is difficult to decompose in the natural environment for tens to hundreds of years due to its high molecular weight and stable physical and chemical structure. The decomposed plastic debris in nature results in lots of severe hazards, including, but not limited to, the waste of land sources and destruction of the ecological environment, which becomes harmful for animal and human health[45]. Therefore, it is urgent to develop meaningful management and recycling strategies for plastic waste. Among the various types of plastic waste, polyethylene terephthalate (PET) occupies a large proportion, as it has been widely utilized in different applications, such as automotive, textile, and packaging industries. Herein, our group presents a successful way to transfer PET waste bottles into active carbon materials,

which can be used in manufacturing double-layered supercapacitors, as shown in **Figure 1.2d**.

The active carbon materials obtained from plastic waste bottles after ball milling possess an interconnected network mainly dominated by amorphous carbon with randomly distributed, highly ordered reduced graphene oxide (rGO). Electric double-layer capacitors (EDLCs), also called supercapacitors, are assembled with active carbon powders with high surface areas as electrodes and separators. EDLCs have been tested by EIS, galvanostatic cycling with potential limitation (GCPL), and CV, and the results reveal that the EDLCs are very stable and have long life. The material was also tested in an LIB as the anode; however, the performance was not good enough compared to the commercial anode materials. Therefore, further research needs to be developed. Nevertheless, it was shown that carbon obtained from waste bottles could be used in supercapacitors, and it may have a vast potential in the future designs of other electrical energy storage systems that could satisfy the requirements for renewability and sustainability.

In summary, we demonstrated two simple and scalable methods for converting waste into electrochemical energy storage materials. Through the described processes, thousands of discarded glass and plastic bottles can be recycled and transferred into useful materials, which not only protects the natural environment and resources but also provides a new way to reduce the cost of electrochemical energy storage materials.

1.2 Backgrounds of Traditional Lithium-ion Battery

State-of-the-art technology of LIBs still depends on the same chemistry that enabled the commercialization of LIBs for the first time in the 90s. This chemistry, which uses conventional intercalation electrode materials, enables batteries to have a low self-discharge rate and a relatively higher energy density compared to the older technologies. As shown in **Figure 1.3**, the cathode (positive electrode) is a type of lithium metal oxide ($LiCoO_2$), and the anode (negative electrode) is carbon, usually graphite. The space between the two electrodes is filled with electrolyte, which provides a conducting medium for lithium ions to transfer. During charging, lithium ions leave the layered metal oxide structure of the cathode and flow into the anode. The opposite reaction happens during discharge: Lithium ions leave the anode and turn back to the empty sites in the layered metal oxide structure of the cathode. The related redox reactions for the anode and the cathode are given in **Equations 1.1** and **1.2**, respectively.

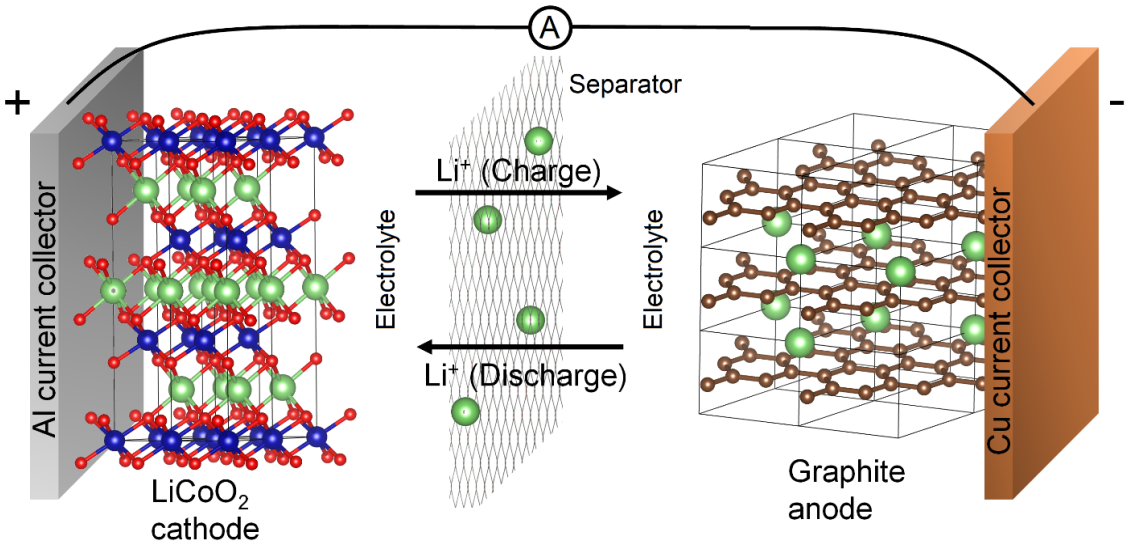


Figure 1.3 Representative schematic of the first LIB, consisting of a $LiCoO_2$ cathode, a graphite anode, and the electrolyte. During charge, lithium ions are forced to release the layered $LiCoO_2$ structure, and they move to the graphite anode. During discharge, lithium ions move back across the electrolyte to the cathode while producing a current on the outer circuit. In both charging and discharging processes, the liquid electrolyte enables the conduction of the ionic component of the chemical reactions between the two electrodes and forces the electrons to move through the outer circuit. The crystal structure images of $LiCoO_2$ and graphite are generated by using VESTA[46].

Equation 1.1

$$C + xe^- + xLi^+ = Li_xC\ (anode)$$

Equation 1.2

$$LiCoO_2 - xe - xLi^+ = Li_{1-x}CoO_2\ (cathode)$$

Although the electrodes with traditional lithium-ion chemistries can provide stable and highly efficient batteries, their specific capacities have reached a limit. The cathode materials of conventional LIBs commonly include cobalt, and they have specific capacities around 100 to 200 mAh/g and energy densities of 150 to 250 Wh/kg, which are

not sufficient to meet the growing demand in applications that require materials with high energy storage capacities, e.g., electric/hybrid vehicles and remote control aerial devices[47]. In addition, cobalt-based cathodes tend to be more expensive because of the relatively high prices of cobalt ($17.675 per pound)[7]. Although manufacturers are trying to decrease the cobalt content in commercial batteries used in electric vehicles, the cobalt loading per vehicle increased 45% in the first half (H1) of 2019 compared to the levels of 2018 H1. Similarly, in the first half of 2019, a total of 7,200 tons of battery-grade cobalt metal were used in electric vehicle batteries globally, which is 81% greater than the levels in 2018[48]. Furthermore, cobalt reserves on earth are very restricted, and more than half of the total cobalt supply needed for the batteries is being provided from only one country, which causes political instabilities and difficult mining practices in the area. Since cobalt is a toxic metal, the mining practices are dangerous for both the workers and the environment. Because of all these issues, researchers have been devoted to exploring new chemistries that could utilize abundant and environmentally benign materials and could lead to improvements in the specific capacities and energy densities of the batteries at the same time.

1.3 Backgrounds of Ni-rich Cathode

Due to the promotion of electric vehicles, research on lithium-ion battery materials is imminent. However, the current commercial NMC cathodes, $LiNi_xMn_yCo_{(1-x-y)}O_2$, such as NMC111 and NMC532, limit the driving distance of electric vehicles per unit charging time, so the development and application of high-nickel cathodes have

attracted much attention[49]. High-nickel cathodes usually refer to NMC materials with x equal to or higher than 0.6[50]. The Ni element can provide capacity through $Ni^{2+}/Ni^{3+}/Ni^{4+}$ redox species in redox reactions[51]. Higher Ni content will bring higher energy density and theoretical capacity. Among high-nickel cathodes, $LiNi_{0.8}Mn_{0.1}Co_{0.1}O_2$ (NMC811) gains a lot of interests, because it has a capacity of more than 200 mAh/g and a wide chemical window. However, NMC811 has not yet been commercialized due to the following problems: (1) When the voltage exceeds 4.2V, the delithiated NMC811 electrode undergoes an irreversible phase transition from a layered phase to a NiO-like phase, which causes capacity loss and reduced reversibility of the electrochemical reaction[52]. (2) Lithium compounds from the preparation process remain on the surface of NMC811 particles. These compounds undergo parasitic reactions under high pressure, produce reactive oxygen and carbon dioxide, and consume electrolytes, leading to increased resistance and electrode cracks[53]. (3) During the battery cycle, the electrolyte reacts with residual water to produce hydrofluoric acid (HF), which attacks the electrolyte/positive electrode interface, aggravating the parasitic reaction, reducing ion transfer efficiency and further causing electrode cracking[54]. These problems result in a short cycle life, low rate performance, and poor capacity retention of the NMC811 positive electrode, hindering its large-scale commercialization.

1.4 Backgrounds of Li-S Battery

In recent years, the trend of replacing traditional fuel vehicles with electric vehicles (EVs) has become increasingly evident worldwide, aiming to reduce automobile

exhaust emissions and address the gradual depletion of petroleum resources[55]. However, current conventional lithium-ion batteries have reached a limit of about 300 Wh/kg in energy density, making the development of the next-generation rechargeable batteries crucial[56,57]. Lithium-sulfur (Li-S) batteries have drawn widespread attention due to their high energy density of 2600 Wh/kg and theoretical capacity of 1675 mAh/g[58]. Moreover, the materials used for cathodes of Li-S batteries are mainly carbon and elemental sulfur, which have abundant reserves in nature, making them more cost-effective and more environmentally friendly compared to traditional lithium-ion batteries[59]. However, Li-S batteries haven't been commercialized due to the following issues: (1) Poor conductivity of sulfur (10^{-30} S/cm) leads to low utilization of the active material, resulting in actual capacity not reaching the theoretical capacity[60]. (2) The electrochemical reactions of Li-S batteries involve several intermediates, namely lithium polysulfides (LiPSs, Li_2S_n, $1 \leqslant n \leqslant 8$)[61]. Soluble long-chain LiPSs (Li_2S_n, $4 \leqslant n \leqslant 8$) migrate in the electrolyte, causing a loss of active material that is not effectively oxidized or reduced at the electrode[62]. Additionally, if soluble LiPSs are reduced to insoluble short-chain LiPSs (Li_2S and Li_2S_2) and deposit on the surface of anode, lithium dendrite growth occurs, which damages the solid electrolyte interphase (SEI) layer on the lithium anode[63]. This problem is known as the "shuttle effect", leading to the loss of active material, reduction in battery capacity, cycle life and Coulombic efficiency, and in severe cases, it may even cause short circuits of batteries[64]. (3) The low density of Li_2S results in an electrode volume expansion of up to 80% during the charging and discharging process[65,66]. These issues lead to the actual

energy density and capacity of Li-S batteries falling far below the theoretical values, hindering their large-scale production and commercial application.

Researchers tried to explore and utilize the Li-S chemistry, even before the commercialization of LIBs. However, the efforts were not successful, and the performance results were not adequate. After important advancements in nanotechnology and the ability of its involvement in the manufacturing processes, researchers started to reconsider Li-S chemistry, in hope of overcoming the problems that come with this alternative battery chemistry. **Figure 1.4** shows the increase in the total number of publications and the total number of issued patents related to Li-S batteries. To address the issues of Li-S batteries, the modification of the cathode is crucial. An effective approach is to design the structure of carbon materials in the cathode, such as using carbon nanotubes, porous carbon fibers, and hollow carbon nano-spheres[67-69], to physically confine sulfur molecules and accommodate volume expansion during the cycling process. This method can play a certain role in limiting the shuttle effect. However, due to the size of soluble LiPSs (> 0.8 nm), precise control of nanoscale pores in carbon materials is essential[70]. Strictly limiting the pore size below 0.8 nm is necessary to effectively confine LiPSs within the cathode. To make this happen, the preparation process is often complex and challenging. An alternative, relatively simpler approach is to trap LiPSs on the cathode by chemical absorption. Some metal oxides, such as Al_2O_3, TiO_2, MnO_2, and ZnO, have demonstrated good adsorption capability for LiPSs[71-74]. Therefore, adding trace amounts of these metal oxide materials to the cathode proves effective in restricting the shuttle effect. For example, Ge et al. demonstrated the use of a

chemical synthesis method to coat MnO_2 on the surface of sulfur particles, which mitigated the shuttle effect[75]. However, this solution-based synthesis method is prone to introducing impurities, leading to less absorption than theoretical values. To reduce the impurities introduced during coating, some researchers opted for atomic layer deposition (ALD) for coating process[76-79]. However, ALD is costly and has slow deposition rates. Additionally, the low melting point of sulfur (112.8°C) necessitates low-temperature ALD process, which significantly affects the morphology and performance of the deposited material, and even causes unsuccessful deposition[80]. Thus, choosing an appropriate deposition method and a coating material with strong absorption capacity for LiPSs is importance.

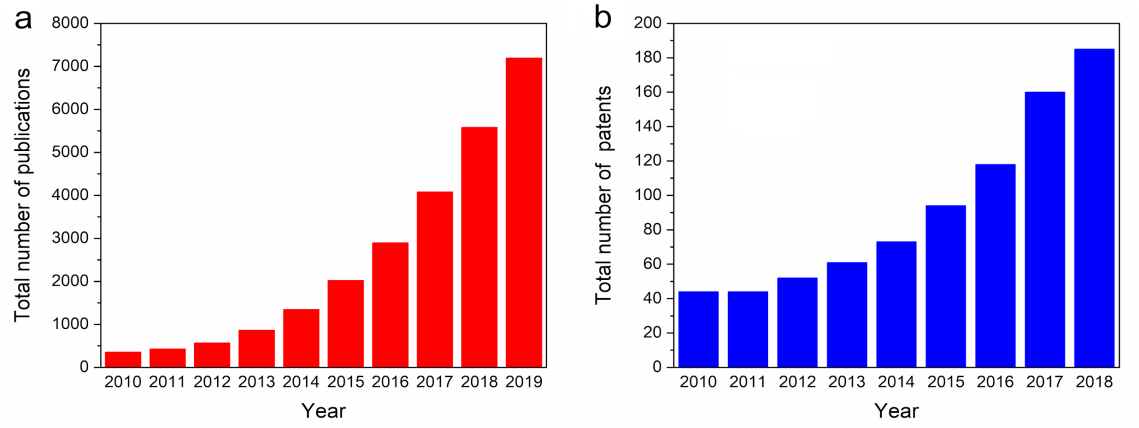


Figure 1.4 Total number of (a) publications and (b) patents related to Li-S batteries after 2010. In the last ten years, the total number of publications has increased by a factor of 20, whereas the total number of issued patents has increased by a factor of four. The numbers listed here are obtained from Web of Science for the publications and Google Scholar for the issued patents.

1.5 Backgrounds of Solid Electrolyte and All-solid-state Battery

In solid-state batteries (SSBs), solid electrodes and electrolytes are used in replacement of typical liquid or polymer gel electrolytes of conventional batteries (i.e., LIBs). This solid-state technology has existed for quite some time and is proposed to solve many issues presented by the use of liquid electrolytes in batteries[81]. Therefore, in the past two decades, much research has been targeted at improving SSBs for ubiquitous use in critical technologies, such as EVs. Liquid electrolyte batteries were projected to reach practical limits of energy density given the predicted constraints of materials technology development[82-84], making them less than favorable for use in energetically demanding technologies such as EVs. Moreover, SSBs pose numerous advantages over LIBs, including increased energy storage density, life-cycle, charging speed, and increased safety due to higher thermal stability (reducing flammability and volatility). In fact, Dudney et. al predicted that SSBs would soon have the potential to be widely used in applications such as energy storage, as well for powering electronics devices and automobiles in 2015[85]. While we have not reached this point, the evolution of SSBs is ongoing and promising; eight years later, with the continued global focus on decreasing fossil fuel dependency, we see major efforts toward applying solid-state technology. Particularly in the automobile industry, leading companies and research labs work toward implementing SSBs in EVs[86]. Nonetheless, much progress is still to be made, as many issues challenge the scale-up of production and actual advantageousness of SSBs over conventional batteries[87]. Specifically, performance enhancements that will make SSBs more cost effective per kWh, such as increasing power density for more efficient

charging, as well as increasing life-cycle by solving mechanical issues, are key to the realization of SSBs in modern technology.

High volumetric and gravimetric energy densities are important in determining the competitiveness of batteries in EV applications and, currently, respective densities of 770 Wh L^{-1} and 260 Wh kg^{-1} are reported for high-performing liquid electrolyte batteries. SSB volumetric energy densities are reportedly around 430 Wh L^{-1}, or 63% of that of liquid electrolyte batteries, thus there is room for improvement[88]. Developments are promising though, as one startup – the Qing Tao Energy Development Co. – claims successful production of solid-state lithium batteries with gravimetric energy density of 400 Wh/kg with their 100 MWh per year production plant (as of 2019), which they begun expanding to 10 GWh as of March 2022 to increase production[89]. The United States Advanced Battery Consortium (USABC) reports that an 80% charge reached within 15 minutes is necessary for EVs to be considered competitive against conventional combustion engine vehicles[90]. LIBs implemented in EVs, (i.e., Porsche Taycan, Tesla Model 3) reportedly reach 80% charging in 23-27 minutes, while SSBs are claimed to meet the USABC requirement, charging within just 15 minutes. Moreover, LIBs show degradation in just 1000 cycles, while SSBs are more durable – in 5000 cycles, they are able to retain 90% of the original battery capacity, due to lessened mechanical strain. Finally, a major performance advantage of SSBs over LIBs is their avoidance of liquid electrolytes and carbon anodes, which not only limit battery energy density, but are also highly flammable[24,91-93]. Thus, use of the liquid electrolyte poses safety risks, arguably

the most important consideration for EVs[94,95]. SSBs inherently address safety concerns in many ways, as shown in **Figure 1.5**.

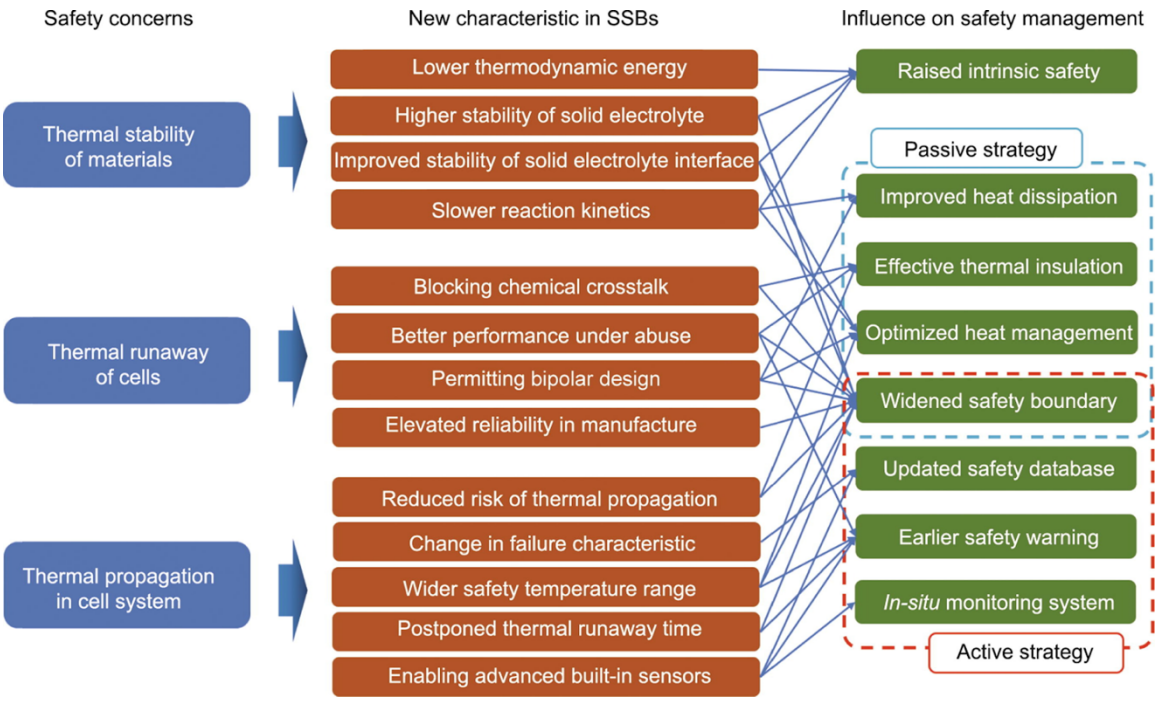


Figure 1.5 Modifications in material and battery design across material, cell, and system tiers offer fresh avenues for enhancing safety strategies in SSBs[96].

Theoretically, SSBs offer cost advantages over conventional liquid electrolyte batteries, a large component of their attractiveness. For instance, infiltration, formation, and conventional production steps for liquid electrolyte batteries are not required[83]. Such factors, in addition to significantly lower materials costs, ultimately work to make SSBs very cost effective. To this end, sulfide-electrolyte SSBs, designed for 6 GWh/year production output, are reportedly most cost-effective[97]. However, challenges of implementation specifically target the economical advantageousness of SSBs, and thus further exploration is required to actually realize the cost advantages. First, the materials

used are an area of concern. Studies report that scale-up efforts are particularly prone to failure if the supply chain is constrained, as well as if cell integration warrants costly and impractical materials manufacturing[97]. Additionally, conventional processing and manufacturing techniques will need to be uniquely tailored to SSBs' specific requirements, and integrating new procedures may present high upfront costs to further challenge implementation. Specifically, SSBs are reactive to humidity and oxygen, must be manufactured with high-pressures and temperatures, and possess unique mechanical properties which may pose manufacturability and safety-related complications[88]. Additionally, pertinent areas must be to be addressed as large-scale implementations ramp up, such as underdeveloped efforts to curb toxicity and make SSB technologies more sustainable (recyclable). Finally, defects and stability issues are prevalent and make SSB implementation imperfect[98]. Mainly, dendrite formation, which causes short-circuiting, is a problem that was expected to be curbed with use of solid rather than liquid electrolytes but is found to persist and is being extensively studied. Other mechanical failure mechanisms which threaten effectiveness and lifecycle life of SSBs include electrolyte fracture toughness, bending, and cracking.

As mentioned, SSBs were formerly assumed to be inherently resistant to dendrite formation compared to liquid electrolyte batteries, and although the mechanisms of dendrite growth are not necessarily similar between the two batteries, dendrites indeed persist in implementation of SSBs. This does not mean that the issue is as elusive as in LIBs[99,100]. In SSBs, dendrite formation is reportedly more predictable, thus can be managed through mindful materials engineering. Specifically, dendrites are shown to

form when pores in the solid electrolyte are “interconnected”; therefore, this issue may be combated by increasing the density of the electrolyte by altering the grain boundaries of the material, such as by sintering[101]. Other material options are also being researched. At Massachusetts Institute of Technology, mixed ion-electronic conductor tubes were filled with lithium (anode), such that the tubes are coated and thus are protected from the electrolyte, preventing dendrite formation. Furthermore, this tube’s 3D honeycomb architecture permits expansion/contraction that occurs during the charge/discharge process to avoid cracking[102]. Such research on the optimization of anode and cathode materials can also help improve the energy density of SSBs. Coating techniques, such as those explored by MIT, can improve thermodynamic instabilities. Other ways to improve energy density are being explored with thinner electrolyte layers, which are also reported to improve the economic attractiveness of SSBs, Therefore, these improvements are multifaceted, and future work should continue to search for optimized materials, manufacturing methods, and life-time properties of SSBs, as this will not only make them more efficient, but also more cost effective in comparison to liquid electrolyte batteries.

Chapter 2

2 Experimental Methods and Instrumentation

2.1 HfO_2-based Artificial Cathode Electrolyte Interphase (CEI) through Atomic Layer Deposition for High Voltage Stable NMC811 Electrode

2.1.1 Cathode Preparation

All the chemicals were used in their original, as-received state. The 5 wt% poly(vinylidene fluoride) (PVDF, Mv ~ 534000, Sigma-Aldrich) solution was prepared by adding 2g PVDF into 38g *N*-methyl-2-pyrrolidone (NMP, 99.9%, AME Energy) solvent, and keep stirring for 24 hours until PVDF is fully dissolved. Before preparing the slurry of the cathode, 5g NMC811 powders (Particle Size (D50): 9-15 μm, MSE Supplies) were dried in a muffle furnace (1100 Compact Muffle Furnace, MTI Corporation) at 140°C for 2 hours in the glovebox (Vigor) filled with Argon gas. To achieve a homogeneous slurry, 5g pre-heated NMC811 powders, 0.278g carbon black (Super P, 99+%, Alfa Aesar), and 5.556g 5 wt% PVDF solution were sequentially loaded into the container under Argon atmosphere in the glovebox, then the sealed container was transferred to the slurry mixer (Model ARE-310, Thinky Corporation) for mixing of 9.5 minutes at 2000 rpm and defoaming of 30 seconds at 2200 rpm, repeat the mixing and defoaming process for 3 times. The mass ratio of NMC811 powders, carbon black, and

PVDF is 9:0.5:0.5. The NMC811 cathode was prepared by coating the prepared slurry on Aluminum foil (99.45%, Alfa Aesar) through a film applicator (Compact Tape Casting Coater, MTI Corporation), then the cathode foil was kept in vacuum oven (KJ Group, MTI Corporation) at 60°C with the pump on overnight until fully dried.

2.1.2 HfO_2 Coating via ALD

HfO_2 thin film was deposited on the NMC811 cathodes using the Cambridge Nanotech Savannah 100 ALD System at 200°C. Tetrakis(diethylamido)hafnium(IV) ($Hf[N(C_2H_5)_2]_4$) and deionized H_2O were used as precursors. The N_2 was served as carrier and purge gas, the deposition process follows the following procedure: 0.01s H_2O pulse, 30s purge, 0.1s $Hf[N(C_2H_5)_2]_4$ pulse, 30s purge. During the purge process, the N_2 flow rate was kept at 20 sccm, and the reactor pressure was 0.6-0.8 Torr. The procedure was repeated for 55 cycles.

2.1.3 Material Characterizations

To characterize the morphology and elemental concentration and distribution for the surface of HfO_2 coated cathodes, scanning electron microscopy (SEM, NovaNanoSEM 450) and energy-dispersive X-ray spectroscopy (EDS, NovaNanoSEM 450) were utilized. During the test, accelerating voltage was kept at 20 kV, the spot size was 4.5, the emission current was 67 μA, and the gun pressure was kept at around 1.03×10^{-7} Pa. Before SEM tests, Pt/Pd sputter coating (Sputter Coater, GRESSINGTON 108 Auto) was applied to the cathode surfaces for 60s with current of 20 μA to enhance

the surface conductivity. To further analyze the elemental composition of HfO_2 coated cathodes, Raman spectroscopy (Horiba, LabRam HR800) test was performed. During Raman test, the wavelength of the utilized laser was 532 nm and the grating was 1800 gr/mm.

2.1.4 Coin Cell Assembly

NMC811 coin cells (CR2032) were assembled in the Argon-filled glovebox with H_2O content of less than 0.1 ppm and O_2 content of less than 1 ppm. The assembly procedure for the coin cells is outlined as follows before electrochemical tests. Firstly, a 16 mm-diameter lithium disk was positioned inside the negative electrode cell case, and 60 µL of 1 M $LiPF_6$ Ethylene carbonate (EC)/ Diethyl carbonate (DEC) (EC: DEC=1:1 vol.%) electrolyte was dripped onto it. Subsequently, a 19 mm-diameter polypropylene separator was added on top of the anode, followed by another 60 µL of the electrolyte. Then, the pre-cut uncoated or HfO_2-coated cathode disk with 16 mm diameter was placed on the top of the separator, and the mass loading of active materials in the prepared cathode was around 14 mg/cm^2. Next, a spacer, spring, and positive electrode case were placed in order, the cell was sealed by the electric crimper machine (MSK-160D, MTI Corporation). The last step was to keep the sealed cells in the fume hood overnight to allow the electrolyte to permeate the electrode materials completely.

2.1.5 Electrochemical Measurements

Bio-Logic (BCS 810) battery tester was used for all the electrochemical tests. To evaluate the charge/discharge performance, the galvanostatic tests were applied to the cells, the voltage range of the tests is from 2.5V to 4.6V vs Li/Li^+, and three condition cycles with 0.56 mA constant current rate (0.1C) were applied before the tests to achieve stable electrode/electrolyte interphase. For the galvanostatic tests, 2.8 mA (0.5C) and 5.6 mA (1C) were employed for 200 cycles separately based on 200 mAh/g for NMC811. To evaluate the rate performance of the cells, galvanostatic tests with 0.1C, 0.2C, 0.5C, 1C, 2C, 5C, and 0.1C current rates were employed for 5 cycles of each rate. To analyze the electrochemical reactions and polarization of cells during charging and discharging, cyclic voltammetry (CV) tests were used between 2.5V to 4.6V vs Li/Li^+ after 100 and 200 cycles of galvanostatic tests (1C) with the scan rate of 0.1 mV/s. To further confirm the Diffusion Coefficient D_{Li^+} of uncoated and HfO_2 coated cells, the cells were swept from 3V to 4.5V vs Li/Li^+ with scan rate from 0.1 mV/s to 1.0 mV/s by the step size of 0.1 mV/s. To analyze the internal resistance of the batteries, electrochemical impedance spectroscopy (EIS) tests were applied after condition, 100 and 200 cycles of galvanostatic tests (0.5C), the perturbation amplitude of the tests is 10 mV, and the frequency range is 10 mHz to 10 kHz.

2.1.6 Post-Mortem Characterization

After 200 cycles of charging and discharging at 0.5C, HfO_2 coated and uncoated cells are opened by hydraulic crimping machine (MSK-110, Corporation) in the glovebox

filled with Argon gas. The cycled electrodes were immersed and washed by dimethyl carbonate (DMC, ≥99%, Sigma-Aldrich). After overnight drying, the completely dried electrodes were observed for surface morphology and elemental distribution using SEM and EDS. The thickness of the cathodes was also measured, and the acceleration voltage during testing was 30 kV, with a chamber pressure of 1.28×10^{-2} Pa. It is noteworthy that during the transfer of the lithium anodes from the glovebox to the SEM chamber, the electrodes need to be stored in a sealed container filled with Argon gas to prevent oxidation.

2.2 Rational Design of SnO_2 Thin Film Coated Cathode with Function of Entrapping Polysulfides for Performance Enhanced Li-S Batteries

2.2.1 Preparation of Sulfur/Porous Carbon Cathodes

All the chemicals were used as received. Sulfur/Porous Carbon composites were synthesized by manual grinding and mixing 3g of sublimed sulfur (~100 mesh, 99.5%, Alfa Aesar) and 2g of porous carbon (2000 m^2/g, ACS Material, LLC). Then, the well-mixed sample was transferred to the glovebox (Vigor) filled with Argon gas and heated in a muffle furnace (1100 Compact Muffle Furnace, MTI Corporation) at 155°C for 6 hours with a heating rate of 5°C/min. After natural cooling, the powders were manually ground again. To prepare the slurry for cathodes, 2.105g of poly(acrylic acid) (PAA, Mv ~ 450000, Sigma-Aldrich) was added to 40g of *N*-methyl-2-pyrrolidone (NMP, 99.9%, AME Energy), and stirred for 24 hours until PAA is completely dissolved, resulting in a

5wt% PAA solution in NMP. Then, 2g of Sulfur/Porous Carbon composites and 0.57g acetylene black (99.9%, Alfa Aesar) were sequentially added to 5.17g of 5wt% PAA in NMP solution, with a mass ratio of Sulfur/Porous Carbon composites, acetylene black, and PAA as 7:2:1, followed by the addition of 7g of NMP and stirring for 3 days. The homogeneous slurry was coated on Aluminum foil (99.45%, Alfa Aesar) by a film applicator (Compact Tape Casting Coater, MTI Corporation), then placed in an air oven at 60°C overnight, resulting in completely dried Sulfur/Porous Carbon cathodes.

2.2.2 SnO_2 Thin Film Coating

SnO_2 film was deposited on Sulfur/Porous Carbon cathodes using the magnetron sputtering method, utilizing the AJA ORION 5 Sputtering System. After transferring the sample to the main chamber, the gas pressure was maintained at $5\text{-}10\times10^{-6}$ Torr. During the deposition process, a continuous flow of 10 SCCM Argon gas was maintained to stabilize the pressure at 4.4 mTorr. The final heating power and ramp-up time of the heater were set to 45 W and 300 s, respectively. The power type of the magnetron sputtering is RF, and this configuration yields a deposition rate of approximately 0.625 Å/s for SnO_2 target. To achieve a homogenous SnO_2 film deposition, the cathode was rotated as 40% speed during the deposition process.

2.2.3 Materials Characterization

The surface morphology of the electrode was characterized by scanning electron microscopy (SEM, NovaNanoSEM4 50). The testing was performed with accelerating

voltage of 20 kV and spot size of 3.5. During testing, the chamber pressure was approximately 3×10^{-3} Pa, the gun pressure was about 2.5×10^{-7} Pa, and the emission current was around 75 μA. Elemental analysis of the electrode surface was conducted by energy dispersive X-ray spectroscopy (EDS, NovaNanoSEM 450) and Raman spectroscopy (Horiba, LabRam HR800). Raman testing utilized a laser wavelength of 532 nm. The weight ratio of sulfur and carbon in cathode was determined through thermogravimetric analysis (TGA, Mettler Toledo) with increasing temperature by 5°C/min from room temperature to 700°C in flowing Argon gas. To acquire higher magnification image of cathode and thickness of SnO_2 coating layer, scanning transmission electron microscopy (STEM, Tian Themis 300, ThermoFisher Scientific) with Super-X Energy Dispersive X-ray Spectrometer system was utilized. To prepare the thin film for STEM image, the SnO_2 coated cathode was pressed to around 40 μm, then DualBeam scanning electron microscope and focused ion beam (FIB, Quanta 200i 3D, ThermoFisher Scientific) with gallium ion source were used as following procedures. Firstly, the interested area of SnO_2 coated cathode was deposited by platinum and carbon protective layers of 6 μm and 2 μm respectively. Then, an $18 \times 2 \times 5$ μm lamella was milled by 150 pA - 30 nA and polished by 5 nA at 30 kV from the sample and transferred to Omniprobe needle by platinum deposition. Finally, the Omniprobe manipulator transferred the cut lamella to TEM grid, and a final milling at 5 kV was applied to acquire the thin sample of 80 nm thickness for STEM. STEM was tested at 300 kV accelerating voltage and the EDS mapping was acquired at a beam current of 550 pA. The visual adsorption test was proceeded in the Argon atmosphere. Li_2S_6 solution was prepared by

adding sublimed sulfur (~100 mesh, 99.5%, Alfa Aesar) and Li_2S (MSE Supplies) with a molar ratio of 5:1 into a solution mixed by 1,3-dioxolane (DOL, Sigma-Aldrich) and 1,2-dimethoxyethane (DME, Sigma-Aldrich) solvents with 1:1 volume ratio. The mixture was stirred overnight under 60°C to get a Li_2S_6 solution (0.5 M). Then the Li_2S_6 solution was diluted to 2 mM by the DOL/DME solvent (1:1 in volume) for comparison. 50 mg SnO_2 (pre-dried under 80°C overnight) powders was added to 6 mL Li_2S_6 (2 mM). After 7 hours static adsorption, two solutions are compared.

2.2.4 Coin Cell Assembly

Li-S coin cells (CR2032) were assembled in Argon-filled glovebox (H_2O content <0.1 ppm, O_2 content <1 ppm) before electrochemical tests. The assembly process of the coin cells is described as follows. Firstly, a 16 mm-diameter lithium disk was placed inside the negative electrode cell case, and 45 μL of electrolyte was dripped onto it. The electrolyte was prepared by mixing 1,3-dioxolane (DOL, Sigma-Aldrich) and 1,2-dimethoxyethane (DME, Sigma-Aldrich) solvents, the volume ratio is 1:1; 1 M bis(trifluoromethane)sulfonimide (LiTSFI, Sigma-Aldrich) and 1 wt% $LiNO_3$ was added and fully dissolved by stirring for 2 days. Then, a 19 mm-diameter polypropylene separator was placed on the top of the counter electrode, and 45 μL of the electrolyte was added. Next, an uncoated or SnO_2-coated cathode was cut into a 16 mm-diameter circular disk and placed on the top of separator, the loading of active materials of the prepared cathode is 3 mg/cm^2. By using this recipe, the electrolyte/sulfur ratio of Li-S cells was maintained at around 15 μL/mg to provide enough wetting of electrode materials without

increasing the free migration of active materials[95]. Subsequently, a spacer, spring and positive electrode cell case were added, and the coin cell was sealed by a crimper (MSK-160E, MTI Corporation). Finally, the cells were left undisturbed overnight to allow the electrolyte to fully permeate the electrode materials.

2.2.5 Electrochemical Measurements

All the electrochemical tests were performed by Bio-Logic (BCS 810) battery tester. For the galvanostatic charge/discharge tests, constant current rates of 1 mA (0.1C) and 5 mA (0.5C, 1C = 1675 mA/g) was employed for 100 cycles, with a voltage range of 1.7 V to 2.8 V vs Li/Li^+. Before tests, all batteries were charged and discharged for 3 condition cycles with 500 μA (1/20C) to achieve stable electrode/electrolyte interphases. To evaluate the rate performance of uncoated and 5 nm SnO_2 coated Li-S cells, galvanostatic tests with 0.1C, 0.2C, 0.5C and 1C current rate were applied after 3 condition cycles. Cyclic voltammetry (CV) tests were applied between 1.7 V and 2.8 V vs Li/Li^+ after 1^{st}, 5^{th} and 15^{th} galvanostatic tests (0.5C), the scan rate is 0.1 mV/s. To analyze the internal resistance and polarization of batteries, electrochemical impedance spectroscopy (EIS) and galvanostatic intermittent titration technique (GITT) were used. EIS was performed before, after condition cycles, and after 100 cycles of galvanostatic tests (0.1C and 0.5C), the perturbation amplitude is 10 mV and the frequency range is 20 mHz to 10 kHz. GITT was applied after condition cycles with 5 mA current rate of 10 min charge/discharge pulse and 10 min relaxation time.

2.2.6 Computational Methods

The DFT was used to carried out the simulations with generalized gradient approximations in the form of Perdew−Burke−Ernzerhof for the electron−electron exchange and correlation interactions[103] and implemented in the Quantum Espresso program package[104,105]. The electron-ion interactions were represented by ultrasoft pseudopotentials[106]. An electronic smearing technique was used to improve the accuracy of the calculations[107]. The kinetic energy and augmented density cutoff were chosen to be 600 and 60 Ry, respectively. The Broyden−Fletcher− Goldfarb−Shanno (BFGS) algorithm [108] was used to optimize the studied structures. Converge criteria were selected as 0.01 eV Å−1 and 10−6 eV/atom for the maximum force and energy on each atom, respectively. The SnO_2 surface was adjoined with a vacuum region larger than 15 Å to minimize the interactions along the z-direction. Among various initial configurations, the most stable configurations were discussed to understand the interactions between Li_2Sn and SnO_2 surface. The binding energies (E_b) are determined by the **Equation 2.1**.

Equation 2.1

$$E_b = \left(E_{Li_2S_n} + E_{SnO_2-surface}\right) - E_{Li_2S_n-SnO_2}$$

where $E_{Li_2S_n}$ is the total energy (E_T) of Li_2S_n, $E_{SnO_2-surface}$ is the E_T of the SnO_2-surface and $E_{Li_2S_n-SnO_2}$ is the E_T of the Li_2S_n− SnO_2 system.

2.3 Interfacial Modification of Li_6PS_5Cl-based All-solid-state Li-S Batteries by Al_2O_3 Nano-layer Deposition

2.3.1 Li_6PS_5Cl-based Cathode Preparation

The cathode powders were prepared by solid-state reaction method. 150 mg sublimed sulfur (~100 mesh, 99.5%, Alfa Aesar), 50 mg carbon nanotubes (CNT, Alfa Aesar) and 300 mg Li_6PS_5Cl solid electrolyte (MSE Supplies, 325 mesh) were added into the sealed ball mill jar in the glovebox filled with Argon gas. Then the powers were ball milled (MSK-SFM-1, MTI corporation) at 400 rpm for 10 hours with 10 mins clockwise and 10 mins counterclockwise rotations. After that, the sealed ball mill jar was transferred into the glovebox again and the well-mixed materials were poured out into a ceramic jar with lid. Next, the materials were heated in a muffle furnace (1100 Compact Muffle Furnace, MTI Corporation) at 155°C for 12 hours with a heating rate of 5°C/min. After natural cooling, the powders were manually ground again.

2.3.2 Al_2O_3 Coating via Atomic Layer Deposition

Al_2O_3 thin film was deposited on the Indium foil using the Cambridge Nanotech Savannah 100 ALD System at 130°C. Trimethylaluminum (TMA) and deionized H_2O were used as precursors. The N_2 was served as carrier and purge gas, the deposition process follows the following procedure: 0.025s H_2O pulse, 20s purge, 0.015s TMA pulse, 20s purge. During the purge process, the N_2 flow rate was kept at 20 sccm, and the reactor pressure was 0.6-0.8 Torr. The procedure was repeated for 55 cycles.

2.3.3 Materials Characterization

To characterize the morphology and elemental concentration and distribution for the surface of Al_2O_3 coated anode before cycling, scanning electron microscopy (SEM, NovaNanoSEM 450) and energy-dispersive X-ray spectroscopy (EDS, NovaNanoSEM 450) were utilized. During the test, accelerating voltage was kept at 20 kV, the spot size was 3.0, the emission current was 67 μA, and the gun pressure was kept at around 1.03×10^{-7} Pa.

2.3.4 Symmetrical Cell Assembly

The symmetrical cell was assembled in the glovebox filled with Argon gas. The lithium foil was cut into 5 mg disks, and the coated or uncoated indium foil was cut into 100mg disks before pressing. Then, a lithium disk and an indium disk were put into the 10 mm diameter die in order, please note the coated surface was facing towards the solid electrolyte. Then 150 mg Li_6PS_5Cl solid electrolyte was added into the die, press the materials gently by hand. Finally, add another indium disk and lithium disk sequentially into the die. Apply 300 MPa pressure to create a symmetrical pellet and move it to the Swagelok cell inside of the glovebox. The Swagelok cell was connected to the battery tester by wires.

2.3.5 Electrochemical Measurements

All the electrochemical tests were performed by Bio-Logic (VMP3) battery tester. The galvanostatic charge/discharge tests were performed for the symmetrical cells, constant current rate of 20 μA were employed for 999 cycles with 10 mins charging and discharging. After 150 cycles, EIS tests were performed with 10 mV amplitude and 10 mHz to 1 MHz frequency range.

2.3.6 Post-Mortem Characterization

After 999 cycles of 10 min charging and discharging at 20 μA, the electrodes of Al_2O_3 coated and uncoated symmetrical cells are taken out from the Swagelok cell in the glovebox filled with Argon gas. Then, the electrodes were observed for surface morphology and elemental distribution using SEM and EDS. The acceleration voltage during testing was 30 kV, with a chamber pressure of 1.28×10^{-2} Pa. It is noteworthy that during the transfer of the electrodes from the glovebox to the SEM chamber, the electrodes need to be stored in a sealed container filled with Argon gas to prevent oxidation.

Chapter 3

3 HfO_2-based Artificial Cathode Electrolyte Interphase (CEI) through Atomic Layer Deposition for High Voltage Stable NMC811 Electrode

3.1 HfO_2 ALD Deposition Analysis

The process of HfO_2 thin film coating on NMC811 cathode via ALD is illustrated in **Figure 3.1**. Firstly, the gaseous $Hf[N(C_2H_5)_2]_4$ precursor was pulsed into the reaction chamber, chemically adsorbing on the electrode through reactions with hydroxyl groups on the surface. The excess precursor was then removed during the purge process using N_2. Subsequently, water vapor was pulsed into the reaction chamber, creating more hydroxyl groups on the surface, and allowing for the continued growth of HfO_2. Excess water vapor was removed by N_2 during the purge process, and this cycle was repeated. The coating thickness can be determined by controlling the total number of ALD cycles, please refer to **Section 2.1.2** for detailed procedure. The surface morphology of the HfO_2 coated NMC811 cathode is shown in **Figure 3.2a**, the cathode is composed of quasi-spherical NMC811 particles with diameters ranging from 9 to 15 μm, uniformly dispersed in a continuous conductive carbon matrix linked by PVDF binder before cycling, the HfO_2 protective layer on the surface of the cathode is coated evenly, which is confirmed by the EDS mapping (**Figure 3.2b-3.2g**). Compared with the uncoated

NMC811 cathode (**Figure 3.3a, 3.3c-3.3h**), there are no significant differences in the surface morphology and distribution of Ni, Co, Mn, C, and O elements on the surface of cathodes, which indicates that the HfO_2 ALD coating doesn't alter the morphology of the cathode. The EDS spectra of the HfO_2 coated NMC811 cathode, as shown in **Figure 3.2h**, reveal distinct peaks of Hf element on the surface of the coated cathode at 1.66, 7.92, and 8.26 keV, while other element peaks remain consistent with the uncoated cathode **(Figure 3.3b)**. This confirms the successful deposition of the HfO_2 thin film on the cathode surface. Due to the low carbon content on the surface of the cathodes, Pt/Pd sputter coating was applied to the cathode surfaces before SEM testing to enhance conductivity in order to obtain clear SEM images, therefore, both coated and uncoated cathode surfaces exhibit peaks of Pt and Pd in the EDS spectra. **Figures 3.4 and 3.5** display the elemental concentration and statistical error in weight percentage for the surfaces of the HfO_2 coated and uncoated cathodes, revealing 1.2% of Hf on the coated cathode, while the uncoated one lacks Hf. Besides Hf, other elemental contents show minor differences in the weight percentage, likely due to variations in the number and diameter of selected regions of NMC811 particles. To gain more information about the composition of the uncoated and HfO_2 coated cathode, Raman spectroscopy was performed, and the results are shown in **Figure 3.2i**. Six Lorentzian peaks of the NMC811 surface layers are deconvoluted for both spectra, they are assigned to E_g (Ni) = 452 cm^{-1} and A_{1g} (Ni) = 560 cm^{-1} in red, E_g (Co) = 531 cm^{-1} and A_{1g} (Co) = 549 cm^{-1} in green, and E_g (Mn) = 589 cm^{-1} and A_{1g} (Mn) = 609 cm^{-1} in grey[109]. For the HfO_2 coated cathode, one characteristic band appears at approximately 481 cm^{-1}, which might be

ascribed to the transverse optical (T_O) phono of HfO_2[110,111]. Due to the overlapping Raman peaks at 560 cm^{-1} and 589 cm^{-1}, the characteristic band of longitudinal optical (L_O) phonons of HfO_2 at around 570 cm^{-1} is not prominent[110]. The results of Raman spectroscopy support the findings of EDS testing, confirming the successful deposition of HfO_2 on the surface of the NMC811 cathode, and the Raman spectra further indicate that part of the deposited HfO_2 through ALD is amorphous.

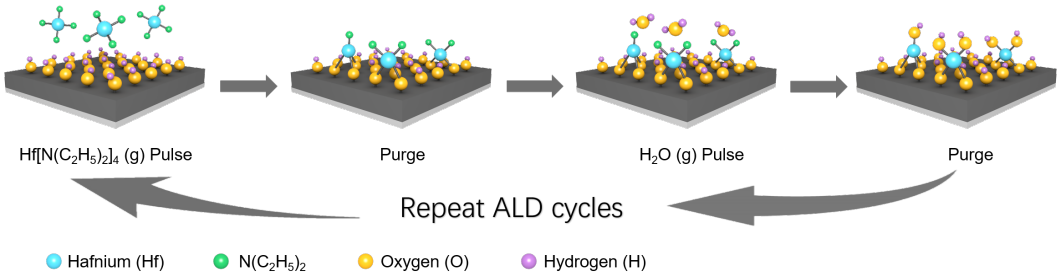


Figure 3.1 Schematic depiction of HfO_2 thin film coating procedure on NMC811 cathode by ALD.

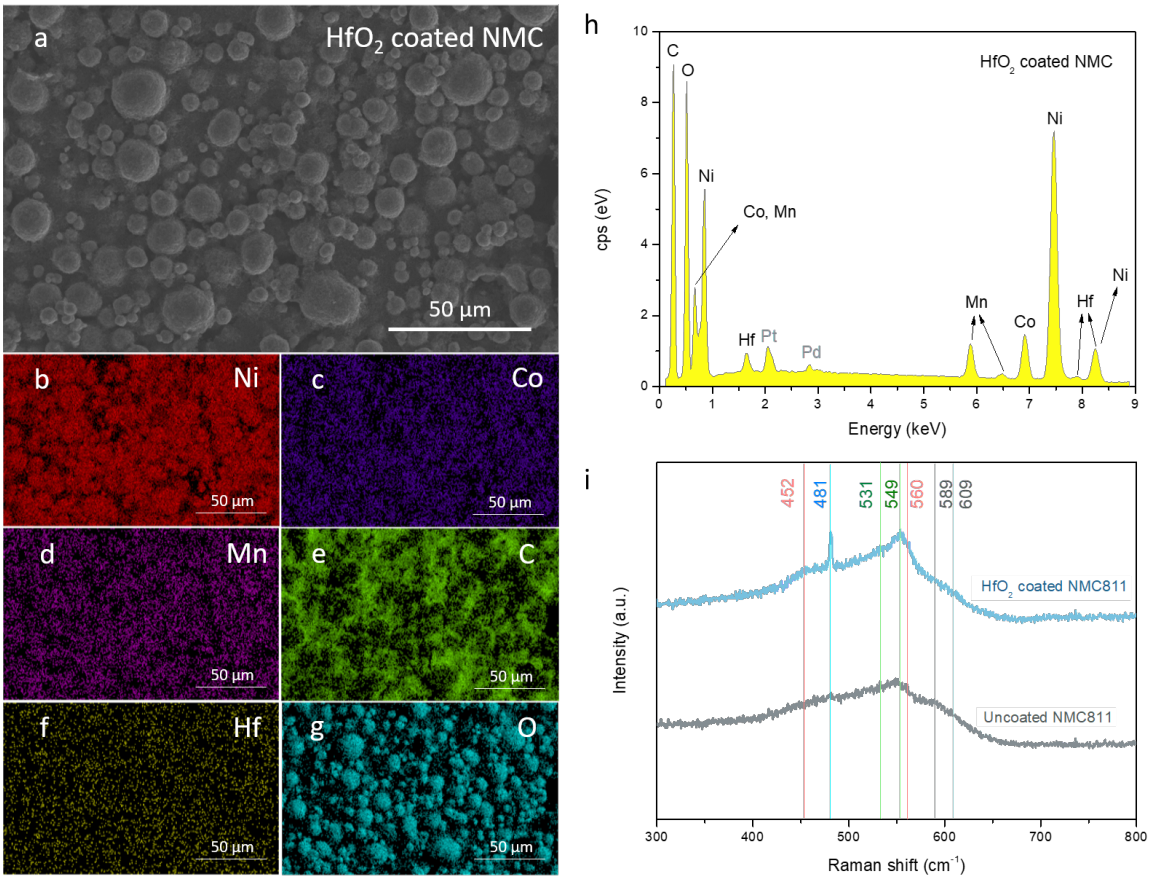


Figure 3.2 (a) SEM image; (b-g) corresponding elemental mapping of Ni, Co, Mn, C, Hf and O; (h) EDS spectra and (i) Raman spectra for HfO_2 coated NMC811 cathode before cycling.

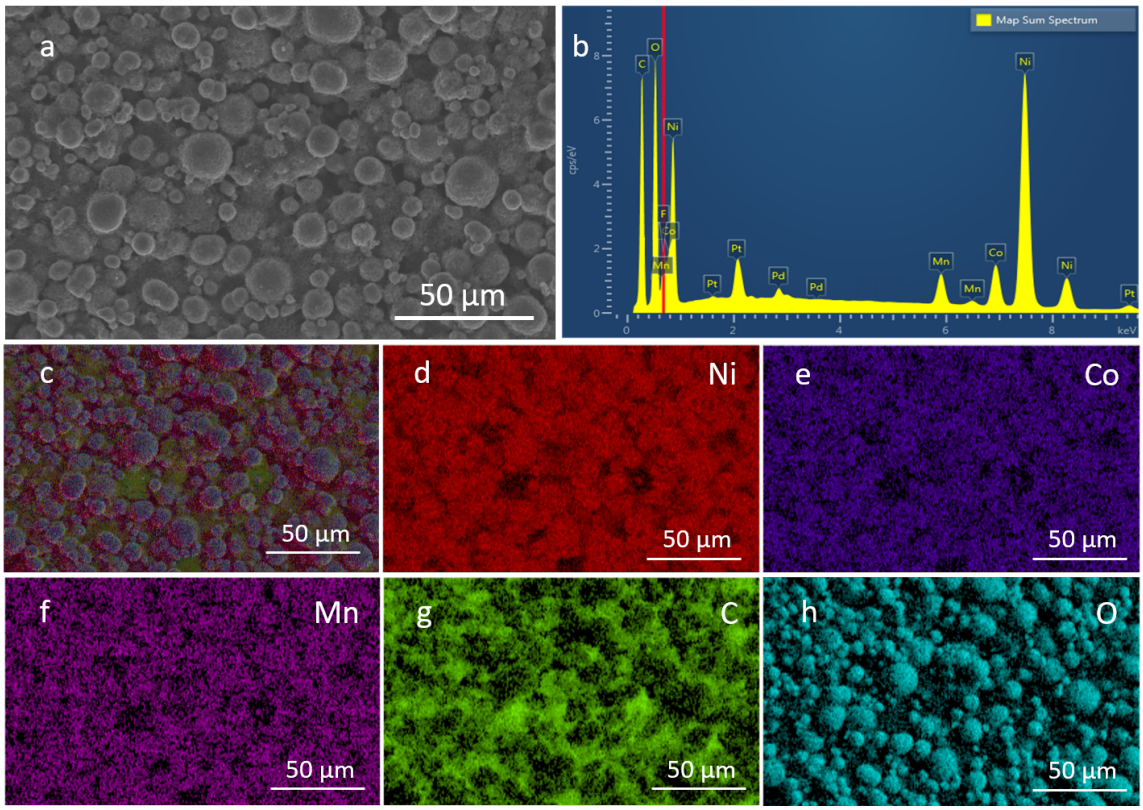


Figure 3.3 (a) SEM image; (b) EDS spectra; (c) elemental mapping and (d-h) corresponding elements of Ni, Co, Mn, C and O for uncoated NMC811 cathode before cycling.

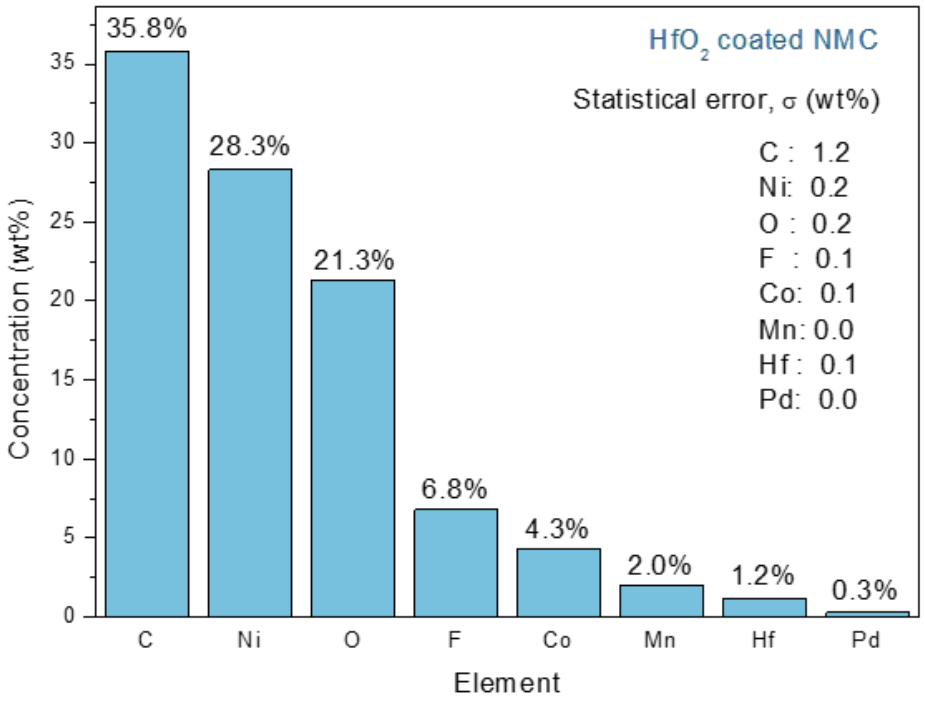


Figure 3.4 Elemental concentration in weight percent and statistical error of C, Ni, O, F, Co, Mn, Hf, Pd for HfO_2 coated NMC811 cathode before cycling.

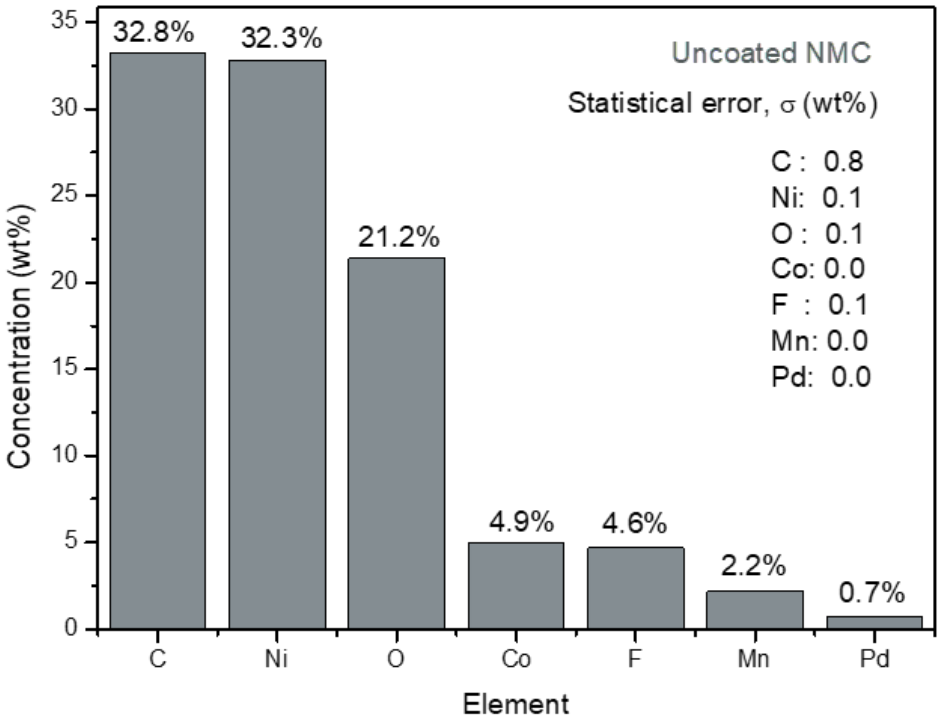


Figure 3.5 Elemental concentration in weight percent and statistical error of C, Ni, O, Co, F, Mn, Pd for uncoated NMC811 cathode before cycling.

3.2 Cycling and Rate Test Results

The cycling performance of HfO_2 coated and uncoated NMC811 half-cells at 0.5C is shown in **Figure 3.6a**. The voltage range for each cycle is from 2.5V to 4.6V, and the figure shows fully discharged specific capacity. For HfO_2 coated cell, the specific capacities after the first and 200th cycles are 202.80 mAh/g and 152.87 mAh/g, resulting in a capacity retention of 75.38%. For uncoated cell, the specific capacities after the first and 200th cycles are 191.89 mAh/g and 62.15 mAh/g, with a capacity retention of 32.39%. After 200 cycles, the coated cell exhibits a specific capacity 2.46 times that of the uncoated cells, with a 42.99% higher capacity retention, indicating that the HfO_2

artificial CEI coating enables stable cycling of NMC811 cathode cells under high cutoff voltage and wide electrochemical window for long cycling. It's noteworthy that HfO_2 coated cell experiences a slight initial capacity drop in the first 5 cycles, possibly due to the extra time required for electrochemical activation and formation of a stable CEI layer with HfO_2 thin film coating, which slows down the diffusion of electrolyte into the cathode at the beginning of cycles, this also explains the slight capacity rebound after 5 cycles. The charge-discharge profiles for the first, 100^{th}, and 200^{th} cycles of HfO_2 coated and uncoated cells are shown in **Figures 3.6b** and **3.6c**. Coated cell exhibits a slight overpotential increase from the first to the 100^{th} cycle, while uncoated cells show a significant increase. Additionally, at the first, 100^{th}, and 200^{th} cycles, uncoated cells consistently exhibit much higher overpotential than HfO_2 coated cells, with the gap widening as the cycle number increases. This suggests that the HfO_2 thin film coating significantly enhances the cycle stability of NMC811 half-cells, it may be due to the coating preventing the contact between the electrolyte and the highly delithiated NMC811 cathode, thereby weakening the occurrence of interfacial side reactions[112-114].

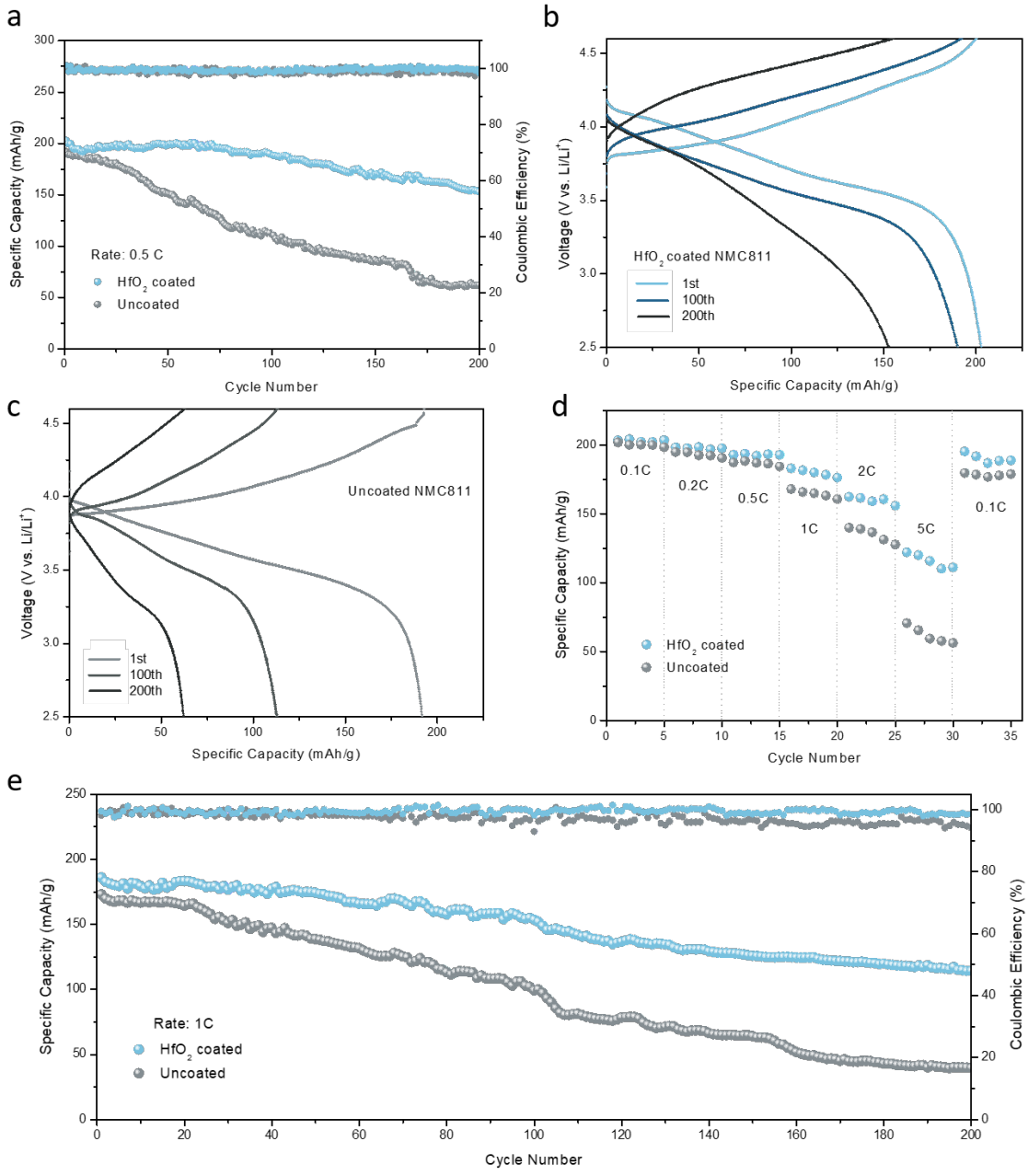


Figure 3.6 (a) Cycling performance of HfO_2 coated and uncoated NMC811 cells at 0.5C over 200 cycles; Charge-discharge profiles for (b) HfO_2 coated and (c) uncoated NMC811 cells after 1st, 100th and 200th cycles at 0.5C; (d) Rate performance of HfO_2 coated and uncoated NMC811 cells from 0.1 to 5C; (e) Cycling performance of uncoated and HfO_2 coated NMC811 cells at 1C over 200 cycles.

To explore the rate performance, HfO_2 coated and uncoated cells were cycled for 5 cycles at rates of 0.1, 0.2, 0.5, 1, 2, and 5C, then back to 0.1C. As shown in **Figure 3.6d**, the fully discharged specific capacity difference between coated and uncoated cells gradually increases with increasing current density. At a 5C charge-discharge rate in the fifth cycle, the specific capacity of the uncoated cell is 56.32 mAh/g, while that of the coated cell is 111.14 mAh/g, which is 1.97 times that of the uncoated cell. After returning to a 0.1C rate, the specific capacity of the coated cell is 195.31 mAh/g, which is 96.05% of that of the first cycle (203.35 mAh/g). The specific capacity of the uncoated cell is 179.69 mAh/g, which is 88.97% of that of the first cycle (201.97 mAh/g), 7.08% less than the coated cell. This indicates that the HfO_2-rich thin CEI film can provide good capacity retention performance under rapid lithium-ion insertion/extraction, which may be due to the stability of the HfO_2 coated NMC811 cathode structure[115]. To examine the long cycling performance differences between HfO_2 coated and uncoated NMC811 half-cells at high rate, the cells were cycled 200 times at 1C, and the results are shown in **Figure 3.6e**. When cycled at 0.5C, both coated and uncoated cells show no significant decline in Coulombic efficiency during cycling. When the rate is increased to 1C, the Coulombic efficiency of coated cells drops from 99.59% to 98.64% after 200 cycles, resulting in a 0.95% decrease. However, the Coulombic efficiency of uncoated cells decreases from 98.28% to 94.19%, leading to a 4.09% decrease, which is more significant. This demonstrates that the HfO_2 coated cell exhibits higher cycling efficiency at high rate and voltage. After 200 cycles at 1C, the specific capacity of uncoated cell decreases from 173.05 mAh/g to 39.53 mAh/g, with a capacity retention of only 22.84%.

The specific capacity of HfO_2 coated cell decreases from 185.99 mAh/g to 114.32 mAh/g, with a capacity retention of 61.47%, which is 38.63% higher than that of uncoated cell. This proves that the HfO_2 coating can significantly enhance the capacity retention performance of NMC811 batteries under high-rate, long cycling conditions, maintaining the stability of the NMC811 electrode.

3.3 Cyclic Voltammetry and Li ion Diffusion Coefficient Results

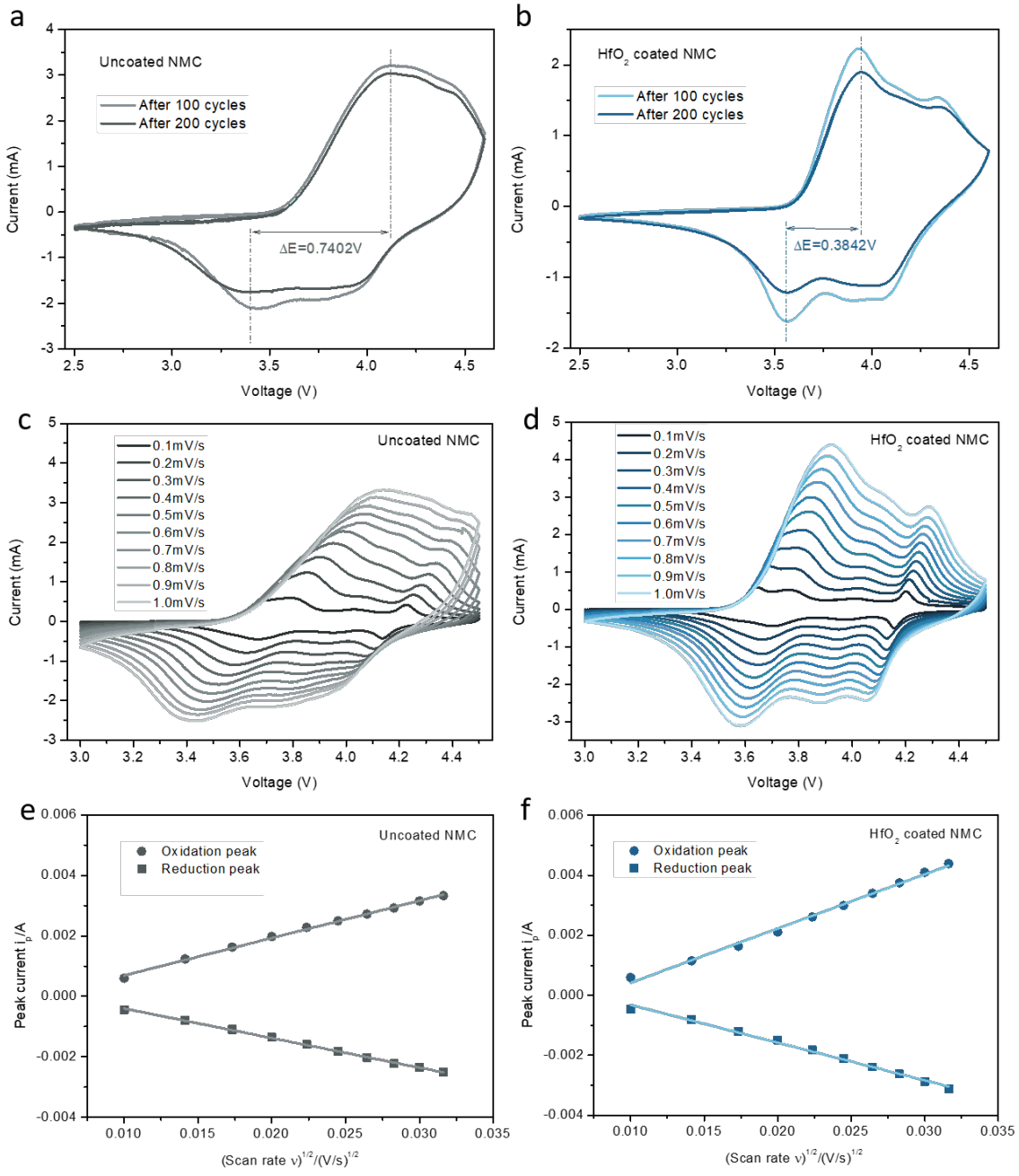


Figure 3.7 CV curves of (a) uncoated and (b) HfO_2 coated NMC811 cells after 100th and 200th cycles at 1C; CV curves with increased scan rates from 0.1 mV/s to 1.0 mV/s for (c) uncoated and (d) HfO_2 coated NMC811 cells; Line plots of oxidation and reduction peak current obtained from (c) and (d) as a function of the square root of scan rate for (e) uncoated and (f) HfO_2 coated NMC811 cells.

CV plots were measured after 100 and 200 cycles at 1C to further explore the long cycling performance of NMC811 electrodes under high pressure, as shown in **Figures 3.7a** and **3.7b**. The peak intensities of both coated and uncoated cells decrease with increasing cycle numbers, indicating a capacity decline consistent with the cycling behavior in **Figure 3.7**. The uncoated cell exhibits a significant oxidation peak, a noticeable reduction peak, and a less distinct reduction peak. After 200 cycles, compared to after 100 cycles, the main reduction peak shifts from 3.43V to 3.39V, indicating an increase in overpotential and severe polarization of the cells with increasing cycle numbers[95]. HfO_2 coated cell shows three oxidation peaks after both 100 and 200 cycles, located at 3.94V, 4.15V, and 4.34V respectively, with the middle peak being weaker in intensity. According to Reference[112,113,116], these three peaks represent phase transitions of NMC811 material from hexagonal (H1) to monoclinic (M), then from M to hexagonal (H2), and finally from H2 to H3, respectively. The reduction peaks in the coated cell decreased from three to two due to the weakened peak intensities, making the middle peak less prominent. Compared with the coated cell, the uncoated cell only exhibits one large oxidation peak, with the H2→H3 transition missing, possibly indicating irreversible phase changes in the cells. Studies suggest that if the cycling voltage exceeds 4.2V, lithiation of NMC811 electrodes undergoes an irreversible transition from layered phase ($R\bar{3}m$) to disordered spinel phase ($Fd\bar{3}m$) and then to a NiO-like rock salt phase ($Fm\bar{3}m$)[116-118]. The formula is as follows, where M represents Ni and Co, [O] represents active oxygen intermediates:

Equation 3.1

$$MO_2 \text{ (layered)} \rightarrow M_3O_4\text{(spinel)} + [O]$$

Equation 3.2

$$M_3O_4\text{(spinel)} \rightarrow MO\text{(rocksalt)} + [O]$$

This series of phase transitions not only reduces M^{4+} to M^{2+}, leading to capacity loss, but also generates active oxygen intermediates, resulting in oxygen evolution, electrolytes consumption, gas generation, and impedance increase[115,116]. The coated cell exhibits three distinct oxidation reduction peaks, indicating fewer irreversible phase transitions, higher electrochemical reversibility, and a more stable structure of NMC811 under high voltage. After 200 cycles, the voltage differences between main oxidation and reduction peaks of uncoated and coated cells are 0.74V and 0.38V, respectively, which proves that the HfO_2 artificial CEI reduces polarization in NMC811 cells under high-voltage cycling.

To further explore the electrochemical reaction differences between HfO_2 coated and uncoated cells under high-voltage and high-rate conditions, CV tests were employed from 0.1 to 1 mV/s, with a step size of 0.1 mV/s. As the scan rate increases, both oxidation and reduction peaks shift to higher and lower potentials, respectively. However, coated cells exhibit significantly less shifting, indicating a lower degree of polarization[52,113]. Additionally, the uncoated cell exhibits three obvious reversible oxidation-reduction peaks at low scan rates, while the results at high scan rates align with **Figure 3.7a**, confirming irreversible phase transitions in the NMC811 electrode structure under high voltage and rates. In contrast, the coated cell shows three sets of obvious reversible oxidation and reduction peaks at both low and high scan rates, indicating that

the HfO_2 based artificial CEI enables the NMC811 electrode to maintain structural stability even under high-voltage and high-rate conditions. It's worth noting that at low scan rates around 0.1/0.2 mV/s in **Figures 3.7c and 3.7d**, there are four oxidation peaks. This is because the $Co^{4+/3+}$ redox couple contributes a small portion of the capacities, causing the first oxidation peak to split into two overlapping peaks during the H1→M transition[119,120]. To calculate the Li ion diffusion coefficient of the cells, the maximum current density of the oxidation and reduction peaks in **Figures 3.7c** and **3.7d** as the function of the square root of the scan rate was plotted to obtain **Figures 3.7e** and **3.7f**. The Li ion diffusion coefficients are calculated by the Randles-Sevcik equation at 25°C[121-126]:

Equation 3.3

$$i_p = 2.69 \times 10^5 \times n^{3/2} \times A \times D_{Li^+}^{1/2} \times C \times \nu^{1/2}$$

Where i_p represents the peak maxima (A); n represents the number of charge carriers; A represents the surface area of electrode; D_{Li^+} represents the Li ion diffusion coefficient; C represents the Li ion concentration in NMC811 cathode; ν represents the scan rate. Since all coefficients except i_p and ν are constants, **Equation 3.3** can be rewritten as:

Equation 3.4

$$i_p = slope \times \nu^{1/2}$$

Where the slope can be obtained from **Figure 3.7e** and **3.7f**, and then the Li ion diffusion coefficient calculation formula is as follows:

Equation 3.5

$$D_{Li^+} = \left(\frac{slope}{2.69 \times 10^5 \times n^{3/2} \times A \times C}\right)^2$$

Where n=1; A=2.01 cm^2; C=0.0236 mol/cm^3, which is calculated by C=density/molecular weight, the density and molecular weight of NMC811 is 2.3 g/cm^3 and 97.28 g/mol. The slopes and calculation results are shown in **Table 3.1**.

	Oxidation Peak		Reduction Peak	
Uncoated NMC811	Slope	0.1236	Slope	-0.09769
	Diffusion Coefficient D_{Li}^+ (cm^2/s)	9.34828E-11	Diffusion Coefficient D_{Li}^+ (cm^2/s)	5.83976E-11
HfO_2 coated NMC811	Slope	0.18063	Slope	-0.12577
	Diffusion Coefficient D_{Li}^+ (cm^2/s)	1.99652E-10	Diffusion Coefficient D_{Li}^+ (cm^2/s)	9.67941E-11

Table 3.1 Slope obtained from Figure 3.7e and f for uncoated and HfO_2 coated NMC811 cells and calculated Li ion Diffusion Coefficient D_{Li}^+ (cm^2/s).

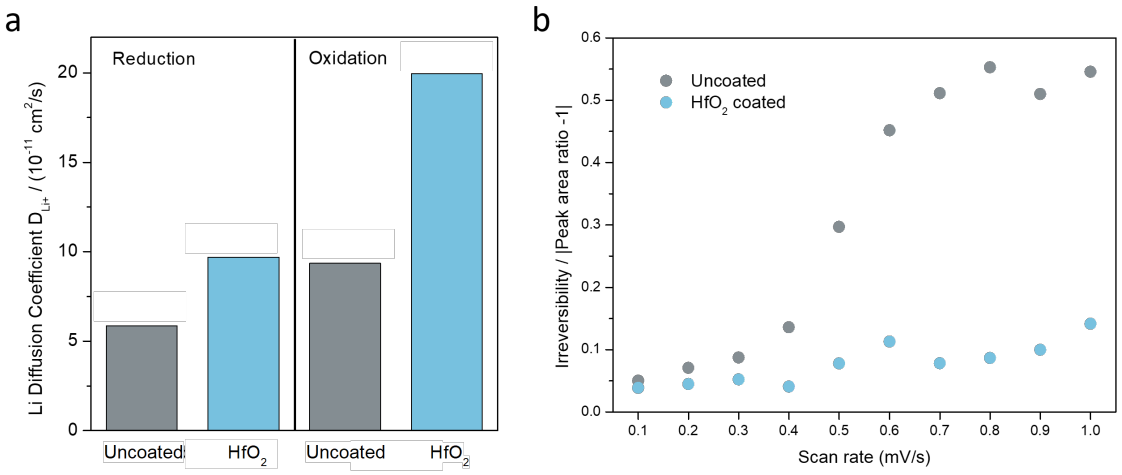


Figure 3.8 (a) Estimated Li ion Diffusion Coefficient (D_{Li}^+) of uncoated and HfO_2 coated NMC811 cells; (b) The relative electrochemical reversibility of uncoated and HfO_2 coated NMC811 cells, which is calculated by the absolute value of the ratio of oxidation and reduction peak area minus one as the function of the scan rate.

The Li ion diffusion coefficients for the oxidation and reduction electrochemical processes of coated and uncoated cells are shown in **Figure 3.8a**. For the oxidation half-reaction, the D_{Li^+} of the uncoated cell is approximately 9.35×10^{-11} cm^2/s, while that of the coated cell is 2.00×10^{-10} cm^2/s, which is 2.14 times greater than the uncoated cell. For the reduction half-reaction, the D_{Li^+} of the uncoated cell is approximately 5.84×10^{-11} cm^2/s, while that of the coated cell is 9.68×10^{-11} cm^2/s, which is 1.66 times greater than the uncoated cell. This indicates that the HfO_2 based artificial CEI significantly enhances the Li ion conductivity and diffusion kinetics in NMC811 batteries. This may be attributed to the HfO_2 coated cell having a smaller internal impedance, which will be further explained in the following EIS section[121,124,125]. In addition to Li ion diffusion coefficients, the electrochemical reversibility of the cells can also be roughly compared based on **Figures 3.7c** and **3.7d**. Based on some recent studies, it is suggested that the electrochemical reversibility of batteries is high when the areas of oxidation and reduction peaks are approximately equal[127-129]. The peak areas and area ratios are shown in **Table 3.2**, and the absolute value of the ratio of oxidation and reduction peak areas minus one as a function of scan rate is shown in **Figure 3.8b**. The smaller the value, the more the areas of oxidation and reduction peaks equal, indicating higher battery reversibility. At low scan rates, both HfO_2 coated and uncoated cells exhibit relatively good electrochemical reversibility. However, as the scan rate increases, the reversibility of the uncoated cell significantly deteriorates, while the coated cell still maintains the good reversibility. This also supports the results of Li ion diffusion kinetics.

	Scan rate (mV/s)	Area of Oxidation Peak	Area of Reduction Peak	Area ratio (O/R)	Area ratio (O/R)-1
Uncoated NMC811	0.1	0.2335	0.2223	1.050382	0.050382
	0.2	0.4835	0.4516	1.070638	0.070638
	0.3	0.7011	0.6448	1.087257	0.087257
	0.4	0.8979	0.7904	1.136007	0.136007
	0.5	1.1880	0.9161	1.296802	0.296802
	0.6	1.5070	1.0380	1.45183	0.45183
	0.7	1.6790	1.1110	1.511251	0.511251
	0.8	1.8090	1.1650	1.55279	0.55279
	0.9	1.9600	1.2980	1.510015	0.510015
	1	2.0620	1.3340	1.545727	0.545727
HfO_2 coated NMC811	0.1	0.1903	0.1980	0.961111	0.038889
	0.2	0.4332	0.4146	1.044863	0.044863
	0.3	0.6664	0.6334	1.0521	0.0521
	0.4	0.8783	0.8439	1.040763	0.040763
	0.5	1.0810	1.0030	1.077767	0.077767
	0.6	1.2800	1.1500	1.113043	0.113043
	0.7	1.4600	1.3540	1.078287	0.078287
	0.8	1.6410	1.5101	1.086683001	0.086683
	0.9	1.7830	1.62101	1.099931524	0.099931
	1	1.9390	1.6983	1.141729965	0.141729

Table 3.2 Area of oxidation and reduction peaks obtained from Figure 3.7c and 3.7d for uncoated and HfO_2 coated NMC811 cells.

3.4 Electrochemical Impedance Spectroscopy Results

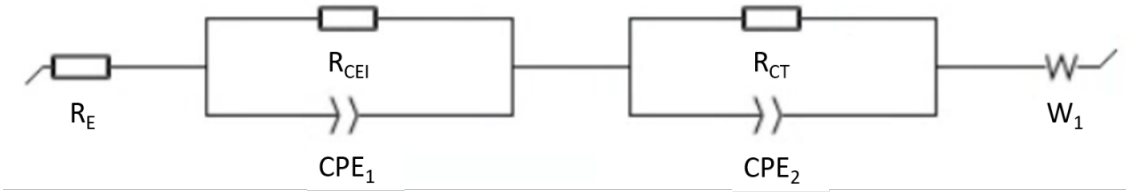


Figure 3.9 Equivalent circuit fitting model for NMC811 batteries. R_E represents the electrolyte resistance, R_{CEI} represents the cathode/electrolyte interphase resistance and R_{CT} represents the charge transfer resistance at the interface between electrode and electrolyte. CPE_1 and CPE_2 are the constant phase related to the double layer capacitance. W_1 is Warburg resistance associated with diffusion of Li^{+}[130-133].

To explain the differences between HfO_2 coated and uncoated cells in Li ion diffusion coefficients and electrochemical reversibility, EIS testing was performed to explore the internal resistance of batteries. The equivalent circuit fitting model is shown in **Figure 3.9**, where R_E represents the electrolyte resistance, related to the intersection of the plot in the high frequency region and the x-axis; R_{CEI} and R_{CT} represent the cathode/electrolyte interphase resistance and charge transfer resistance at the interface between electrode and electrolyte respectively, associated with the semicircles in the plot; W_1 is the Warburg resistance associated with the diffusion of Li^{+}, related to the sloping line in the low frequency region[130-133]. The Nyquist impedance plots after conditioning, 100 and 200 cycles, are shown in **Figure 3.10a-3.10c**, indicating that the internal resistance of the cells gradually increases during cycling. EIS fitting results are shown in **Figure 3.10d** and **Table 3.3**, it shows that the HfO_2 coated cell exhibits smaller R_E, R_{CEI}, and R_{CT} compared to the uncoated cell during the cycling process, suggesting that the coated cell has lower internal resistance and better ion and electron transfer performance. It is noteworthy that after 200 cycles, the R_{CEI} of the uncoated cell is 446.10 Ω, while that

of the coated cell is only 61.28 Ω, which is 13.7% of the uncoated cell. Such a significant difference may be due to the HfO_2 based artificial CEI reducing irreversible phase transitions on the surface of NMC811 particles, effectively passivating the interface and preventing parasitic reactions at the interface. Typically, some residual lithium compounds from the synthesizing process are present on the surface of NMC811 particles, which can be oxidized to produce carbon dioxide and oxygen when the voltage exceeds 4.2V, as shown below[116]:

Equation 3.6

$$Li_2O - 2e^- \rightarrow \frac{1}{2}O_2 + 2Li^+$$

Equation 3.7

$$LiOH - 2e^- \rightarrow \frac{1}{2}O_2 + Li^+ + H^+$$

Equation 3.8

$$Li_2CO_3 - 2e^- \rightarrow \frac{1}{2}O_2 + CO_2 + 2Li^+$$

The oxidation/reduction intermediates further consume electrolytes, leading to an increase in battery resistance; meanwhile, gas generation occurs, causing a decrease in the electrochemical reversibility of batteries and resulting in cracks. During the cycling, the electrolyte in the battery reacts with residual water, generating hydrofluoric acid (HF), which further attacks secondary NMC811 particles and causes more cracks. The reaction is shown as follows:

Equation 3.9

$$LiPF_6 + H_2O \rightarrow LiF \downarrow + POF_3 + 2HF$$

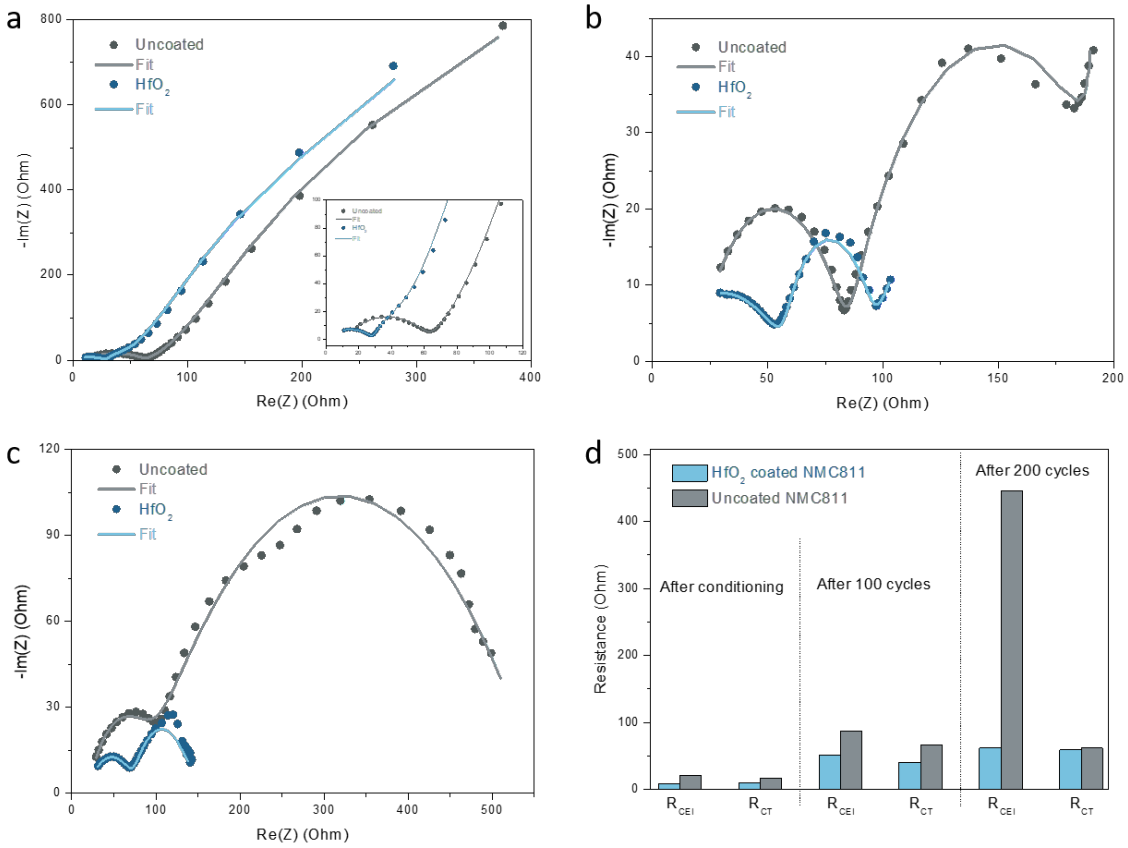


Figure 3.10 EIS plots of uncoated and HfO_2 coated NMC811 cells (a) after condition cycles, (b) after 100 cycles, and (c) after 200 cycles at 0.5C from 2.5V to 4.6V; (d) Fitting results of impedance spectra for R_{CEI} and R_{CT}.

		R_E (Ω)	R_{CEI} (Ω)	R_{CT} (Ω)
Uncoated NMC811	After condition	15.61	19.94	16.96
	After 100 cycles	19.09	87.26	66.55
	After 200 cycles	25.09	446.1	61.34
HfO_2 coated NMC811	After condition	4.292	8.809	9.818
	After 100 cycles	6.863	50.93	40.16
	After 200 cycles	17.02	61.28	59.03

Table 3.3 EIS fitting results for uncoated and HfO_2 coated NMC811 batteries after conditions, after 100 cycles and after 200 cycles at 0.5C.

3.5 Scanning Electron Microscopy Results

The schematic diagram of the degradation of uncoated NMC811 electrodes under high-voltage cycling is shown in **Figure 3.11a**. During the long cycling process under high voltage, cracks are generated within and between NMC811 crystals, by-products are increased, and the electrode becomes much thicker. While the HfO_2 coated battery has a thin, robust CEI layer, which effectively resists HF attacking and reduces electrode cracking, as shown in **Figure 3.11b**. And these are the origins of higher ion diffusion rates and better electrochemical reversibility of coated batteries under high voltage during long cycling, which lead to higher capacity retention and cycling efficiency. To verify this mechanism, batteries were opened after 200 cycles for SEM and EDS testing. As shown in **Figures 3.11c** and **3.11d**, the coated cathode has fewer surface cracks compared with the uncoated cathode, the corresponding EDS results are shown in **Figure 3.12-3.15**. According to the results in **Tables 3.4** and **3.5**, the HfO_2 coated battery has more oxygen and less fluorine concentrations on the cathode surface, supporting the stronger resistance to HF of the HfO_2 based CEI layer. The thickness of cycled NMC811 electrodes is shown in **Figures 3.11e** and **3.11f**, the coated electrode is 63.0 μm and the uncoated electrode is 107.9 μm, the uncoated electrode is 1.71 times thicker and has more cracks. In addition to cracking caused by CO_2 and O_2 generated by parasitic reactions, the uncoated NMC811 undergoes an irreversible phase transition from a layered spinel to a rock salt phase under high voltage, leading to significant volume changes in the crystal unit cell, resulting in cracking of NCM811 secondary particles[116-118]. These cracks exacerbate the parasitic reactions and expose more surfaces of electrodes, this vicious circle greatly increases the

surface resistance of the NMC811 electrode and severely limits Li ion diffusion[52]. HfO_2 based artificial CEI layer effectively prevents electrode cracking and parasitic reactions, thereby improving the electrochemical performance of the NMC811 electrode. SEM images of Li anode surfaces after cycling are shown in **Figures 3.11g and 3.11h**, the anode of the uncoated cell is covered with lithium dendrites, while the one paired with the coated NMC811 electrode is smoother with no obvious dendrites. The EDS results for the surface of cycled Li anodes are shown in **Figures 3.16** and **3.17**, and the corresponding elemental concentrations are shown in **Tables 3.6** and **3.7**. The results indicate that the oxygen concentration on the surface of the Li anode paired with the uncoated cathode is 66.2 wt%, while that of the coated battery is only 47.4 wt%, 18.8 wt% less than the uncoated battery. This suggests a significant reduction in the oxidation degree of the Li anode in coated batteries, possibly due to the fewer active oxygen intermediates generation and parasitic reactions of NMC811 cathodes, which support the results of EIS and SEM.

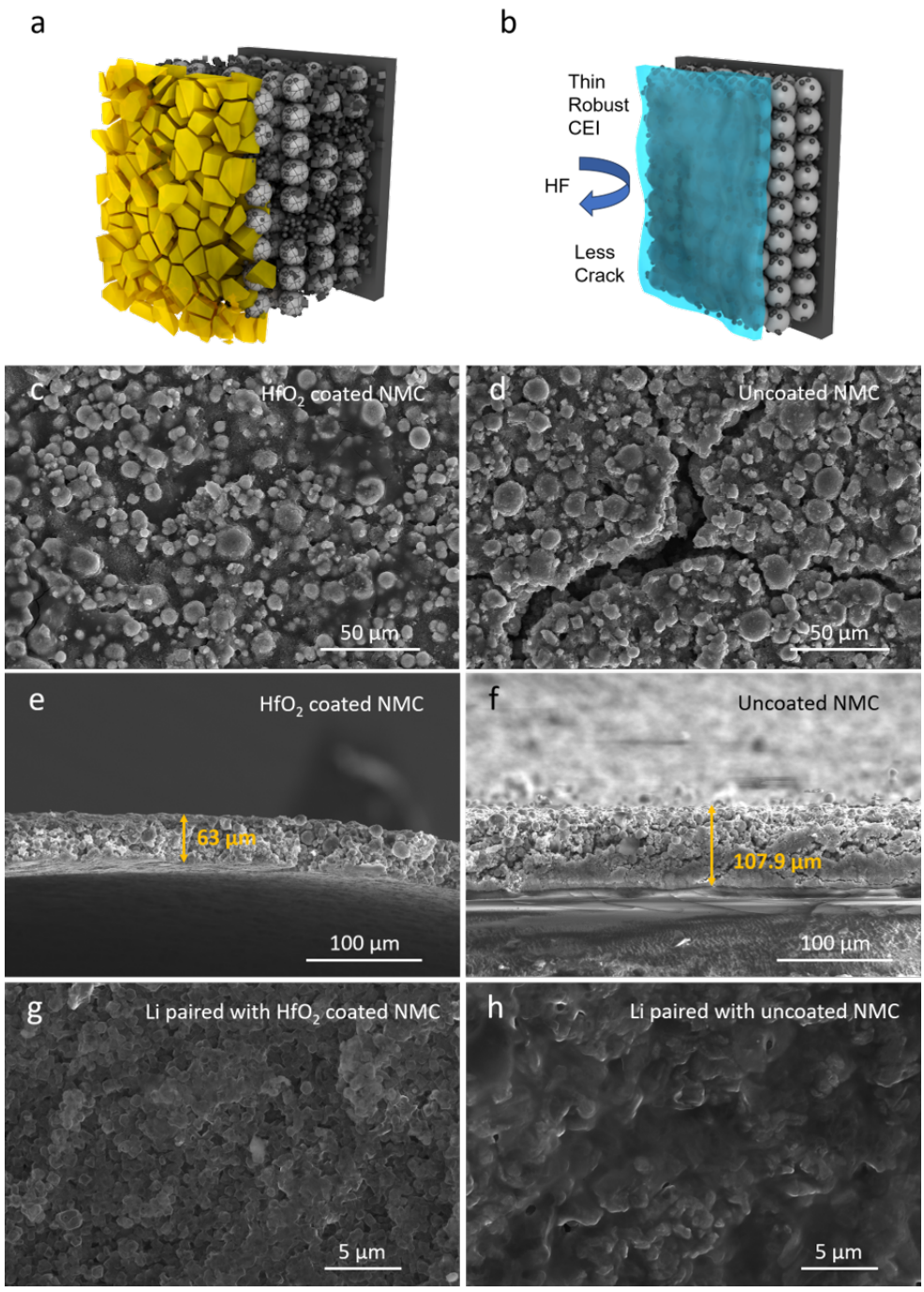


Figure 3.11 Scheme of the degradation mechanisms of (a) uncoated and (b) HfO_2 coated NMC811 electrodes; Surface morphologies of (c) uncoated and (d) HfO_2 coated NMC811 electrodes after 200 cycles at 0.5C; Cross sections of (e) uncoated and (f) HfO_2 coated NMC811 electrodes after 200 cycles at 0.5C; Surface morphologies of lithium anodes of (g) uncoated and (h) HfO_2 coated NMC811 electrodes after 200 cycles at 0.5C.

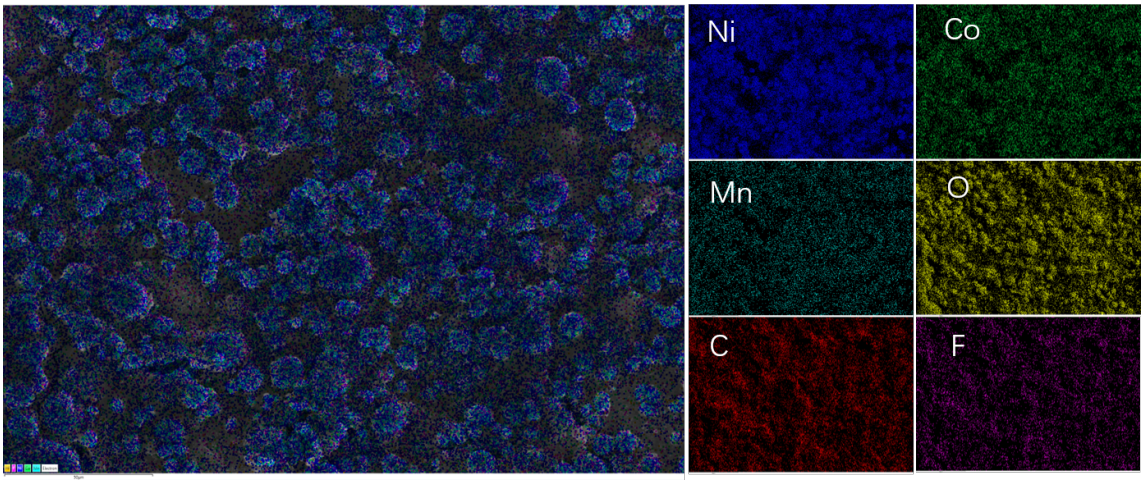


Figure 3.12 Elemental mapping and corresponding elements of Ni, Co, Mn, O, C and F for HfO_2 coated NMC811 cathode after 200 cycles at 0.5C.

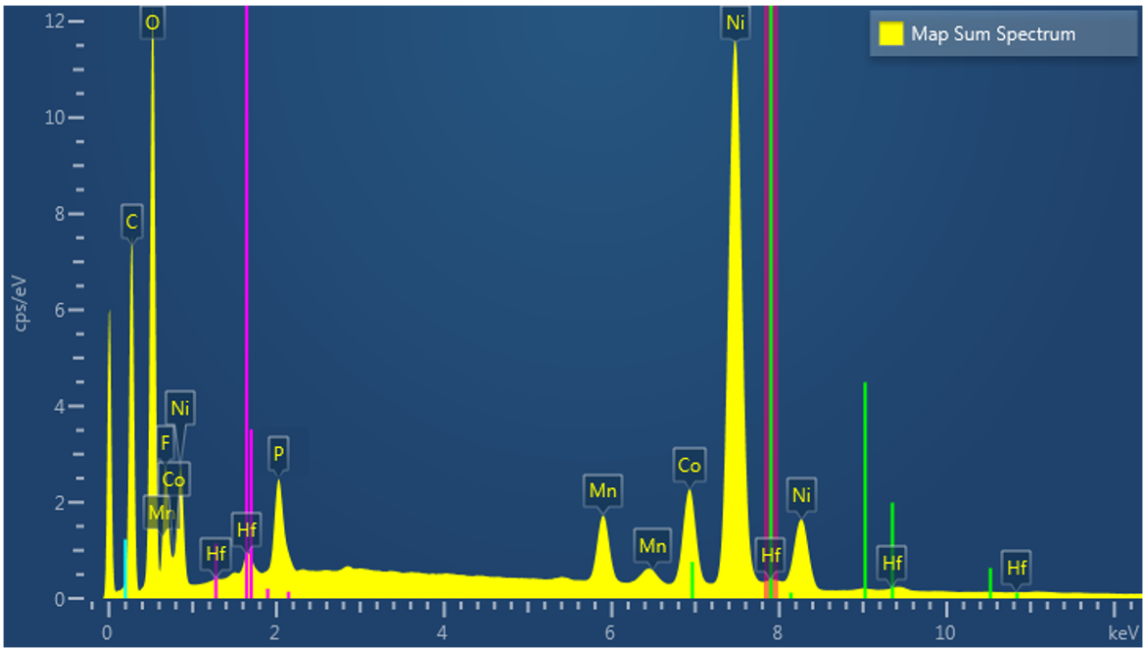


Figure 3.13 EDS spectra for HfO_2 coated NMC811 cathode after 200 cycles at 0.5C.

Element	Weight %	σ
C	37.9	0.3
O	34.3	0.2
Ni	13.7	0.1
F	10.3	0.2
Co	2.2	0.0
Mn	1.0	0.0
Hf	0.5	0.0

Table 3.4 Elemental concentration in weight percent and statistical error of C, O, Ni, F, Co, Mn, Hf for HfO_2 coated NMC811 cathode after 200 cycles at 0.5C.

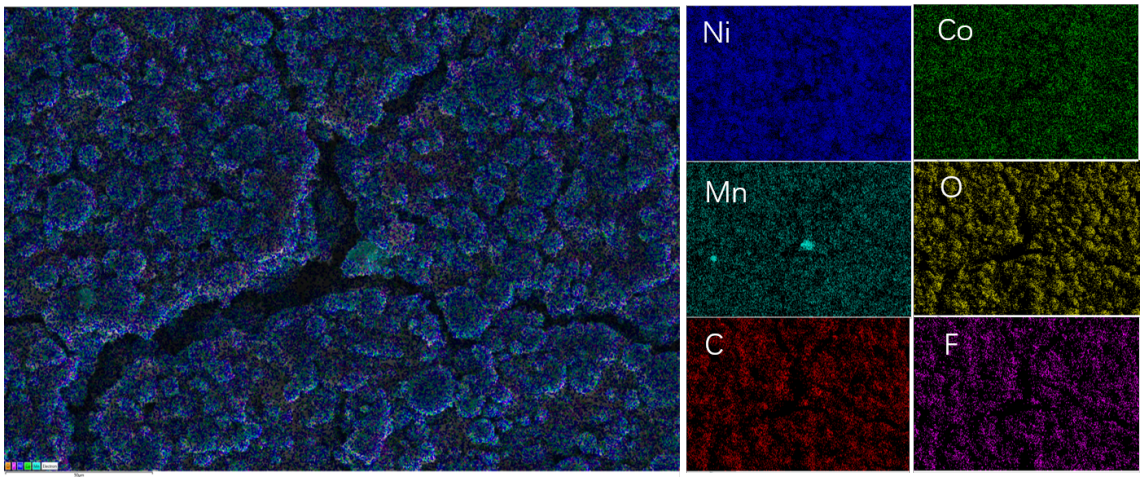


Figure 3.14 Elemental mapping and corresponding elements of Ni, Co, Mn, O, C and F for uncoated NMC811 cathode after 200 cycles at 0.5C.

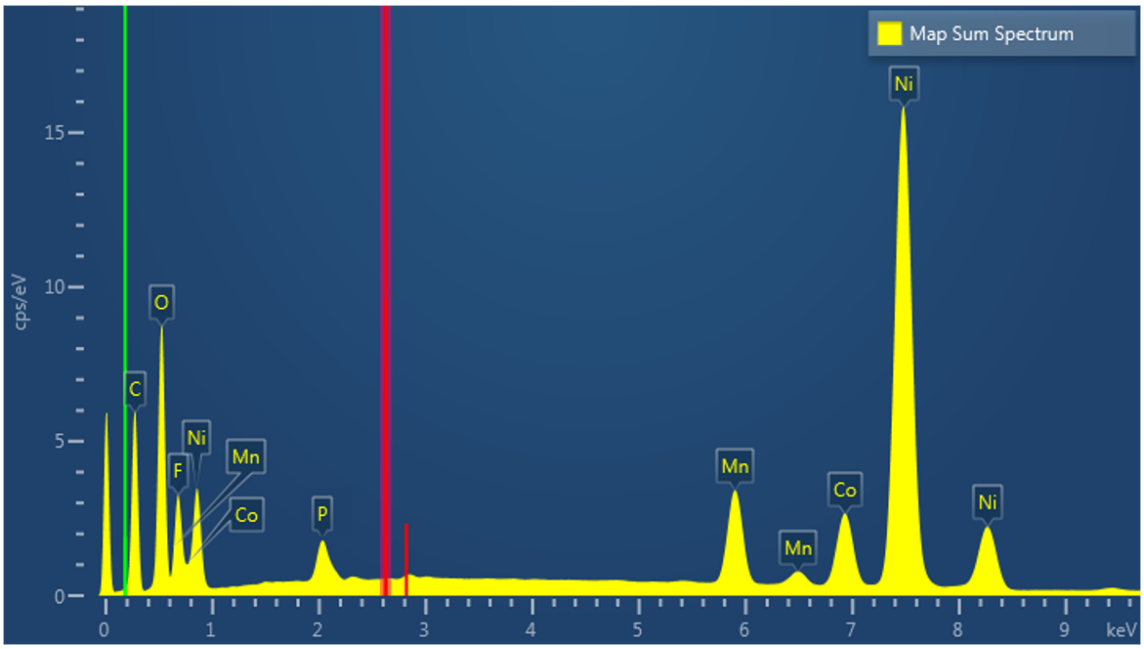


Figure 3.15 EDS spectra for uncoated NMC811 cathode after 200 cycles at 0.5C.

Element	Weight %	σ
C	37.2	0.3
O	26.3	0.2
Ni	19.9	0.1
F	11.5	0.2
Co	2.7	0.0
Mn	2.4	0.0

Table 3.5 Elemental concentration in weight percent and statistical error of C, O, Ni, F, Co, Mn for uncoated NMC811 cathode after 200 cycles at 0.5C.

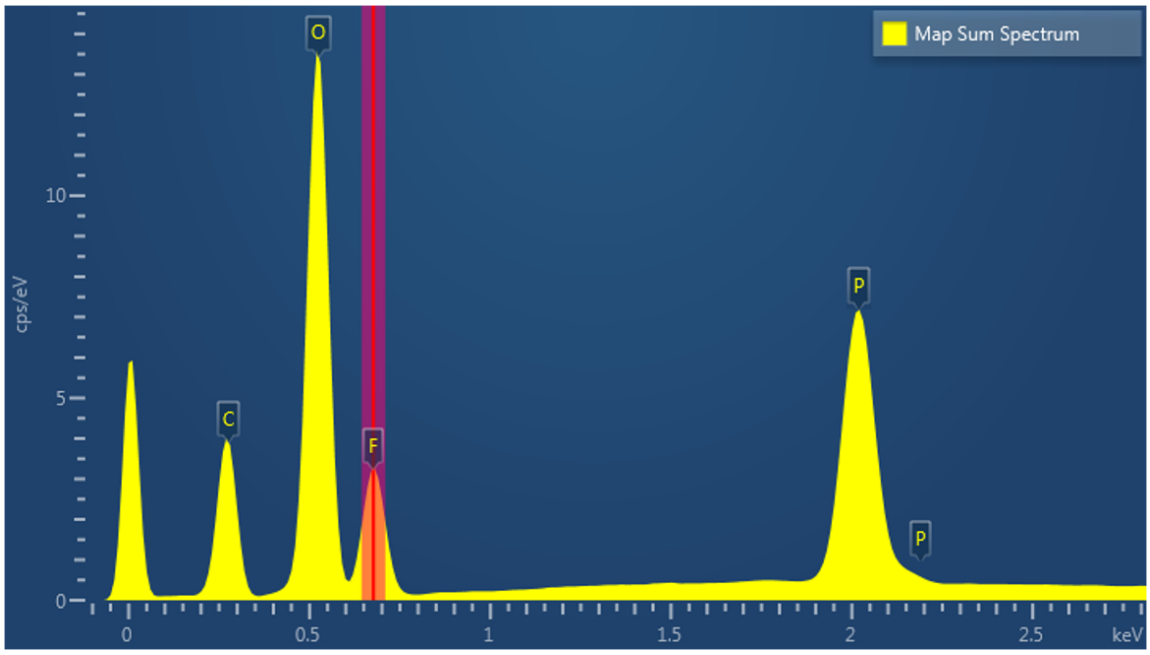


Figure 3.16 EDS spectra for lithium anode of HfO_2 coated NMC811 cathode after 200 cycles at 0.5C.

Element	Weight %	σ
O	47.4	0.3
C	28.5	0.3
F	24.0	0.3

Table 3.6 Elemental concentration in weight percent and statistical error of O, C, F for lithium anode of HfO_2 coated NMC811 cathode after 200 cycles at 0.5C.

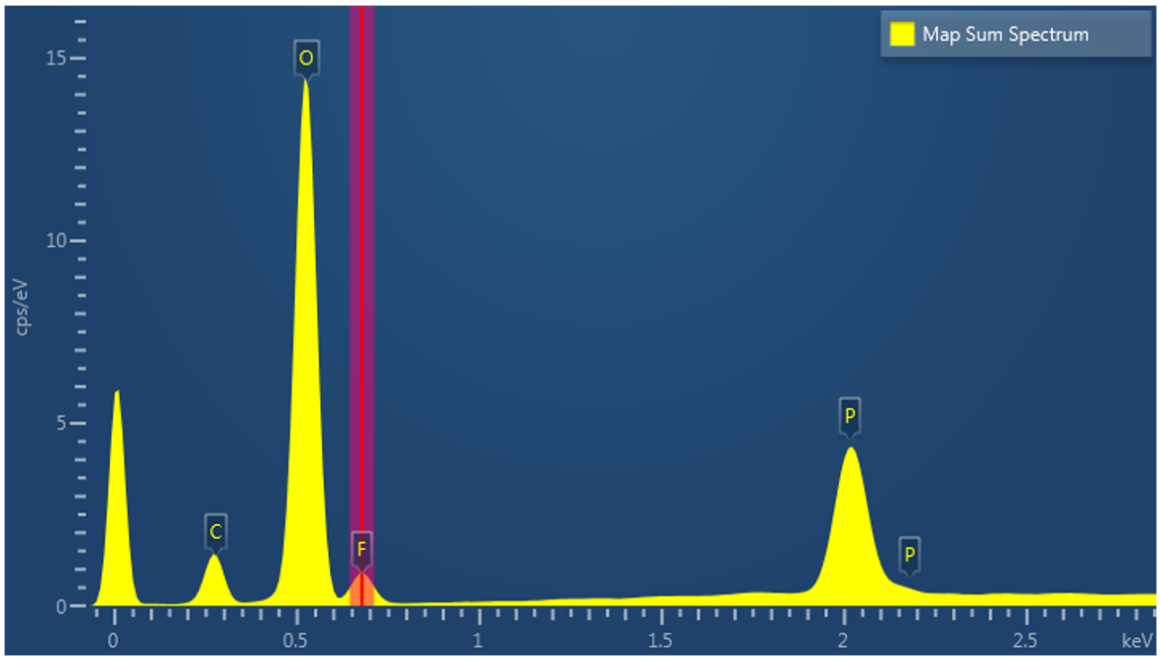


Figure 3.17 EDS spectra for lithium anode of uncoated NMC811 cathode after 200 cycles at 0.5C.

Element	Weight %	σ
O	66.2	0.5
C	18.8	0.4
F	15.0	0.4

Table 3.7 Elemental concentration in weight percent and statistical error of O, C, F for lithium anode of uncoated NMC811 cathode after 200 cycles at 0.5C.

Chapter 4

4 Rational Design of SnO_2 Thin Film Coated Cathode with Function of Entrapping Polysulfides for Performance Enhanced Li-S Batteries

4.1 SnO_2 Magnetron Sputtering Analysis

The synthesis process of Sulfur-Porous carbon cathodes and the coating procedure of SnO_2 film is shown in **Figure 4.1**. For detailed experimental steps, please refer to **Section 2.2.1 and 2.2.2**. When preparing Sulfur-Porous carbon composites, the temperature of 155°C is chosen to ensure the complete melting of sublimed sulfur since its melting point is 112.8°C. The 12-hour duration at 155°C is intended to allow the melted sulfur to fully infiltrate and combine with the porous carbon, enhancing the conductivity of sulfur. Both heating and cooling processes are conducted inside the Argon-filled glovebox to prevent the oxidation of sulfur. The sulfur cathode coated with 5 nm SnO_2 film by magnetron sputtering is characterized for surface morphology and elemental distribution using SEM and EDS. As shown in **Figure 4.2a**, the surface of the cathode exhibits granular sulfur and carbon particles with pores, attributed to the porous structure of carbon and crystalline structure formed by sulfur during slow cooling. **Figure 4.2b-4.2e** display the uniform elemental distribution of S, C, Sn and O on the cathode surface. According to **Figure 4.3**, carbon and sulfur account for 62.9% and 17.9% of the

surface composition in weight, respectively. While based on the TGA results (**Figure 4.2g**), it presents the sulfur content in the Sulfur-Porous carbon composites is around 60% in weight, which differs from the EDS results. This indicates that a significant amount of sulfur is infiltrated into the voids of carbon host during the heating process and cannot be detected by EDS. Besides, the surface of the cathode is not fully flat and has porous structures, which causes the inaccuracy of EDS tests. The weight percentages of Sn and O (**Figure 4.3**) indicate the presence of SnO_2 on the surface of the cathode, but it is relatively in trace amount compared to C and S, therefore accurate quantitative analysis cannot be obtained through EDS measurements. To obtain more information about the composition of uncoated and SnO_2 coated cathode, Raman spectroscopy was performed, and the results are shown in **Figure 4.2f**. Both spectra have two main peaks, they are assigned to D band (1345 cm^{-1}) and G band (1580 cm^{-1}). The ID/IG values of uncoated and 5 nm coated sample samples are 1.03 and 0.94, respectively, which indicates that the coated electrode has higher degree of graphitization and smaller sp2 carbon domain size by depositing SnO_2 on the surface[134-136]. Owing to the influence of the trace amount of SnO_2 and porous structure of carbon, the characteristic peak of SnO_2 is not prominent. Due to the magnification limitation of SEM, detailed internal structures of the cathode cannot be observed. Additionally, since the thickness of the coated SnO_2 film is in the range of a few to several tens of nanometers, quantitative elemental analysis by EDS is not accurate. Therefore, to explore the internal structure details of cathode particles and validate the thickness of the coated film, a combination of STEM and EDS techniques was employed. As shown in **Figure 4.4a** and **4.4b**, the internal structure of the electrode

has a highly porous arrangement, which provides channels for electrolyte penetration and ensures good contact between the electrolyte and cathode materials. **Figure 4.4c** and **Figure 4.4e-g** present elemental mapping of high-angle annular dark field image of cathode particles shown in **Figure 4.4d** and reveal a 5 nm layer of SnO_2 thin film coating on the surface. This confirms the precise deposition rate achieved through the magnetron sputtering parameters used in this study and shows the excellent integration between deposited SnO_2 and porous particles of cathode materials.

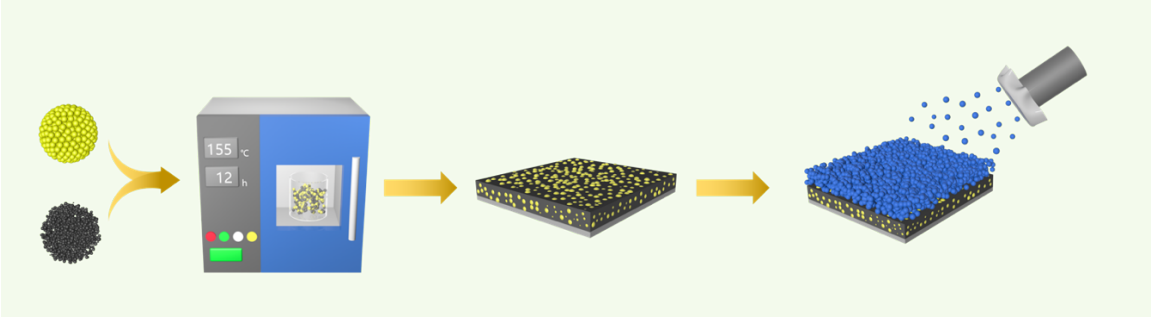


Figure 4.1 Synthesis process of Sulfur/Porous carbon cathodes and SnO_2 thin film coating by magnetron sputtering.

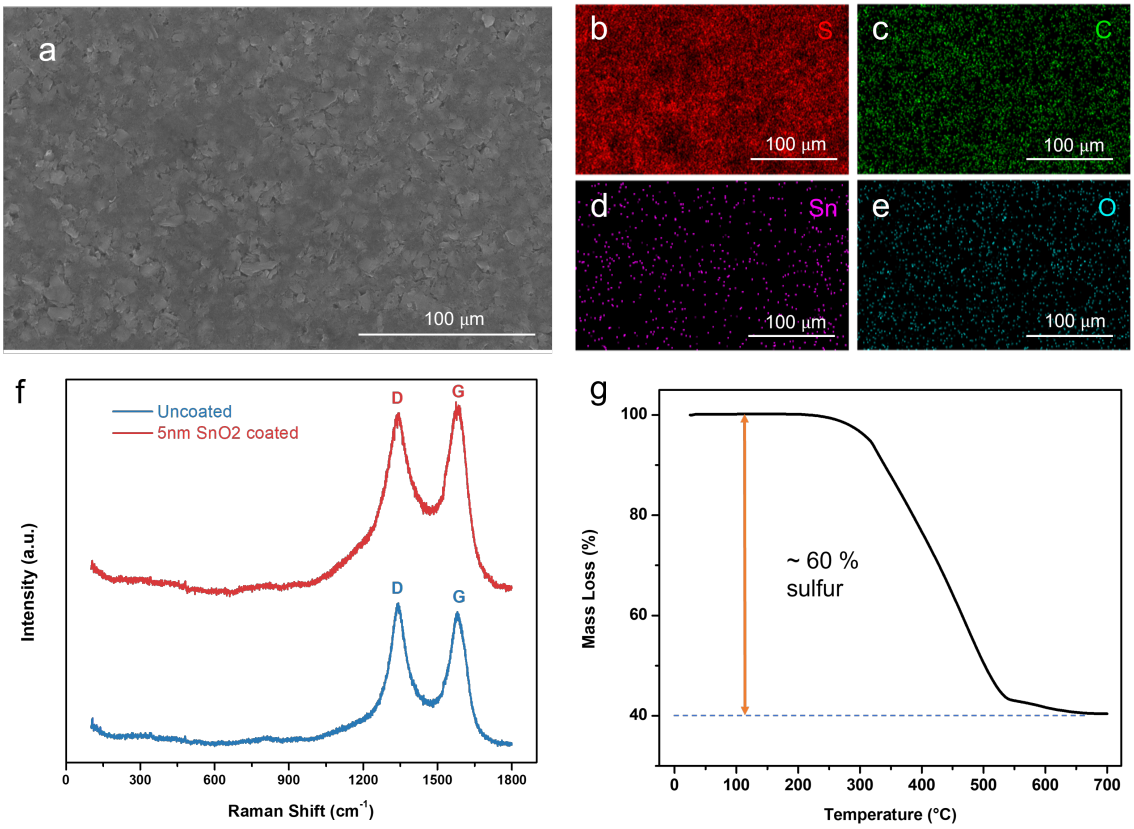


Figure 4.2 (a) Surface morphology of 5 nm SnO_2 coated Sulfur/Porous carbon cathode; (b, c, d, e) Elemental mapping of S, C, Sn and O; (f) Raman spectrum of 5 nm SnO_2 coated Sulfur/Porous carbon cathode; (g) TGA curve of Sulfur and Porous carbon composites.

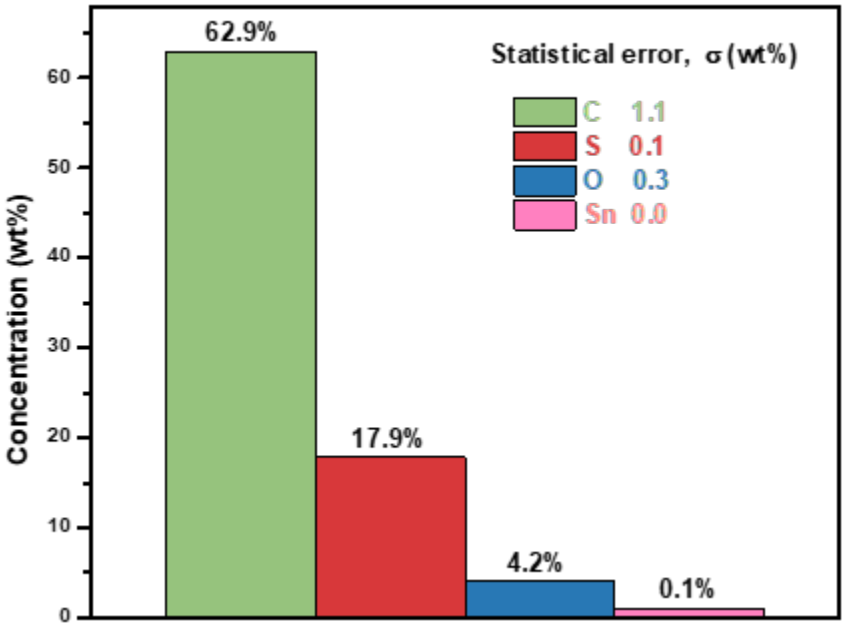


Figure 4.3 Elemental concentration in weight percent and statistical error of C, S, O and Sn.

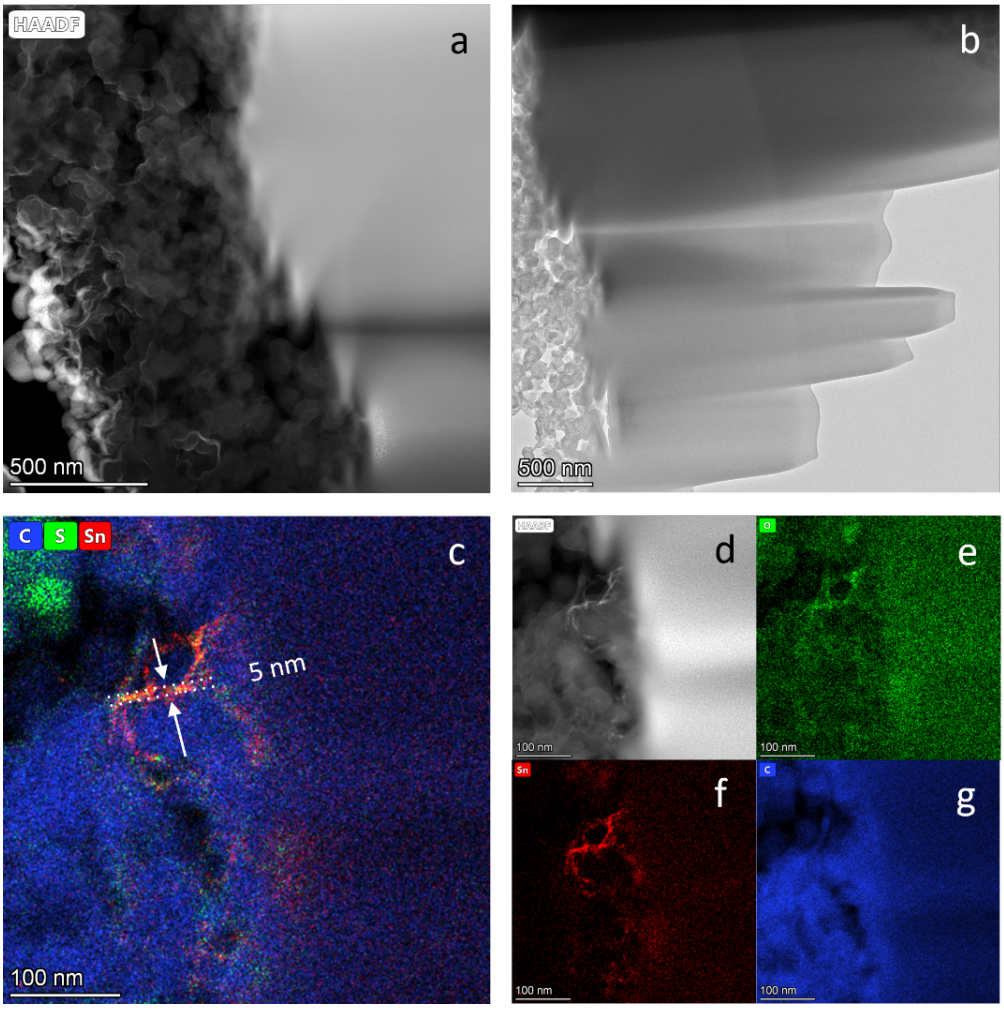


Figure 4.4 (a) High-angle annular dark field (HAADF) and (b) bright field STEM images of SnO_2 coated cathode in low magnification; (c) Elemental mapping of C, S, Sn for (d) HAADF image of SnO_2 coated cathode in high magnification; (e, f, g) Elemental mapping of O, Sn and C for (d) respectively.

4.2 Cycling and Electrochemical Results

The cycle performance results of uncoated and SnO_2 coated Li-S batteries are shown in **Figure 4.5a** (0.1C) and **Figure 4.5b** (0.5C), the batteries were subjected to 3 condition cycles (1/20C) before cycling. The capacity retention of uncoated, 2 nm, 5 nm and 10 nm SnO_2 coated Li-S batteries after 100 cycles at 0.1C are 60.39%, 68.32%,

84.32% and 70.82%, respectively, the Coulombic Efficiencies (CEs) are 96.26%, 97.54%, 99.72% and 98.86%, respectively. Compared with the uncoated Li-S battery curve, the capacity decline of the 2 nm SnO_2 coated curve is slower in the first 20 cycles, the capacities of the 5 nm and 10 nm coated curves both increase at the beginning, and the 5 nm coated curve rises most obviously. This may be because the SnO_2 thin film coating on the surface of the cathode slows the electrolyte diffusion into the cathode and the formation of a stable electrode/electrolyte layer, requiring more time for electrochemical activation than uncoated battery. It can be seen that the 5 nm coated battery has the best cycle performance, its battery capacity decay rate is significantly slower than other batteries, and it has the highest specific capacity and CE. The cycle performance of the 10 nm coated battery is worse than the 5 nm coated battery, which may be because the coating is so thick that weakens the conductivity of the cathode material, and in turn, affects the participation of the active material in the electrochemical reaction. After 100 cycles at a current rate of 0.5C, the specific capacities of uncoated and the 5nm coated batteries are 235.09 and 604.93 mAh/g, CEs are 97.65% and 99.20%, respectively. The capacity of the uncoated battery keeps decreasing, but the capacity of the 5 nm coated battery is increasing in the first 70 cycles, which is consistent with their performance at the 0.1C cycle rate, but due to the increased current rate, the coated battery needs more time to complete the electrochemical activation process. The difference in cycle performance between the 5 nm coated and uncoated batteries is more pronounced at a cycle rate of 0.5C than at a rate of 0.1C. To further explore the rate performance of the batteries, the cycle results at 0.1, 0.2, 0.5 and 1C current rates are

shown in **Figure 4.5c**. As the current rate increases, the difference of specific capacity between the coated and uncoated battery gradually increases. At the 10^{th} cycle of 1C charge/discharge rate, the specific capacity of the uncoated battery is 115.33 mAh/g, that of the 5 nm SnO_2 coated battery is 390.38 mAh/g, which is 3.4 times higher than the uncoated battery. This means that the SnO_2 coating has a more obvious effect on improving battery capacity and stability at high charge/discharge rates. After the current rate drops from 1C to 0.1C, the specific capacity of the coated battery at cycle 70 is 674.74 mAh/g, which is 94.22% of that of cycle 1 (716.12 mAh/g). The specific capacity of the uncoated battery at the 70^{th} cycle is 76.24% of that of the first cycle, which drops 18.1% than the 5 nm coated battery, and its CE after 70 cycles is 2% lower than that of the coated battery. This further proves the good capacity retention performance and high efficiency provided by the SnO_2 thin film coating.

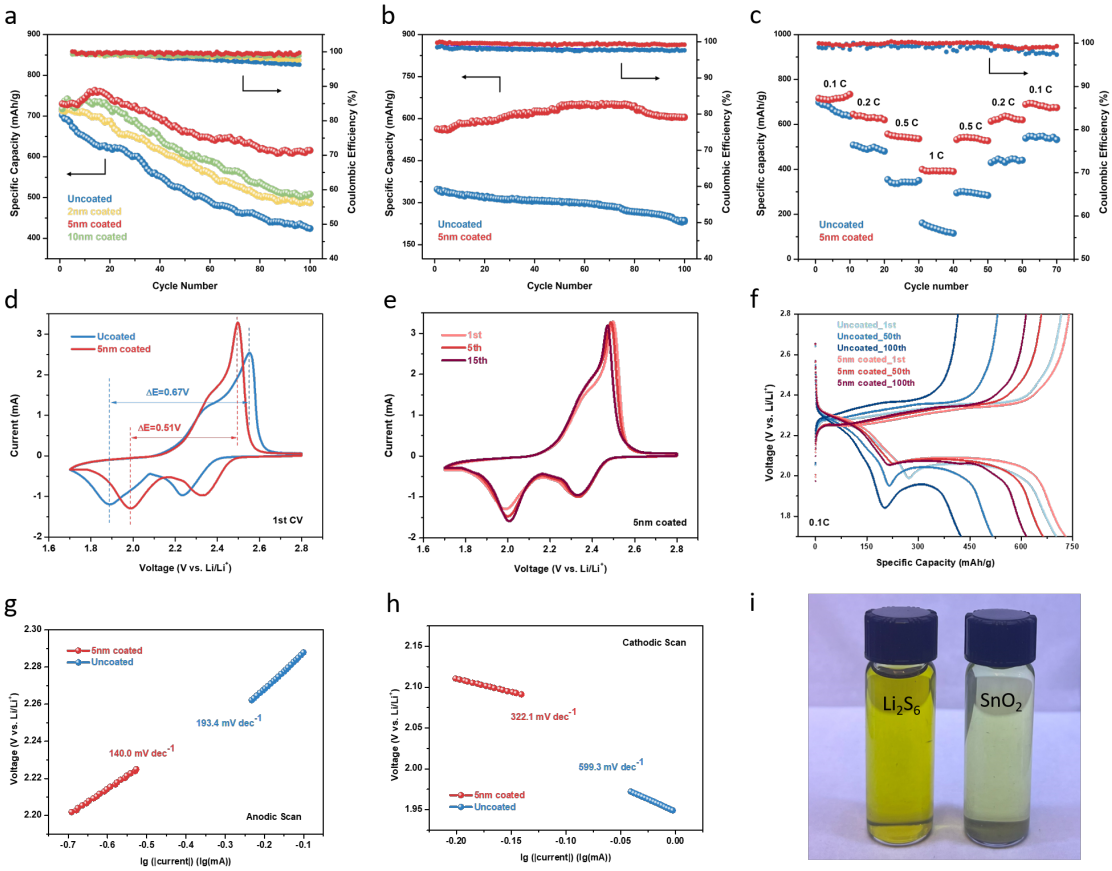


Figure 4.5 (a) Cycle performance of uncoated, 2 nm, 5 nm and 10 nm SnO_2 coated Li-S cells at 0.1C over 100 cycles; (b) Cycle performance of uncoated and 5 nm SnO_2 coated Li-S cells at 0.5C over 100 cycles; (c) Rate performance of uncoated and 5 nm SnO_2 coated Li-S cells; (d) CV curves of uncoated and 5 nm SnO_2 coated Li-S cells after condition cycles; (e) CV curves of 5 nm SnO_2 coated Li-S cells after 1st, 5th and 15th cycles at 0.5C; (f) Voltage profiles of uncoated and 5 nm SnO_2 coated Li-S cells after 1st, 50th and 100th cycles at 0.1C; Tafel plots derived from the (g) anodic scan and (h) cathodic scan of CV curves; (i) digital photos of 2 mM Li_2S_6 solution and SnO_2 added 2 mM Li_2S_6 solution after 7 h of static adsorption.

In order to explore the oxidation/reduction behavior and polarization of the batteries, the CV curves of batteries are measured after 1, 5, and 15 cycles at a cycling rate of 0.5C. As shown in **Figure 4.5d**, for the uncoated battery, there are two anodic peaks during the first charging process, a shoulder peak located at 2.30V and a strong

broad peak at 2.55V, which correspond to the oxidation of short-chain LiPSs to long-chain LiPSs and the further oxidation of long-chain LiPSs to elemental sulfur, respectively[137]. For cathodic scans, there are two strong peaks at 2.22V and 1.88V, representing the reduction of elemental sulfur to long-chain LiPSs and the further reduction of long-chain LiPSs to short-chain LiPSs[138,139]. The battery coated with 5 nm SnO_2 film exhibits CV curves with the same shape as the uncoated battery. However, the voltage difference between oxidation/reduction peaks of uncoated and coated cells are 0.67V and 0.51V. It shows that the positions of the coated cell's anodic peaks (2.30V and 2.50V) and cathodic peaks (2.32V and 1.99V) are closer to each other, and the current of the peaks are larger, indicating reduced polarization in the coated battery. **Figure 4.5e** shows the CV curves of the coated battery after cycling for 1, 5, and 15 cycles, where it can be observed that the positions of the anodic/cathodic peaks and the current of peaks are almost unchanged, indicating excellent electrochemical stability and reversibility of the coated battery[140]. These results from the CV testing are further confirmed by the voltage profile curves of the battery with different cathodes, as shown in **Figure 4.5f**, obtained after cycling once, 50 times, and 100 times at a discharge/charge rate of 0.1C. In addition, the Tafel curves (**Figure 4.5g-h**) are obtained by calculating the oxidation peak (anodic scan at 2.4 V) and reduction peak (cathodic scan at 2.0 V) data in **Figure 4.5d**. For both oxidation and reduction processes, the slopes of the coated cell (140.0 and 322.1 mV/dec) are significantly smaller than the slopes of the uncoated cell (193.4 and 599.3 mV/dec). This further indicates that the SnO_2 coating facilitates the rapid conversion between LiPSs and Li_2S[141-143]. The electrochemical reactions during the discharge

process of Li-S batteries occur in multiple steps. At the short plateau around 2.3V, solid elemental sulfur is reduced to liquid long-chain LiPSs, as shown in **Equation 4.1**.

Equation 4.1

$$S_8\ (s)\ \rightarrow\ S_8\ (l)\ + 4e^-\ \rightarrow\ 2S_4^{2-}$$

As the discharge process continues, liquid long-chain LiPSs are further reduced to solid short-chain LiPSs at the long plateau around 2.1V, as indicated by reaction **Equation 4.2** and **4.3**. These reactions contribute the most to the overall capacity.

Equation 4.2

$$S_4^{2-}\ +\ 8Li^+ + 6e^-\ \rightarrow\ 4Li_2S\ (s)$$

Equation 4.3

$$S_4^{2-}\ +\ 4Li^+ + 2e^-\ \rightarrow\ 2Li_2S_2\ (s)$$

After the long plateau in the discharge curve of the voltage profile, there is a rapid voltage drop, which corresponds to the reduction of Li_2S_2 to Li_2S, as shown in reaction **Equation 4.4**. Due to the solid-state nature of this reaction, it is slower and more challenging than reaction 4.2 and 4.3, resulting in a low contribution to the overall capacity.

Equation 4.4

$$Li_2S_2\ +\ 2Li^+ +\ 2e^-\ \rightarrow\ 2Li_2S\ (s)$$

For the charging curve of the voltage profile, a long and flat plateau appears around 2.3V. During this process, short-chain LiPSs are oxidized to long-chain LiPSs, and then further oxidized to elemental sulfur, in reverse to reaction **Equations 4.1-4.4**. The voltage difference ΔE between the charging plateau and the second discharge plateau

represents the polarization potential of the battery. The uncoated battery exhibits ΔE of 0.30V and 0.42V in the first and 100th cycles, respectively, showing an increase of 0.12V. The coated battery exhibits ΔE of 0.22V and 0.27V, showing a smaller increase of only 0.05V compared to the uncoated battery. This indicates that the coated battery has higher electrochemical stability. Moreover, after 100 cycles, the ΔE of the coated battery is 0.15V smaller than that of the uncoated battery, indicating reduced polarization and a more stable electrode/electrolyte interface. Another noticeable difference in the voltage profile between the two batteries with different cathodes is the presence of a significant dip in the uncoated battery before reaching the long plateau at 2.3V. This dip increases gradually with cycling for uncoated batteries, while the coated battery does not exhibit such a dip. The formation of this dip is caused by concentration polarization. With the increase in the concentration of S_4^{2-}, the electrolyte becomes more and more viscous, resulting in a slower ion diffusion rate. Additionally, S_8 has a low solubility in the electrolyte, leading to a consumption rate of liquid S_8 higher than its diffusion rate, which causes the potential of electrode surface deviating from equilibrium[141]. This may be due to the severe shuttle effect and side reactions between LiPSs and the lithium metal in the uncoated battery, leading to dendrite growth and SEI layer degradation. The growing surface area of lithium anode caused by the dendrites depletes the electrolyte and increases viscosity, which could cause significant concentration polarization, and reduce the battery's lifetime and cycling capacity significantly[142]. Apparently, the coated battery experiences less shuttle effect and concentration polarization, leading to a more stable SEI layer and better cycle and capacity performance. As mentioned earlier, different

regions of the discharge voltage profile represent different steps of electrochemical reactions. **Table 4.1** summarizes the contribution from different reaction step to overall capacity. For the uncoated battery, after 100 cycles, the capacity contribution of the reaction converting long-chain LiPSs to short-chain LiPSs decreases from 37% to 34%, accounting for approximately 1/3 of the total capacity contribution. This may be due to the dissolved long-chain LiPSs shuttling to the vicinity of the anode and reacting with the lithium metal, resulting in the loss of capacity contribution from this portion of active material. In contrast, for the coated battery, this reaction accounts for 44% of the total capacity contribution after 100 cycles, which is 10% higher than the uncoated battery. This further confirms that the coating layer can significantly mitigate the shuttle effect in the Li-S battery and reduce side reactions on the lithium metal surface. The strong ability to inhibit the shuttle effect of coated samples depends on the strong adsorption capability of SnO_2 on polysulfides. The adsorption effect of SnO_2 can be confirmed by the static adsorption test. After 7 hours, the 2 mM Li_2S_6 solution with SnO_2 added is obviously lighter in color than the solution without addition (**Figure 4.5i**).

	Uncoated (Cycle 1)	Uncoated (Cycle 50)	Uncoated (Cycle 100)	5 nm SnO_2 coated (Cycle 1)	5 nm SnO_2 coated (Cycle 50)	5 nm SnO_2 coated (Cycle 100)
$S_8 \rightarrow S_4^{2-}$	39%	41%	47%	33%	35%	34%
$S_4^{2-} \rightarrow Li_2S + Li_2S_2$	37%	35%	34%	47%	44%	44%
$Li_2S_2 \rightarrow Li_2S$	24%	24%	17%	20%	21%	22%

Table 4.1 Capacity contributions from different electrochemical reaction steps for uncoated and 5 nm SnO_2 coated Li-S batteries.

4.3 DFT Calculation Results

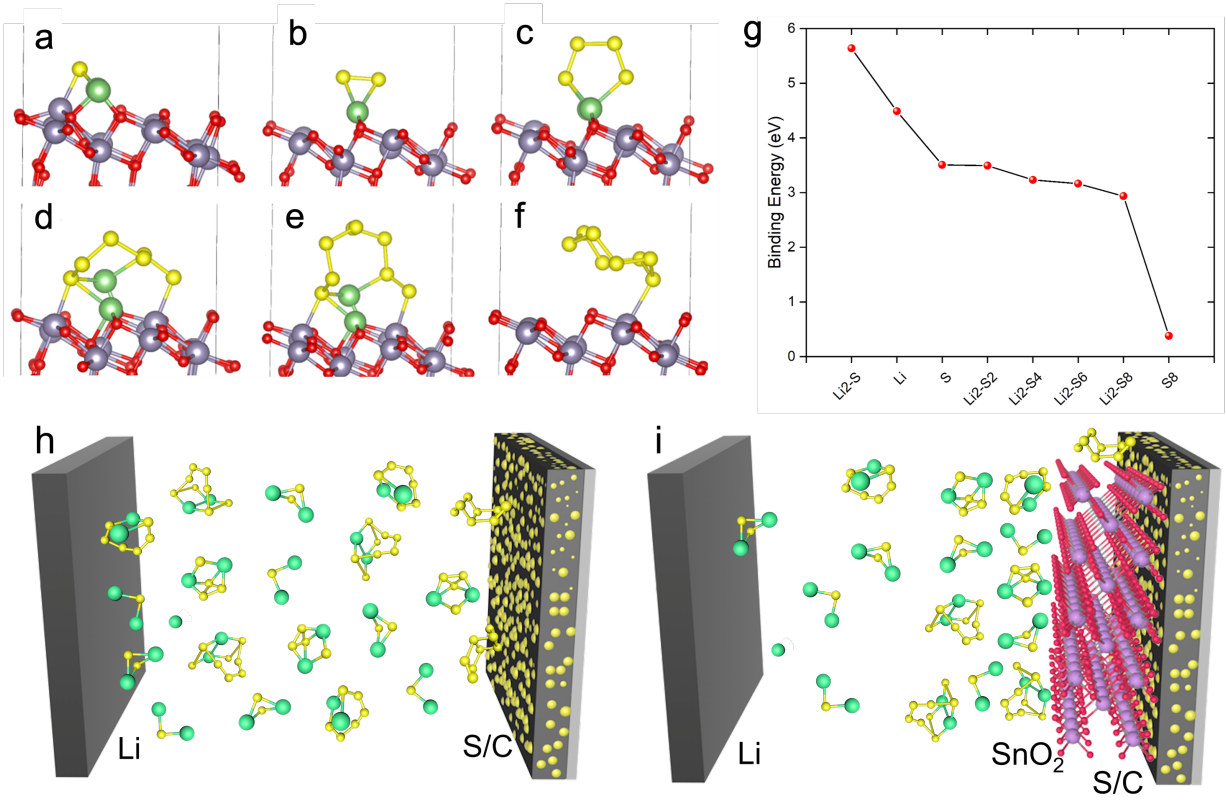


Figure 4.6 Optimized structures for (a) Li_2S, (b) Li_2S_2, (c) Li_2S_4, (d) Li_2S_6, (e) Li_2S_8, and (f) S_8 on the SnO_2 surface. Yellow, green, red, and blue colors indicate S, Li, O and Sn atoms, respectively; (g) Binding energies of the LiPs, Li, S, and S_8 on the SnO_2 surface; Schematic diagram of polysulfides migration in (h) uncoated Li-S cell and (i) SnO_2 coated Li-S cell.

DFT was carried out to understand the interactions between Li_2S_n (n = 1, 2, 4, 6, or 8) species, Li, S, S_8 and SnO_2 surface. The optimized geometries with the lowest total energy of Li_2S_n and S_8 are predicted in our previous work[143] which is compatible with the literature[144,145]. The optimized geometries for Li_2S_n and S_8 on the SnO_2 surface are indicated in **Figure 4.6a–f**. A plot of the binding energy (E_b) for each corresponding

interaction is given in **Figure 4.6g**. After optimization, the Li atom is placed between two O atoms of SnO_2 and the distance between Li and O atoms and angle between the bonds are found to be 1.832 Å and 122.11°, respectively (**Figure 4.7a**). On the other hand, the S atom is placed between Sn and O atoms with a bond length of 2.617 Å (S-Sn) and 1.605 Å (S-O), respectively, with an angle of 103.82° (**Figure 4.7b**). In the S_8 molecule, one of the S atoms forms a bond with Sn atom with a bond length of 2.81 Å (**Figure 4.6f**).

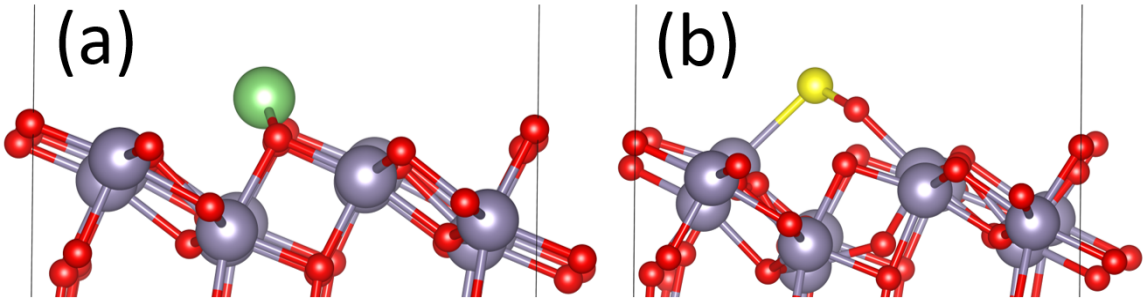


Figure 4.7 The optimized structures of (a) Li and (b) S atoms on the SnO_2 surface.

The interaction between Li_2-S and SnO_2 exhibits the highest E_b of 5.63 eV among all the studied species. This signifies a strong interaction between Li_2-S and the SnO_2 surface, suggesting a favorable adsorption of Li_2-S on SnO_2. Li on SnO_2 also demonstrates a relatively high E_b of 4.48 eV, indicating a favorable adsorption tendency of Li atoms on the SnO_2 surface. The interaction between S and SnO_2 shows a moderate E_b of 3.50 eV, suggesting a favorable interaction despite being lower than the E_b of Li_2-S and Li. Li_2-S_2, Li_2-S_4, Li_2-S_6, and Li_2-S_8 on SnO_2 exhibit E_b ranging from 3.23 eV to 2.93 eV. These values suggest a gradual decrease in E_b as the number of S atoms in Li_2-S increases. However, these species still display relatively high E_b, indicating favorable adsorption on the SnO_2 surface. The interaction between S_8 and SnO_2 has the lowest E_b

of 0.38 eV among all the studied species, suggesting a weaker interaction compared to other species. The lower E_b implies that S_8 may tend to desorb or be less strongly bound to the SnO_2 surface. In summary, the E_b of Li_2S on the SnO_2 surface (5.63 eV) is higher than that of other Li_2Sn. The E_b of Li on the SnO_2 surface (4.48 eV) is also higher than that of S (3.50 eV). These results indicate stronger adsorption tendencies for Li_2-S and Li on SnO_2, while S_8 exhibits a weaker interaction. Comparing with graphene (<1 eV) reported previously[146,147], much larger E_b of Li_2S_n, Li, and S on the SnO_2 were between 5.63 and 2.93 eV indicate the efficacy of SnO_2 in trapping Li_2S_n. Also, S containing species for ZnO coated electrodes has relatively higher E_b (up to 5.40 eV) than that of SnO_2 except for Li_2S on the SnO_2 surface (5.63 eV). It is important to note that too strong binding can weaken the strong Li-S bond and thus induce the decomposition of the Li_2S_n species. Our calculations show that the adsorption capability of SnO_2 is better than the most used surfaces including TiO_2, ZnO and graphene. Moreover, the effectively highlights the differences in performance between the materials investigated in this work and the previously reported studies were given in **Table 4.2**. Comparing the E_b of SnO_2 and commonly used surface materials with LiPSs in **Table 4.2**, we can make the following comments.

	Li_2-S	Li	S	Li_2-S_2	Li_2-S_4	Li_2-S_6	Li_2-S_8	S_8
SnO_2	5.63	4.48	3.50	3.49	3.23	3.16	2.93	0.38
$MoSe_2$[1]	0.79	-	-	0.52	0.28	0.22	0.29	-
C_3N_4[1]	1.08	-	-	1.03	0.88	0.80	0.78	-
TiN [2]	-	-	-	-	-	2.03	-	-
h-TiO_2[3]	-	-	-	-	-	7.40	-	-
CuO[4]	-	3.70	-	-	-	5.20	-	-
Fe_3O_4[5]	0.79	-	-	8.70	4.11	2.18	2.21	4.29
Graphene[6]	-	-	-	-	0.47	-	-	-
Graphene@BP[7]	2.46	-	-	1.54	1.07	0.86	0.95	-
ZnO[8]	3.70	-	-	3.91	2.40	1.21	1.79	0.10
TiO_2[9]	4.47	-	-	-	2.78	-	-	-

Table 4.2 The binding energies (in eV) of SnO_2 and polysulfides interactions and comparison with the previous reports.

SnO_2 generally exhibits higher E_b with LiPSs compared to ZnO[148]. This indicates that SnO_2 has a stronger affinity for LiPSs, suggesting a potentially more favorable interaction between SnO_2 and LiPSs in the Li-S battery system. The higher E_b of SnO_2 with Li_2-S, Li, and S suggest that SnO_2 can effectively interact with these key components of the Li-S battery chemistry. This is important as strong interactions can enhance the stability and performance of the battery system. As the number of sulfur atoms in the LiPSs species increases, the E_b gradually decrease for both SnO_2 and ZnO.

This suggests that the interaction between the materials and LiPSs weakens as the LiPSs chain lengthens. On the other hand, SnO_2 shows a E_b of 5.63 eV with Li_2-S, while TiO_2 has a E_b of 4.47 eV with Li_2-S[149]. This indicates that SnO_2 has a stronger affinity for LiPSs. However, TiO_2 demonstrates a higher E_b of 7.40 eV with h-TiO_2 for Li_2-S_6[146], compared to SnO_2. Additionally, TiO_2 exhibits a E_b of 2.78 eV with Li_2-S_4, which is lower than the corresponding value for SnO_2. While a strong interaction between a material like h-TiO_2 and LiPSs, as indicated by a E_b of 7.40 eV, may initially seem desirable, it can have unintended consequences. In a Li-S battery system, the formation and stability of Li_2S species are crucial for overall battery performance. Very strong E_b between the material (such as h-TiO_2) and LiPSs can potentially weaken the strong Li-S bonds within the Li_2S species. This can lead to premature decomposition of Li_2S and undesired side reactions, negatively impacting the battery's capacity, cycling stability, and overall efficiency. On the other hand, the relatively high E_b of SnO_2 with LiPSs compared to other materials[150-155] listed in the **Table 4.2** (such as $MoSe_2$, C_3N_4, CuO, Fe_3O_4, Graphene, and Graphene@BP) indicate that SnO_2 may offer a more favorable surface for LiPSs adsorption and conversion in Li-S batteries.

The strong adsorption capability of the SnO_2 film can play a crucial role in alleviating the shuttle effect and enhancing battery performance. The SnO_2 film, with its high E_b for Li_2-S and Li species, can effectively trap and immobilize these species on its surface. This prevents their dissolution and subsequent migration within the battery system, minimizing the shuttle effect. By immobilizing Li_2-S species, which are responsible for the shuttle effect as they shuttle between the electrodes, the SnO_2 surface

helps to maintain a stable electrochemical environment and reduce capacity loss. Furthermore, the strong adsorption of Li_2-S and Li on the SnO_2 film can promote more reversible electrochemical reactions. When Li_2-S species are adsorbed onto the SnO_2 film, they are more likely to undergo conversion reactions and form insoluble lithium sulfides. This conversion process reduces the solubility of Li_2-S species, preventing their dissolution and loss from the electrode. As a result, the SnO_2 film enhances the overall electrochemical reversibility of the battery system, leading to improved capacity retention and cycling stability. On the other hand, the SnO_2 film's strong adsorption capability for Li_2-S and Li helps maintain a stable and well-defined electrode-electrolyte interface. By adsorbing and immobilizing these species, the SnO_2 film limits their interaction with the electrolyte, reducing side reactions and preserving the structural integrity of the electrode. This stability contributes to the long-term performance and durability of the battery.

The mechanism diagrams of the uncoated and SnO_2 coated batteries as revealed by DFT calculations are shown in **Figure 4.6h** and **4.6i**. The uncoated battery exhibits severe shuttle effect, where many long-chain LiPSs generated during the electrochemical reaction migrate to the surface of the anode and directly react with the lithium metal, resulting in the loss of active material and growth of lithium dendrites. The increased surface area of the anode further exacerbates electrolyte consumption, leading to decreased specific capacity and reduced cycle life of the battery. The battery with an SnO_2 thin film coated cathode, significantly mitigates the shuttle effect by confining most of the LiPSs at the cathode, which creates a more stable SEI layer of the anode. Compared to the uncoated battery, the coated battery exhibits higher specific capacity

and improved cycle life due to the reduced shuttle effect and stabilized electrode/electrolyte interface.

4.4 Electrochemical Impedance Spectroscopy and Galvanostatic Intermittent Titration Technique Results

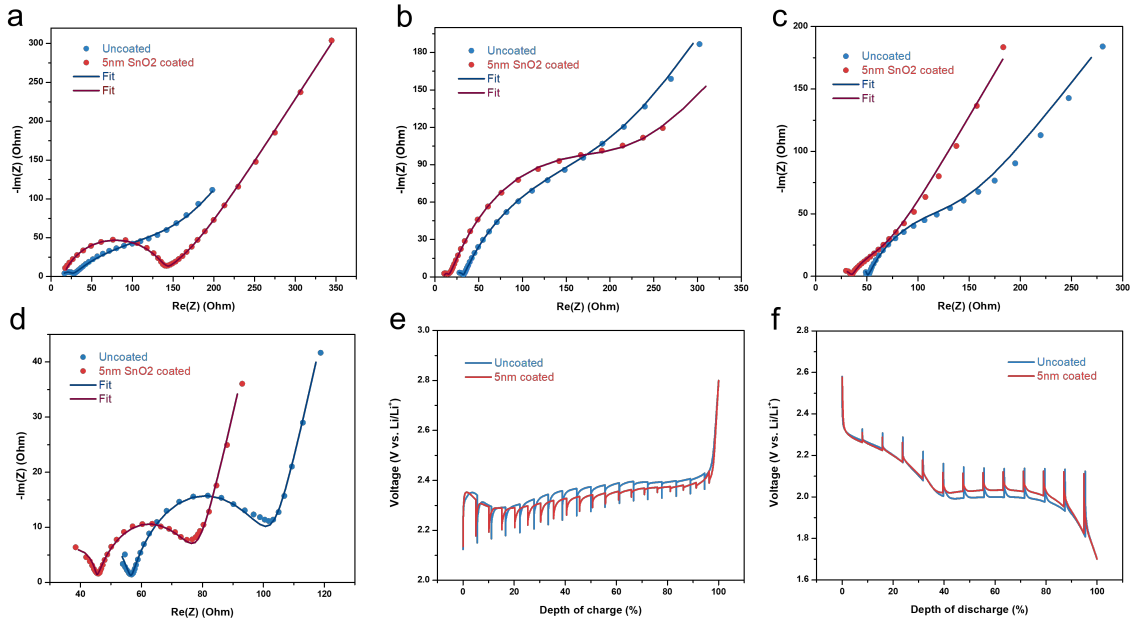


Figure 4.8 EIS plots of uncoated and 5 nm SnO_2 coated Li-S cells (a) before condition cycles, (b) after condition cycles, (c) after 100 cycles at 0.1C, and (d) after 100 cycles at 0.5C; GITT measurements of uncoated and 5 nm SnO_2 coated Li-S cells (e) during charging and (f) discharging.

EIS is employed to further investigate the internal impedance and charge transfer behavior of the batteries during cycling. The EIS results before condition cycles are shown in **Figure 4.8a**. The high-frequency region of the Nyquist plot represents the combined electrolyte resistance (R_e) and charge transfer resistance (R_{ct}), while the

sloping line in the low-frequency region represents the Warburg resistance relating to ion diffusion. The equivalent circuit fitting model is depicted in **Figure 4.9a**[156]. The plot of the coated battery exhibits a large semicircular arc, which is absent in the plot of the uncoated battery, indicating a significantly higher R_{ct} (120.3 Ω) in the coated battery, nearly twice that of the uncoated battery. This is attributed to the insulating nature of the SnO_2 coating layer[133,157]. The equivalent circuit fitting model of the battery after cycling is shown in **Figure 4.9b**. R_{int} is related to the interface contact resistance between the electrodes and soluble long-chain LiPSs. As shown in **Table 4.3**, after condition cycles, the coated battery demonstrates a lower R_{int} compared to the uncoated battery, with a reduction of 3.24 Ω. After cycling 100 times at 0.1C and 0.5C, the reductions are 8.89 Ω and 13.93 Ω, respectively. This indicates that the coated battery has a more stable electrode/electrolyte interface than the uncoated battery, and this difference becomes more pronounced with increasing cycle number and discharge/charge current. The EIS results after condition cycles and after cycling 100 times at a rate of 0.1C are shown in **Figure 4.8b** and **4.8c**, respectively. After 100 cycles, different from an increase of 15.37 Ω of R_{ct} for the uncoated battery, the R_{ct} of the coated battery decreases by 76.14 Ω. This suggests that with cycling, the insulating property of SnO_2 has less influence on charge transfer in the battery. This may be due to the stable interphase formed by active materials, electrolyte, and coating layer during the redox reactions. The sloping line in the low-frequency region of the EIS represents ion diffusion. In **Figure 4.8c**, the slope of the coated battery is much higher than that of the uncoated battery, indicating a smaller Li^+ diffusion impedance after 100 cycles. **Figure 4.8d** shows the Nyquist impedance plots of

the batteries after cycling 100 times at a rate of 0.5C, where the R_e, R_{int}, and R_{ct} of the coated battery are 83.7%, 60%, and 83.3% of those of the uncoated battery, respectively. This is because the SnO_2 coating layer reduces the shuttle effect of long-chain LiPSs in the electrolyte, resulting in less deposition of short-chain LiPSs on the lithium metal surface and consequently showing a smaller R_{int} in the EIS results. Due to the reduced deposition of short-chain LiPSs and dendrites on the lithium anode, electrolyte consumption decreases, leading to a smaller R_e of coated battery. The stable electrode/electrolyte interface in the coated battery facilitates charge and mass transport of ions, resulting in a smaller R_{ct}, higher ion conductivity and electrochemical reversibility. **Figure 4.8e** and **4.8f** depict the charge and discharge profiles obtained from GITT testing. The voltage variations caused by each pulse in the coated battery are smaller than those in the uncoated battery. The maximum voltage difference occurs at the plateau region of the charge curve and the second plateau region of the discharge curve, further confirming the weakening effect of SnO_2 on the shuttle effect and corroborating the previous EIS results.

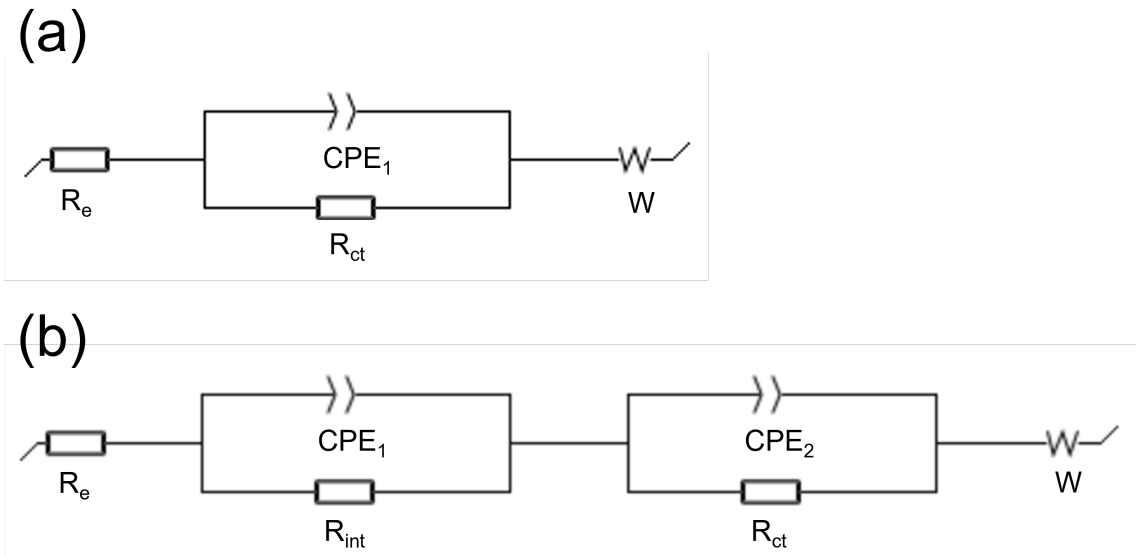


Figure 4.9 Equivalent circuit fitting model for Li-S batteries (a) before cycles and (b) after cycles. R_e is the electrolyte resistance, R_{ct} is the charge-transfer resistance, and R_{int} is interface contact resistance. Q1 and Q2 are the constant phase related to the capacitance. W is Warburg resistance associated with diffusion of Li^{+}[158].

		R_e (Ω)	R_{int} (Ω)	R_{ct} (Ω)
Coated	Before condition	13.33	/	120.3
	After condition	12.98	18.37	102
	After 0.1C	8.612	27.18	25.86
	After 0.5C	14.06	20.9	33.59
Uncoated	Before condition	5.607	/	67.77
	After condition	10.17	21.61	20.08
	After 0.1C	14.6	36.07	35.45
	After 0.5C	16.8	34.83	40.33

Table 4.3 EIS fitting results for uncoated and 5 nm coated Li-S batteries before/after condition cycles, after 100th cycle at 0.1C and after 100th cycle at 0.5C[66].

4.5 Scanning Electron Microscopy and Energy Dispersive X-ray Spectroscopy Results

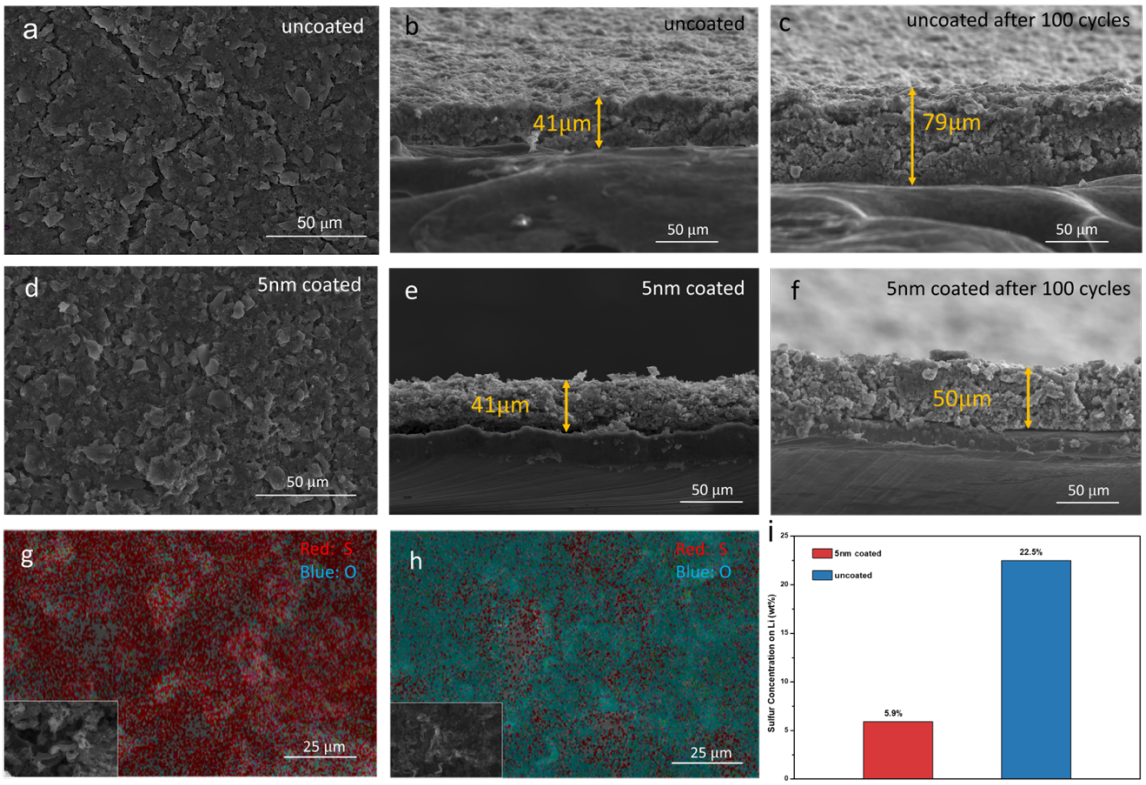


Figure 4.10 (a) Surface morphology, cross sections (b) before condition cycles and (c) after 100 cycles at 0.1C of uncoated cathode; (d) Surface morphology, cross section (e) before condition cycles and (f) after 100 cycles at 0.1C of 5 nm SnO_2 coated cathode; Surface morphologies and elemental mapping of lithium anodes of (g) uncoated Li-S cell and (h) 5 nm SnO_2 coated Li-S cell; (i) Sulfur concentration on lithium anodes.

SEM and EDS are employed to characterize the surface morphology and elemental distribution of the electrodes after cycling. After cycling 100 times at a rate of 0.1C, the batteries were opened in glovebox, and the electrodes were kept undisturbed overnight before testing. It should be noted that the lithium anode needs to be preserved in Argon atmosphere during the transfer process. The surface morphology of the cathodes after cycling is shown in **Figure 4.10a** and **4.10d**. Some cracks are observed on the

surface of the uncoated cathode, while the coated cathode exhibits a smoother surface without noticeable cracks. The formation of cracks is attributed to the increased internal stress caused by the volume changes of the cathode during cycling. As shown in **Figure 4.10b** and **4.10c**, the thickness of the uncoated cathode increases to 193% of its initial thickness after cycling, leading to the generation of internal and surface cracks due to the expansion of the cathode volume. The volume change of the 5 nm SnO_2 coated cathode is shown in **Figure 4.10e** and **4.10f**, where the electrode thickness after cycling becomes 122% of its initial thickness, representing a 71% reduction compared to the uncoated electrode. The reduced volume expansion contributes to the mitigation of crack formation. And the less volume expansion may be due to the coated electrode having a more stable electrode/electrolyte interface, resulting in less electrolyte consumption and fewer side reactions. The SEM and EDS results of the lithium anodes after cycling are shown in **Figure 4.10g** and **4.10h**. The lithium metal paired with the uncoated cathode exhibits more and larger dendrites on the surface compared to the lithium metal paired with the coated cathode. This indicates that the SnO_2 coating layer effectively limits the growth of lithium dendrites and contributes to the formation of a more stable SEI layer. Further EDS results regarding the lithium anode surface are shown in **Figure 4.11-4.14**. The weight percentage of sulfur on the surface of the lithium metal paired with the uncoated cathode is 22.5%, whereas it is only 5.9% on the lithium metal surface paired with the 5 nm SnO_2 coated cathode (**Figure 4.10i**). This indicates that the SnO_2 coating layer significantly weakens the shuttle effect, thereby reducing the deposition of short-chain LiPSs on the anode surface, ensuring effective utilization of the active material and

the formation of a stable SEI layer. The SEM and EDS results further support and validate the results obtained from electrochemical tests and DFT calculations.

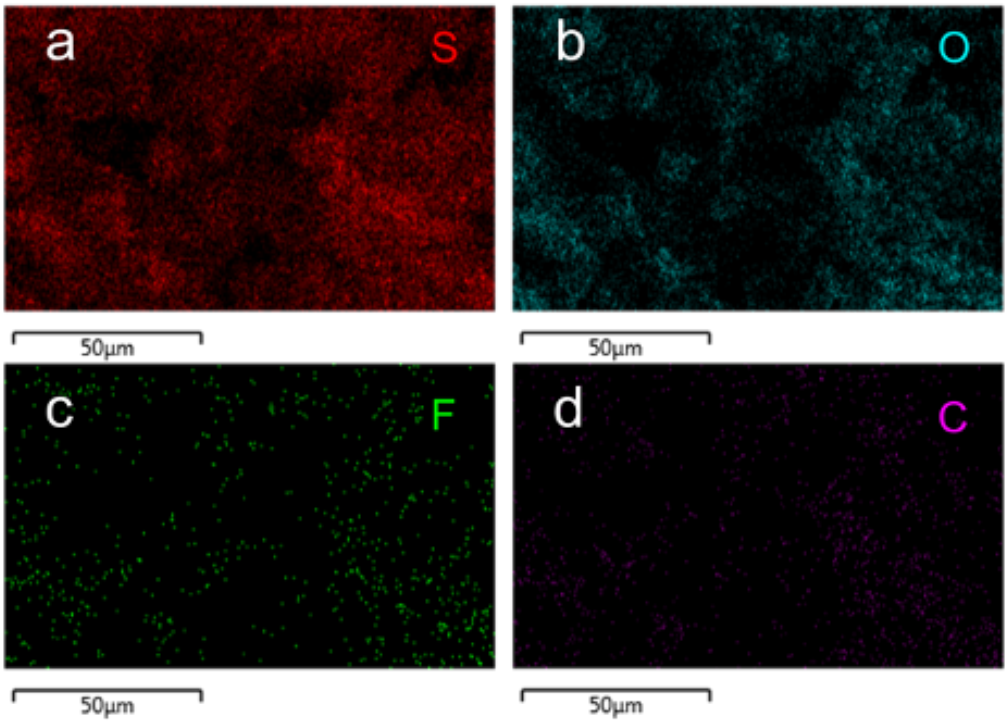


Figure 4.11 EDS mapping of (a) S, (b) O, (c) F and (d) C elements for the lithium anode paired with uncoated cathode.

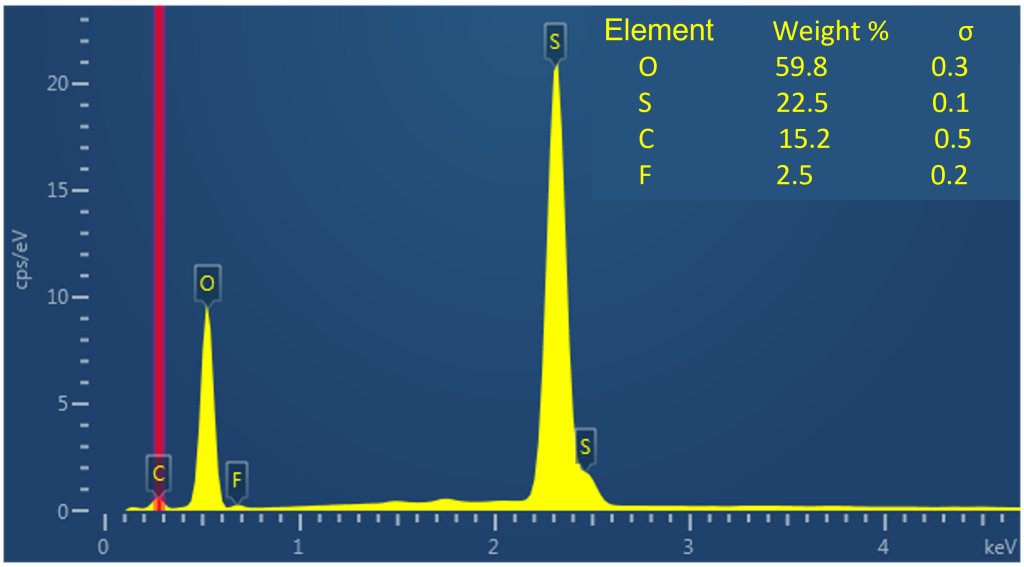


Figure 4.12 EDS spectrum for the lithium anode paired with uncoated cathode. Elemental concentration in weight percent and statistical error of O, S, C and F.

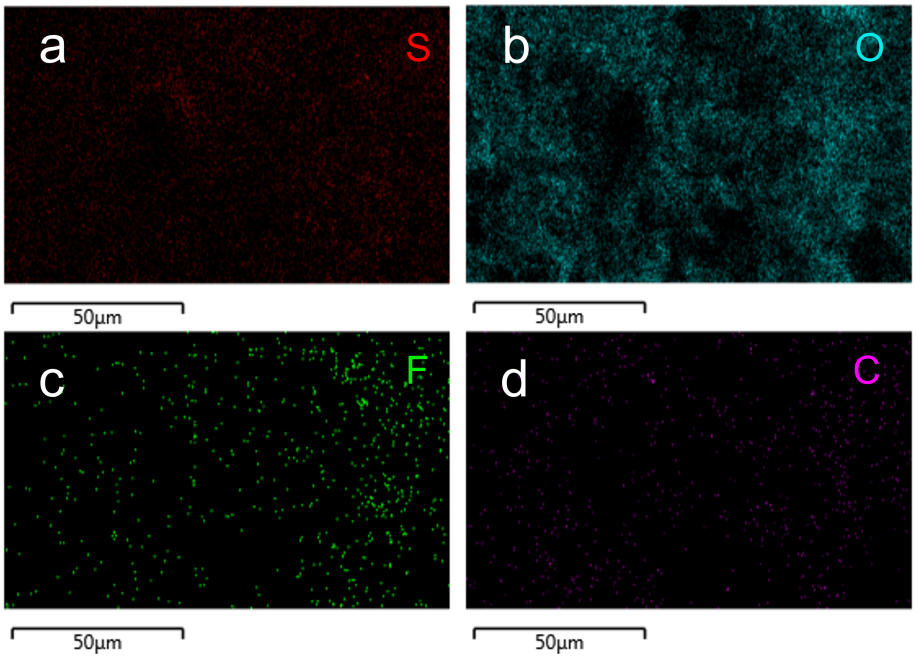


Figure 4.13 EDS mapping of (a) S, (b) O, (c) F and (d) C elements for the lithium anode paired with 5 nm SnO_2 coated cathode.

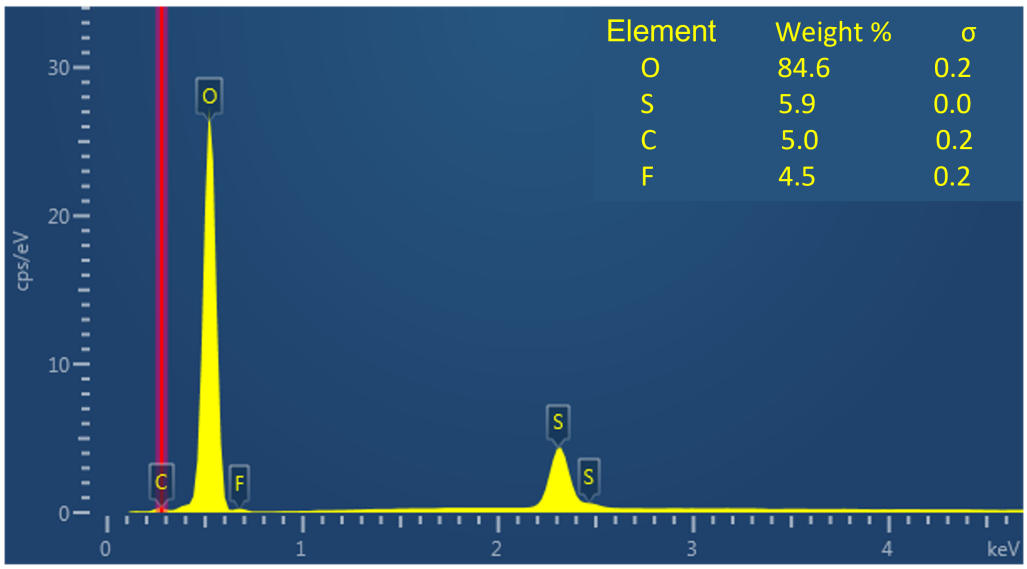


Figure 4.14 EDS spectrum for the lithium anode paired with 5 nm SnO_2 coated cathode. Elemental concentration in weight percent and statistical error of O, S, C and F.

Chapter 5

5 Interfacial Modification of Li_6PS_5Cl-based All-solid-state Li-S Batteries by Al_2O_3 Nano-layer Deposition

5.1 Designed All-solid-state Battery Structure and ALD Deposition

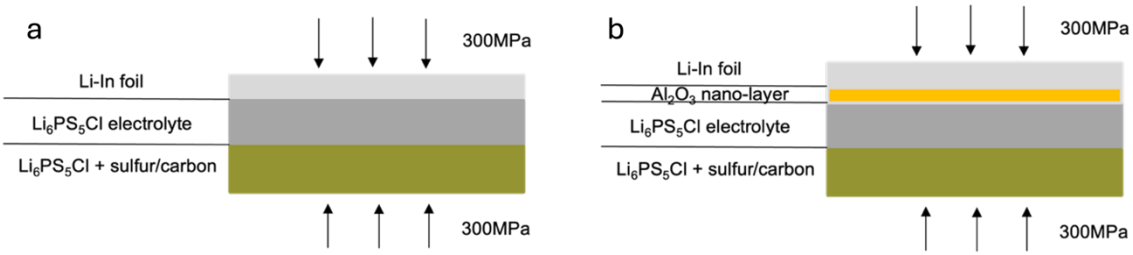
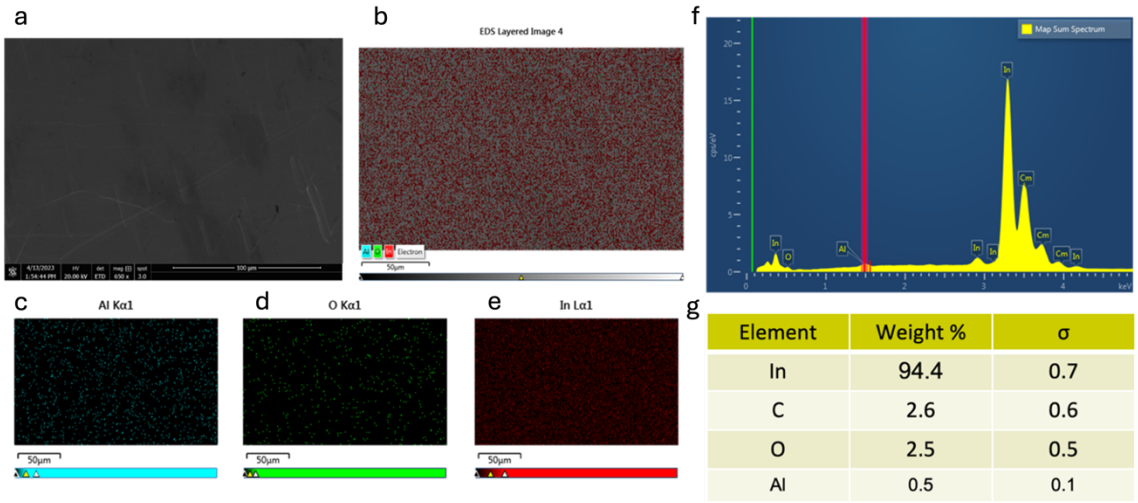


Figure 5.1 Designed Li_6PS_5Cl-based all-solid-state Li-S batteries (a) without or (b) with Al_2O_3 nano-layer deposition.

Figure 5.1 depicts a schematic of our solid-state lithium battery cell design. This design utilizes solid lithium phosphorus sulfide chloride (LiPSCl) electrolytes instead of the conventional liquid electrolyte found in lithium-ion batteries. The Lithium-Indium foil (Li-In) functions as the anode of the battery cell. A thin layer of Al_2O_3 was coated on the surface of the surface of anode by ALD. This layer serves as a protective barrier to prevent dendrite formation and short-circuit. The solid electrolyte separates the anode and cathode. The cathode consists of a composite material of Li_6PS_5Cl and sulfur/carbon composite. A pressure of 300 MPa was applied to compress the powder materials and foil

together. This high pressure is necessary to maintain physical contact between the solid-state layers and enhance cell performance.



Element	Weight %	σ
In	94.4	0.7
C	2.6	0.6
O	2.5	0.5
Al	0.5	0.1

Figure 5.2 (a) SEM result and (b) EDS mapping for Al_2O_3 coated Indium foil with elemental analysis of (c) Al, (d) O and (e) In; (f) EDS spectra and (g) element weight percentage of Al_2O_3 coated Indium foil.

Figure 5.2 shows the SEM and EDS mapping results of Al_2O_3-coated Indium foil. The coated foil is flat and smooth, which indicates that the ALD deposition doesn't change the morphology of the original Indium foil. From the elemental mapping results and EDS spectrum, it is proved that the surface of the foil consists of Indium, carbon, aluminum, and oxygen elements. The presence of oxygen element originated from coated Al_2O_3 and self-oxidation of indium foil exposed to air. **Figure 5.2g** shows the weight percentages and statistical errors of the above-mentioned elements, the weight percentages of Al and O are 0.5% and 2.5%, which shows the Al_2O_3 nano-layer was coated successfully.

5.2 Ion Conductivity of Solid Electrolyte

Figure 5.3a shows the Nyquist plot result of the designed symmetrical cell shown in **Figure 5.3b**. Nyquist plot is a common way to represent EIS data, the plot shows the imaginary part of the impedance on the y-axis and the real part of the impedance on the x-axis. In **Figure 5.3a**, the intersection of the Nyquist plot and the x-axis represents the bulk resistance of the symmetrical cell[133]. The electrodes of the symmetrical battery are both indium metal, and the Li_6PS_5Cl solid electrolyte powders are sandwiched between two identical electrodes[159]. A pressure of 380 MPa is applied to the symmetrical electrodes to compact the powder materials. Here, it is used to calculate the ion conductivity of Li_6PS_5Cl solid electrolyte.

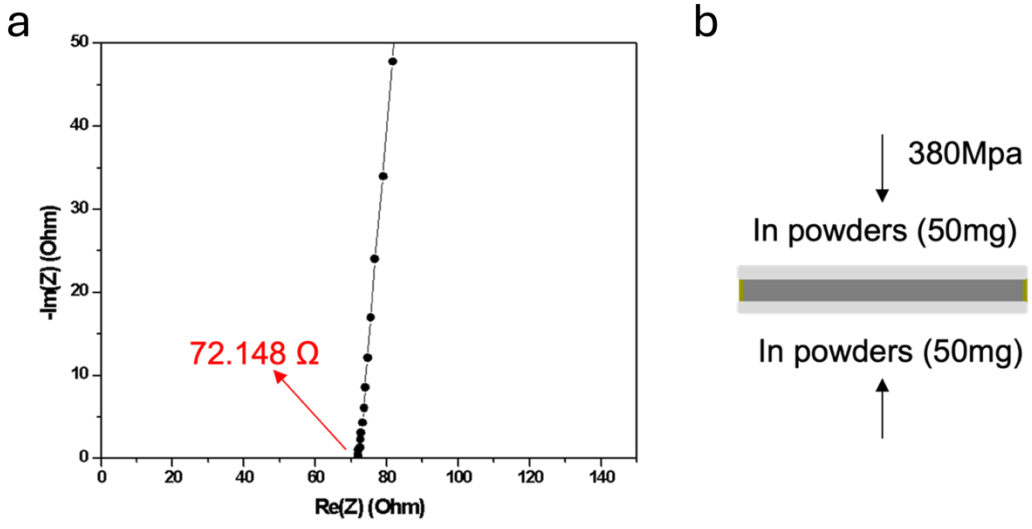


Figure 5.3 (a) EIS result and (b) the structure of designed symmetrical cell to calculate Li ion conductivity.

Here is the equation used for Li ion conductivity calculation:

Equation 5.1

$$Ionic\ conductivity\ \sigma = \frac{d}{R_b \times A}$$

Where d is thickness of the solid electrolyte pellet, R_b is bulk resistance and A is the area of the solid electrolyte pellet.

$$\sigma = \frac{0.14\ cm}{72.148\ \times\ 0.51335\ cm^{-2}} = 3.78\ mS/cm$$

The Li ion conductivity of synthesized electrolyte is 3.78 mS/cm, which is similar to reported literatures[160].

5.3 Electrochemical Results of Symmetrical Cells

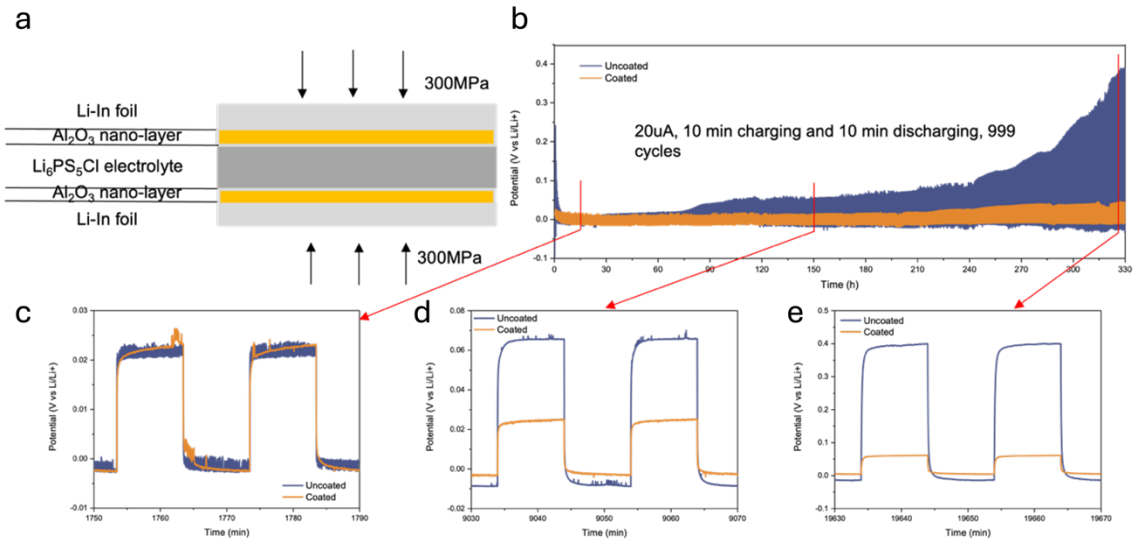


Figure 5.4 (a) Structure of Al_2O_3 coated symmetrical cell; (b) Cycling data of coated and uncoated symmetrical cells; Cycling data after (c) 15h, (d) 150h and (e) 328h of coated and uncoated symmetrical cells.

Figure 5.4 shows the structure and cycling data of the designed symmetrical cell with ALD coating. Constant current 20 μA was used to charge and discharge the coated

and uncoated symmetrical cell per 10 minutes over 999 cycles. In **Figure 5.4b-e**, the y-axis represents the potential of the cell vs. the potential of Li, while the x-axis refers to the total time the experiment was conducted. The uncoated symmetrical cell has a much larger overpotential than the coated cell at the beginning, but it drops fast. After 15h, the potentials of coated and uncoated symmetrical cells are the same. This indicates that the uncoated cell has a large interfacial resistance before cycling and needs time to activate. However, the coated symmetrical cell doesn't need extra time to activate, which indicates the Al_2O_3 coating layer lowers the interfacial resistance of the solid-state cell successfully. After 75h, the overpotential of the uncoated cell increased dramatically and was much larger than the coated cell. This shows the coating layer lowers the overpotential and increases the stability of the solid-state battery successfully. EIS and SEM results can further explain the reason for the different performances.

5.4 EIS and SEM results of Symmetrical Cells

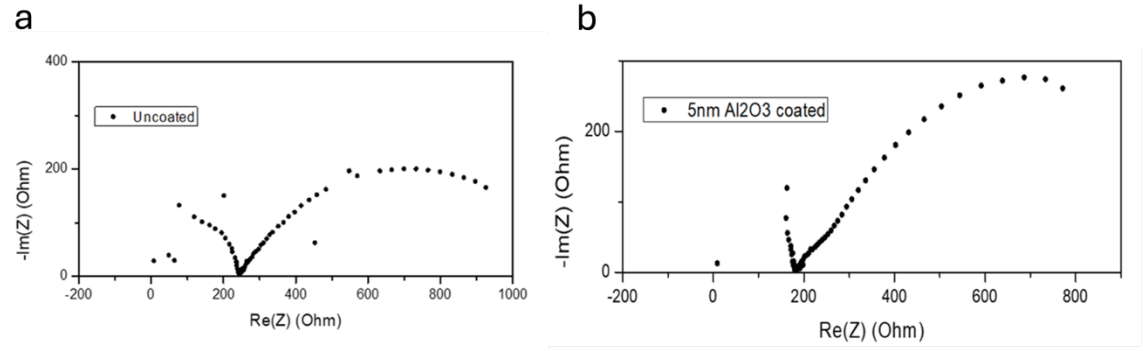


Figure 5.5 EIS results of (a) uncoated and (b) coated symmetrical cell after 150 cycles.

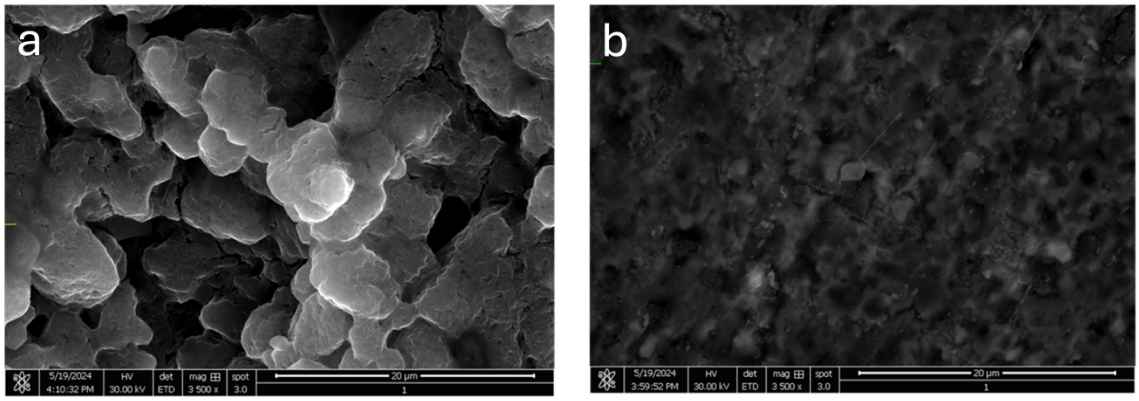


Figure 5.6 SEM results for electrodes of (a) uncoated and (b) coated symmetrical cells after cycling.

In **Figure 5.5**, EIS results show the electrical impedance of an uncoated and 5nm Al_2O_3-coated symmetrical cell after 150 cycles. Both graphs show a similar semi-circular shape, and the 5nm Al_2O_3-coated symmetrical cell has a smaller radius, which indicates lower interfacial resistance. SEM results (**Figure 5.6**) show the morphology of the anodes for uncoated and coated symmetrical cells after 999 cycles, much fewer lithium dendrites and smoother surface can be found for the Al_2O_3-coated symmetrical cell than uncoated one. This can explain the reason why the coated cell has less interfacial resistance and better cycling performance. Overall, the Al_2O_3 coating layer decreases the overpotential and increases the stability of the designed Li_6PS_5Cl-based all-solid-state Li-S battery successfully, further experiments for full cells will be tested.

Chapter 6

6 Conclusions and Recommendations for Future Work

The advancements delineated within this dissertation of next-generation battery technology herald a paradigm shift in energy storage solutions. To fully capitalize on the potential of next-generation batteries, concerted efforts in several strategic research areas and technological innovations are imperative:

6.1 Advancements in Material Science

The progression of material science plays a quintessential role in the evolution of next-generation batteries. Sustained and rigorous research initiatives are imperative for the synthesis and characterization of innovative electrode and solid electrolyte materials, which are the cornerstone of enhancing the overall performance and reliability of batteries.

For Nickel-rich materials, the key issue is to increase the Ni content without going through phase transition, which means increase the capacity without sacrificing the cycle life. For Li-S system, more material modification strategy need to be applied to solve the shuttle effect problem. Enhancing the interface stability is crucial for maintaining long-term battery performance and safety. The interfacial region often presents a significant challenge due to the potential for chemical reactivity and physical mismatches in properties such as thermal expansion coefficients. Advanced surface engineering

techniques, including atomic layer deposition (ALD) or surface coating strategies, could be explored to create stable, compatible interfaces that mitigate degradation mechanisms.

One of the primary objectives in solid-state material development is to augment ionic conductivities within solid electrolytes. Research should focus on the discovery and optimization of materials that facilitate faster ion transport while maintaining electrochemical stability across the battery's operational voltage window. This includes exploring lattice structures that allow easier movement of ions, potentially involving the doping of materials with atoms that can create more mobile ion pathways. Concurrently, it is critical to enhance the mechanical stability of these materials to prevent structural degradations such as cracking or delamination under mechanical stress or thermal fluctuations. This involves engineering materials with robust mechanical properties that can withstand the stresses induced by ionic movement and volume changes during charge-discharge cycles. Research in composite materials or hybrid structures combining polymers and ceramics could provide pathways to achieve these characteristics. Another pivotal aspect of material science research is the operational integrity of SSBs under a diverse array of environmental conditions. Materials must be developed that not only perform optimally in standard conditions but also retain their functional characteristics under extreme temperatures, pressures, or humidity levels. This is particularly relevant for applications ranging from electric vehicles, which require operation in varying climates, to portable electronics, which may encounter various environmental stressors.

By addressing these key areas, the scientific community can substantially advance the material science surrounding next-generation batteries, paving the way for more efficient, durable, and versatile energy storage solutions.

6.2 Scalability and Manufacturing Processes

The advancement from laboratory prototypes to industrial-scale encapsulates a critical phase fraught with technological and engineering challenges. These challenges underscore the need for robust methodologies to uphold the integrity and performance of next-generation batteries during large-scale manufacturing processes. Systematic investigations and innovations are required to establish scalable manufacturing protocols that deliver consistent quality and economically viable production rates.

Implementing rigorous inline quality control systems is vital. These systems would utilize advanced sensing and imaging technologies to monitor the integrity and consistency of materials and components throughout the manufacturing process. Real-time diagnostics coupled with automated feedback mechanisms would ensure the detection and correction of production anomalies, thereby enhancing the yield and reliability of the final products.

To achieve competitive market positioning, developing production strategies that leverage economies of scale is essential. This involves optimizing the material supply chain, reducing energy consumption during manufacturing, and minimizing waste through closed-loop recycling processes. Additionally, partnerships with raw material suppliers and technology developers can help reduce costs and secure supply chains.

Manufacturing processes must also adhere to stringent regulatory standards and environmental guidelines to promote sustainability and reduce ecological impacts. This includes the implementation of cleaner production techniques, the use of non-toxic and recyclable materials, and the adherence to international standards on emissions and waste management.

6.3 Optimization of Fast Charging Capabilities

The advancement of fast-charging technologies is a pivotal aspect of the commercial viability and consumer adoption of next-generation batteries, particularly within the automotive sector. This requires a concerted effort to enhance the batteries' intrinsic fast charging capabilities and integrate sophisticated power management systems. These developments are crucial for meeting consumer expectations and safety standards while extending the operational longevity of the batteries.

The need to improve the ionic conductivity and electron mobility within the battery is at the core of optimizing fast charging. Research should focus on material modifications, such as doping or creating nanostructured materials that facilitate rapid ion transport while maintaining structural stability under rapid charge and discharge cycles.

Addressing thermal management is critical in fast-charging systems. High rates of charging can lead to significant heat generation, which, if not properly managed, can deteriorate battery health and safety. Implementing advanced thermal management solutions, such as heat sinks, cooling systems, or phase change materials, will be essential

to dissipate heat efficiently and maintain the battery's temperature within safe operational limits.

Integrating advanced power management systems is essential for optimizing the charging process and ensuring battery longevity. These systems should be capable of dynamically adjusting the charging rates based on real-time assessments of battery conditions and external factors such as ambient temperature and battery age. Smart charging algorithms that can modulate charge rates to minimize stress and degradation of the battery cells will play a critical role in extending the life span of next-generation batteries.

Fast charging involves higher currents and voltages that increase the risk of mechanical and chemical instabilities within the battery. Developing robust safety mechanisms and protocols is imperative to prevent overcharging, thermal runaway, and other potentially hazardous conditions. These include incorporating sensors that provide continuous monitoring and diagnostics, coupled with automated cutoff systems that can intervene in real time to prevent failures.

The optimization of next-generation batteries fast charging capabilities also involves ensuring compatibility with existing and future electric vehicle charging infrastructure. Collaborations between battery developers, vehicle manufacturers, and infrastructure providers will be crucial to harmonize the technical specifications and ensure seamless integration into the broader EV ecosystem.

By addressing these key areas, the research and development community can enhance the fast-charging capabilities of next-generation batteries, thus meeting the

stringent requirements of the automotive industry and other sectors demanding quick energy replenishment. This will not only boost consumer confidence in electric vehicles but also significantly contribute to the broader adoption of clean energy technologies.

6.4 Enhanced In-Operando Characterization Techniques

The evolution of in-operando characterization methods is crucial for the detailed, real-time monitoring and proactive management of the health and performance of next-generation batteries. These advanced methodologies are instrumental in ensuring optimal operational parameters, enhancing safety profiles, and prolonging the lifespan of these energy storage systems. Developing sophisticated sensing and diagnostic technologies is essential to implementing precise control strategies that adapt to changing operational conditions and maintain battery integrity throughout its lifecycle.

At the forefront of these efforts are the enhancements in sensor technology capable of providing real-time data on critical battery parameters such as temperature, voltage, current, and internal resistance. Innovations may include the integration of nano-sensors within the battery structure that can detect microstructural changes at the electrode and electrolyte levels. These sensors enable the early detection of potential failures, such as electrolyte decomposition or electrode delamination, before they escalate into serious problems.

The integration of high-resolution diagnostic tools, such as acoustic microscopy, optical coherence tomography, and advanced spectroscopy techniques, can offer unprecedented insights into the internal processes of batteries. These tools allow for the

visualization and analysis of the dynamic interactions within the battery during charge and discharge cycles, providing valuable data to optimize battery chemistry and architecture.

Another critical area is leveraging data analytics and machine learning algorithms to interpret the vast amounts of data generated by in-operando diagnostics. These computational tools can predict battery behavior under various conditions and identify optimal operating parameters. By analyzing trends and patterns in the data, machine learning models can forecast potential system failures and suggest preventive measures to extend battery life and enhance performance.

Developing dynamic feedback mechanisms that adjust battery operation based on real-time diagnostics is essential for maintaining battery health. These systems use data from in-operando characterization to modulate charging strategies, manage power output, and activate safety protocols when anomalies are detected. Such adaptive management not only optimizes performance but also significantly mitigates risks associated with battery degradation and failure.

It will be crucial to standardize these advanced in-operando characterization techniques and validate their accuracy and reliability across different battery technologies and applications. This ensures compatibility and comparability of data, facilitating broader implementation and acceptance of these techniques in quality control and regulatory frameworks.

By expanding the capabilities of in-operando characterization techniques, researchers and engineers can significantly enhance the control strategies for batteries,

thereby maximizing their efficiency, safety, and longevity. These advancements will provide the necessary technological foundation to support the deployment of next-generation batteries across a wide range of applications, from consumer electronics to electric vehicles, aligning with the demands of modern energy storage solutions.

6.5 Synergy with Renewable Energy Technologies

Investigative efforts should also encompass the integration of next-generation batteries with renewable energy systems. Next-generation batteries are poised to significantly improve these systems' efficiency and storage capacity, thereby contributing to a more sustainable energy infrastructure.

6.6 Development of Regulatory and Safety Protocols

As the next-generation batteries become more prevalent, establishing comprehensive safety standards and regulatory guidelines will be crucial. These frameworks should ensure the safe application of the next-generation batteries across various domains, including consumer electronics and electric mobility.

Addressing these pivotal areas will enable the research community and industry stakeholders to advance battery technology towards significant market penetration, fulfilling its promise as a cornerstone of next-generation energy storage systems.

7 Bibliography

1. Banos, R., Manzano-Agugliaro, F., Montoya, F., Gil, C., Alcayde, A., and Gómez, J. (2011). Optimization methods applied to renewable and sustainable energy: A review. Renewable and sustainable energy reviews *15*, 1753-1766.

2. Simon, P., Gogotsi, Y., and Dunn, B. (2014). Where do batteries end and supercapacitors begin? Science *343*, 1210-1211.

3. BloombergNEF, N.Y.N. (2019). Electric vehicle outlook 2019. . http://data.bloomberglp.com/bnef/sites/14/2017/07/BNEF_EVO_2017_ExecutiveSummary.pdf.

4. Berckmans, G., Messagie, M., Smekens, J., Omar, N., Vanhaverbeke, L., and Van Mierlo, J. (2017). Cost projection of state of the art lithium-ion batteries for electric vehicles up to 2030. Energies *10*, 1314.

5. L, G.-S. (2019). A behind the scenes take on Lithium-ion battery prices. . https://about.bnef.com/blog/behind-scenes-take-lithium-ion-battery-prices/.

6. Park, M., Zhang, X., Chung, M., Less, G.B., and Sastry, A.M. (2010). A review of conduction phenomena in Li-ion batteries. Journal of power sources *195*, 7904-7929.

7. A, S. (2020). GM's new EV battery to use less cobalt. . https://www.argusmedia.com/en/news/2084749-gms-new-ev-battery-to-use-less-cobalt.

8. Lithium-ion batteries. (2017). https://www.cobaltinstitute.org/lithium-ion-batteries.html.

9. S, L. (2020). Batteries create critical cobalt situation. https://www.miningnewsnorth.com/story/2020/04/03/critical-minerals/batteries-create-critical-cobalt-situation/5749.html.

10. Liu, K., Liu, Y., Lin, D., Pei, A., and Cui, Y. (2018). Materials for lithium-ion battery safety. Science advances *4*, eaas9820.

11. Nitta, N., Wu, F., Lee, J.T., and Yushin, G. (2015). Li-ion battery materials: present and future. Materials today *18*, 252-264.

12. Zuo, X., Zhu, J., Müller-Buschbaum, P., and Cheng, Y.-J. (2017). Silicon based lithium-ion battery anodes: A chronicle perspective review. Nano Energy *31*, 113-143.

13. Zhu, B., Wang, X., Yao, P., Li, J., and Zhu, J. (2019). Towards high energy density lithium battery anodes: silicon and lithium. Chemical science *10*, 7132-7148.

14. Dou, F., Shi, L., Chen, G., and Zhang, D. (2019). Silicon/carbon composite anode materials for lithium-ion batteries. Electrochemical Energy Reviews *2*, 149-198.

15. Zhou, Y., Yang, Y., Hou, G., Yi, D., Zhou, B., Chen, S., Dai Lam, T., Yuan, F., Golberg, D., and Wang, X. (2020). Stress-relieving defects enable ultra-stable silicon anode for Li-ion storage. Nano Energy *70*, 104568.

16. Liang, B., Liu, Y., and Xu, Y. (2014). Silicon-based materials as high capacity anodes for next generation lithium ion batteries. Journal of Power sources *267*, 469-490.

17. Ma, D., Cao, Z., and Hu, A. (2014). Si-based anode materials for Li-ion batteries: a mini review. Nano-micro letters *6*, 347-358.

18. Zhang, R., Du, Y., Li, D., Shen, D., Yang, J., Guo, Z., Liu, H.K., Elzatahry, A.A., and Zhao, D. (2014). Highly reversible and large lithium storage in mesoporous si/c nanocomposite anodes with silicon nanoparticles embedded in a carbon framework. Advanced Materials (Deerfield Beach, Fla.) *26*, 6749-6755.

19. Gribov, B., and Zinov'Ev, K. (2003). Preparation of high-purity silicon for solar cells. Inorganic materials *39*, 653-662.

20. Vlad, A., Reddy, A.L.M., Ajayan, A., Singh, N., Gohy, J.-F., Melinte, S., and Ajayan, P.M. (2012). Roll up nanowire battery from silicon chips. Proceedings of the National Academy of Sciences *109*, 15168-15173.

21. Cui, Y., Lauhon, L.J., Gudiksen, M.S., Wang, J., and Lieber, C.M. (2001). Diameter-controlled synthesis of single-crystal silicon nanowires. Applied Physics Letters *78*, 2214-2216.

22. Law, M., Goldberger, J., and Yang, P. (2004). Semiconductor nanowires and nanotubes. Annu. Rev. Mater. Res. *34*, 83-122.

23. Yao, Y., McDowell, M.T., Ryu, I., Wu, H., Liu, N., Hu, L., Nix, W.D., and Cui, Y. (2011). Interconnected silicon hollow nanospheres for lithium-ion battery anodes with long cycle life. Nano letters *11*, 2949-2954.

24. Favors, Z., Wang, W., Bay, H.H., Mutlu, Z., Ahmed, K., Liu, C., Ozkan, M., and Ozkan, C.S. (2014). Scalable synthesis of nano-silicon from beach sand for long cycle life Li-ion batteries. Scientific reports *4*, 5623.

25. Campbell, B., Ionescu, R., Tolchin, M., Ahmed, K., Favors, Z., Bozhilov, K.N., Ozkan, C.S., and Ozkan, M. (2016). Carbon-coated, diatomite-derived nanosilicon as a high rate capable Li-ion battery anode. Scientific reports *6*, 33050.

26. Bendixen, M., Best, J., Hackney, C., and Iversen, L.L. (2019). Time is running out for sand. Nature *571*, 29-31.

27. Campbell, B., Ionescu, R., Favors, Z., Ozkan, C.S., and Ozkan, M. (2015). Bio-derived, binderless, hierarchically porous carbon anodes for Li-ion batteries. Scientific reports *5*, 14575.

28. Li, C., Liu, C., Wang, W., Mutlu, Z., Bell, J., Ahmed, K., Ye, R., Ozkan, M., and Ozkan, C.S. (2017). Silicon derived from glass bottles as anode materials for lithium ion full cell batteries. Scientific reports *7*, 917.

29. Calvert, R. (1930). Diatomaceous earth. Journal of Chemical Education *7*, 2829.

30. Şan, O., Gören, R., and Özgür, C. (2009). Purification of diatomite powder by acid leaching for use in fabrication of porous ceramics. International Journal of Mineral Processing *93*, 6-10.

31. ., U.S.G.S. (2020). Mineral commodity summaries 2020. https://pubs.usgs.gov/periodicals/mcs2020/mcs2020.pdf.

32. (Austria), B.B.V. (2001). Nuclear graphite waste management.

33. Hong, K.-l., Qie, L., Zeng, R., Yi, Z.-q., Zhang, W., Wang, D., Yin, W., Wu, C., Fan, Q.-j., and Zhang, W.-x. (2014). Biomass derived hard carbon used as a high performance anode material for sodium ion batteries. Journal of materials chemistry a *2*, 12733-12738.

34. Buiel, E., and Dahn, J. (1999). Li-insertion in hard carbon anode materials for Li-ion batteries. Electrochimica acta *45*, 121-130.

35. Luo, W., Schardt, J., Bommier, C., Wang, B., Razink, J., Simonsen, J., and Ji, X. (2013). Carbon nanofibers derived from cellulose nanofibers as a long-life anode material for rechargeable sodium-ion batteries. Journal of Materials Chemistry A *1*, 10662-10666.

36. Romanos, J., Beckner, M., Rash, T., Firlej, L., Kuchta, B., Yu, P., Suppes, G., Wexler, C., and Pfeifer, P. (2011). Nanospace engineering of KOH activated carbon. Nanotechnology *23*, 015401.

37. Lv, Y., Zhang, F., Dou, Y., Zhai, Y., Wang, J., Liu, H., Xia, Y., Tu, B., and Zhao, D. (2012). A comprehensive study on KOH activation of ordered mesoporous carbons and their supercapacitor application. Journal of Materials Chemistry *22*, 93-99.

38. Weinstein, L., and Dash, R. (2013). Supercapacitor carbons. Materials today *10*, 356-357.

39. Liu, N., Huo, K., McDowell, M.T., Zhao, J., and Cui, Y. (2013). Rice husks as a sustainable source of nanostructured silicon for high performance Li-ion battery anodes. Scientific reports *3*, 1-7.

40. Liu, J., Kopold, P., van Aken, P.A., Maier, J., and Yu, Y. (2015). Energy storage materials from nature through nanotechnology: a sustainable route from reed plants to a silicon anode for lithium‐ion batteries. Angewandte Chemie *127*, 9768-9772.

41. Wang, L., Gao, B., Peng, C., Peng, X., Fu, J., Chu, P.K., and Huo, K. (2015). Bamboo leaf derived ultrafine Si nanoparticles and Si/C nanocomposites for high-performance Li-ion battery anodes. Nanoscale *7*, 13840-13847.

42. Si, R., Dai, Q., Guo, S., and Wang, J. (2020). Mechanical property, nanopore structure and drying shrinkage of metakaolin-based geopolymer with waste glass powder. Journal of Cleaner Production *242*, 118502.

43. Miandad, R., Rehan, M., Barakat, M.A., Aburiazaiza, A.S., Khan, H., Ismail, I.M., Dhavamani, J., Gardy, J., Hassanpour, A., and Nizami, A.-S. (2019). Catalytic pyrolysis of plastic waste: moving toward pyrolysis based biorefineries. Frontiers in energy research *7*, 437000.

44. Jambeck, J.R., Geyer, R., Wilcox, C., Siegler, T.R., Perryman, M., Andrady, A., Narayan, R., and Law, K.L. (2015). Plastic waste inputs from land into the ocean. science *347*, 768-771.

45. Cook, C.R., and Halden, R.U. (2020). Ecological and health issues of plastic waste. In Plastic waste and recycling, (Elsevier), pp. 513-527.

46. Momma, K., and Izumi, F. (2011). VESTA 3 for three-dimensional visualization of crystal, volumetric and morphology data. Journal of applied crystallography *44*, 1272-1276.

47. Zerrin, T., Ozkan, M., and Ozkan, C.S. (2018). Improved electrochemical performance of LiCoO2 electrodes for high-voltage operations by Ag thin film coating via magnetron sputtering. MRS Advances *3*, 3513-3518.

48. R, C. (2019). State of charge: EVs, batteries and battery materials. https://www.adamasintel.com/state-of-charge-2019-h1/.

49. Li, T., Yuan, X.-Z., Zhang, L., Song, D., Shi, K., and Bock, C. (2020). Degradation mechanisms and mitigation strategies of nickel-rich NMC-based lithium-ion batteries. Electrochemical Energy Reviews *3*, 43-80.

50. Li, Y., Tan, Z., Liu, Y., Lei, C., He, P., Li, J., He, Z., Cheng, Y., Wu, F., and Li, Y. (2023). Past, present and future of high-nickel materials. Nano Energy, 109070.

51. Lv, F., Liu, J., Ye, Y., Wu, Z., Wang, Q., Sun, Y., and Yuan, S. (2024). Material design strategies for high-nickel ternary cathode materials. Journal of Energy Storage *97*, 112828.

52. Xu, C., Reeves, P.J., Jacquet, Q., and Grey, C.P. (2021). Phase behavior during electrochemical cycling of Ni‐rich cathode materials for Li‐ion batteries. Advanced Energy Materials *11*, 2003404.

53. Song, L., Du, J., Xiao, Z., Jiang, P., Cao, Z., and Zhu, H. (2020). Research progress on the surface of high-nickel nickel–cobalt–manganese ternary cathode materials: a mini review. Frontiers in Chemistry *8*, 761.

54. Wang, F., and Bai, J. (2022). Synthesis and Processing by Design of High‐Nickel Cathode Materials. Batteries & Supercaps *5*, e202100174.

55. Chu, S., Cui, Y., and Liu, N. (2017). The path towards sustainable energy. Nature materials *16*, 16-22.

56. Zhao, J., Chen, D., Boateng, B., Zeng, G., Han, Y., Zhen, C., Goodenough, J.B., and He, W. (2020). Atomic interlamellar ion path in polymeric separator enables long-life and dendrite-free anode in lithium ion batteries. Journal of Power Sources *451*, 227773.

57. Liu, Y., Lei, T., Li, Y., Chen, W., Hu, Y., Huang, J., Chu, J., Yan, C., Wu, C., and Yang, C. (2023). Entrapment of polysulfides by a BiFeO3/TiO2 heterogeneous structure on separator for high-performance Li–S batteries. Journal of Power Sources *556*, 232501.

58. Zhou, G., Chen, H., and Cui, Y. (2022). Formulating energy density for designing practical lithium–sulfur batteries. Nature Energy *7*, 312-319.

59. Shang, R., Zerrin, T., Dong, B., Ozkan, C.S., and Ozkan, M. (2020). Sustainable and Low-Cost Lithium-Ion Batteries: Nonconventional Electrode Chemistries and State of Health Characterization. Technology & Innovation *21*, 1-23.

60. Ma, Y., Shang, R., Liu, Y., Lake, R., Ozkan, M., and Ozkan, C.S. (2023). Enabling fast-charging capability for all-solid-state lithium-ion batteries. Journal of Power Sources *559*, 232647.

61. Pang, Q., Liang, X., Kwok, C.Y., and Nazar, L.F. (2016). Advances in lithium–sulfur batteries based on multifunctional cathodes and electrolytes. Nature Energy *1*, 16132. 10.1038/nenergy.2016.132.

62. Deng, R., Wang, M., Yu, H., Luo, S., Li, J., Chu, F., Liu, B., and Wu, F. (2022). Recent advances and applications toward emerging lithium–sulfur batteries: working principles and opportunities. Energy & Environmental Materials *5*, 777-799.

63. Bi, C.-X., Hou, L.-P., Li, Z., Zhao, M., Zhang, X.-Q., Li, B.-Q., Zhang, Q., and Huang, J.-Q. (2023). Protecting lithium metal anodes in lithium–sulfur batteries: A review. Energy Material Advances *4*, 0010.

64. Wang, J., Wang, H., Jia, S., Zhao, Q., Zheng, Q., Ma, Y., Ma, T., and Li, X. (2023). Recent advances in inhibiting shuttle effect of polysulfide in lithium-sulfur batteries. Journal of Energy Storage *72*, 108372.

65. Shaibani, M., Mirshekarloo, M.S., Singh, R., Easton, C.D., Cooray, M.C.D., Eshraghi, N., Abendroth, T., Dörfler, S., Althues, H., Kaskel, S., et al. (2020). Expansion-tolerant architectures for stable cycling of ultrahigh-loading sulfur cathodes in lithium-sulfur batteries. Science Advances *6*, eaay2757. doi:10.1126/sciadv.aay2757.

66. Choi, J.M., Saroha, R., Kim, J.S., Jang, M.R., and Cho, J.S. (2023). Porous nanofibers comprising VN nanodots and densified N-doped CNTs as redox-active interlayers for Li–S batteries. Journal of Power Sources *559*, 232632.

67. Ma, L., Zhuang, H.L., Wei, S., Hendrickson, K.E., Kim, M.S., Cohn, G., Hennig, R.G., and Archer, L.A. (2016). Enhanced Li–S batteries using amine-functionalized carbon nanotubes in the cathode. ACS nano *10*, 1050-1059.

68. Yang, J., Qiao, W., Qiao, J., Gao, H., Li, Z., Wang, P., Cao, C., Tang, C., and Xue, Y. (2022). Enhanced Performance of Li–S Batteries due to Synergistic Adsorption

and Catalysis Activity within a Separation Coating Made of Hybridized BNNSs/N-Doping Porous Carbon Fibers. ACS Applied Materials & Interfaces *14*, 48558-48569.

69. Chen, M., Su, Z., Jiang, K., Pan, Y., Zhang, Y., and Long, D. (2019). Promoting sulfur immobilization by a hierarchical morphology of hollow carbon nanosphere clusters for high-stability Li–S battery. Journal of Materials Chemistry A *7*, 6250-6258.

70. Hu, C., Chen, H., Shen, Y., Lu, D., Zhao, Y., Lu, A.-H., Wu, X., Lu, W., and Chen, L. (2017). In situ wrapping of the cathode material in lithium-sulfur batteries. Nature communications *8*, 479.

71. Zhang, Z., Lai, Y., Zhang, Z., Zhang, K., and Li, J. (2014). Al2O3-coated porous separator for enhanced electrochemical performance of lithium sulfur batteries. Electrochimica Acta *129*, 55-61.

72. Xiao, Z., Yang, Z., Wang, L., Nie, H., Zhong, M.e., Lai, Q., Xu, X., Zhang, L., and Huang, S. (2015). A lightweight TiO2/graphene interlayer, applied as a highly effective polysulfide absorbent for fast, long‐life lithium–sulfur batteries. Advanced materials *27*, 2891-2898.

73. Ni, L., Wu, Z., Zhao, G., Sun, C., Zhou, C., Gong, X., and Diao, G. (2017). Core–Shell Structure and Interaction Mechanism of γ‐MnO2 Coated Sulfur for Improved Lithium‐Sulfur Batteries. Small *13*, 1603466.

74. Strubel, P., Thieme, S., Biemelt, T., Helmer, A., Oschatz, M., Brückner, J., Althues, H., and Kaskel, S. (2015). ZnO hard templating for synthesis of hierarchical porous carbons with tailored porosity and high performance in lithium‐sulfur battery. Advanced Functional Materials *25*, 287-297.

75. Ge, Y., Chen, P., Zhang, W., Shan, Q., Fang, Y., Chen, N., Yuan, Z., Zhang, Y., and Feng, X. (2020). Shape-controlled MnO 2 as a sulfur host for high performance lithium–sulfur batteries. New Journal of Chemistry *44*, 11365-11372.

76. Yu, M., Yuan, W., Li, C., Hong, J.-D., and Shi, G. (2014). Performance enhancement of a graphene–sulfur composite as a lithium–sulfur battery electrode by coating with an ultrathin Al 2 O 3 film via atomic layer deposition. Journal of Materials Chemistry A *2*, 7360-7366.

77. Zhang, J., Zhang, G., Chen, Z., Dai, H., Hu, Q., Liao, S., and Sun, S. (2020). Emerging applications of atomic layer deposition for lithium-sulfur and sodium-sulfur batteries. Energy Storage Materials *26*, 513-533.

78. Yan, B., Li, X., Bai, Z., Song, X., Xiong, D., Zhao, M., Li, D., and Lu, S. (2017). A review of atomic layer deposition providing high performance lithium sulfur batteries. Journal of Power Sources *338*, 34-48.

79. Carter, R., Oakes, L., Muralidharan, N., Cohn, A.P., Douglas, A., and Pint, C.L. (2017). Polysulfide anchoring mechanism revealed by atomic layer deposition of V2O5 and sulfur-filled carbon nanotubes for lithium–sulfur batteries. ACS applied materials & interfaces *9*, 7185-7192.

80. Cunningham, W.A. (1935). Sulfur. III. Journal of Chemical Education *12*, 120.

81. Funke, K. (2013). Solid State Ionics: from Michael Faraday to green energy—the European dimension. Science and Technology of Advanced Materials *14*, 043502.

82. Janek, J., and Zeier, W.G. (2016). A solid future for battery development. Nature energy *1*, 1-4.

83. Janek, J., and Zeier, W.G. (2023). Challenges in speeding up solid-state battery development. Nature Energy *8*, 230-240.

84. Bell, J., Ye, R., Ahmed, K., Liu, C., Ozkan, M., and Ozkan, C.S. (2015). Free-standing Ni–NiO nanofiber cloth anode for high capacity and high rate Li-ion batteries. Nano Energy *18*, 47-56.

85. Dudney, N.J., West, W.C., and Nanda, J. (2015). Handbook of solid state batteries (World Scientific).

86. Rahardian, S., Budiman, B.A., Sambegoro, P.L., and Nurprasetio, I.P. (2019). Review of solid-state battery technology progress. (IEEE), pp. 310-315.

87. Sun, Y.-K. (2020). Promising all-solid-state batteries for future electric vehicles. ACS Publications.

88. Horowitz, Y., Schmidt, C., Yoon, D.-h., Riegger, L.M., Katzenmeier, L., Bosch, G.M., Noked, M., Ein-Eli, Y., Janek, J., and Zeier, W.G. (2020). Between liquid and all solid: a prospect on electrolyte future in lithium‐ion batteries for electric vehicles. Energy Technology *8*, 2000580.

89. England, R. (2018). A Chinese startup may have cracked solid-state batteries. https://www.engadget.com/2018-11-21-chinese-startup-solid-state-batteries-production.html.

90. Weiss, M., Ruess, R., Kasnatscheew, J., Levartovsky, Y., Levy, N.R., Minnmann, P., Stolz, L., Waldmann, T., Wohlfahrt‐Mehrens, M., and Aurbach, D. (2021). Fast charging of lithium‐ion batteries: a review of materials aspects. Advanced Energy Materials *11*, 2101126.

91. Chen, R., Li, Q., Yu, X., Chen, L., and Li, H. (2019). Approaching practically accessible solid-state batteries: stability issues related to solid electrolytes and interfaces. Chemical reviews *120*, 6820-6877.

92. Li, C., Wang, Z.-y., He, Z.-j., Li, Y.-j., Mao, J., Dai, K.-h., Yan, C., and Zheng, J.-c. (2021). An advance review of solid-state battery: Challenges, progress and prospects. Sustainable Materials and Technologies *29*, e00297.

93. Favors, Z., Wang, W., Bay, H.H., George, A., Ozkan, M., and Ozkan, C.S. (2014). Stable cycling of SiO2 nanotubes as high-performance anodes for lithium-ion batteries. Scientific reports *4*, 4605.

94. Wang, W., Favors, Z., Ionescu, R., Ye, R., Bay, H.H., Ozkan, M., and Ozkan, C.S. (2015). Monodisperse porous silicon spheres as anode materials for lithium ion batteries. Scientific reports *5*, 8781.

95. Zerrin, T., Shang, R., Dong, B., Aguilar, E.C., Malvin, J., Ozkan, M., and Ozkan, C.S. (2022). An overlooked parameter in Li-S batteries: the impact of electrolyte-to-sulfur ratio on capacity fading. Nano Energy *104*, 107913.

96. Yu, X., Chen, R., Gan, L., Li, H., and Chen, L. (2023). Battery safety: From lithium-ion to solid-state batteries. Engineering *21*, 9-14.

97. Ferrari, S., Falco, M., Muñoz‐García, A.B., Bonomo, M., Brutti, S., Pavone, M., and Gerbaldi, C. (2021). Solid‐state post Li metal ion batteries: a sustainable forthcoming reality? Advanced Energy Materials *11*, 2100785.

98. Famprikis, T., Canepa, P., Dawson, J.A., Islam, M.S., and Masquelier, C. (2019). Fundamentals of inorganic solid-state electrolytes for batteries. Nature materials *18*, 1278-1291.

99. Mirjalili, A., Dong, B., Zerrin, T., Akhavi, A.-A., Kurban, M., Ozkan, C.S., and Ozkan, M. (2023). Superporous nanocarbon materials upcycled from polyethylene terephthalate waste for scalable energy storage. Journal of Energy Storage *58*, 106329.

100. Li, C., Liu, C., Wang, W., Bell, J., Mutlu, Z., Ahmed, K., Ye, R., Ozkan, M., and Ozkan, C.S. (2016). Towards flexible binderless anodes: silicon/carbon fabrics via double-nozzle electrospinning. Chemical communications *52*, 11398-11401.

101. Ren, Y., Shen, Y., Lin, Y., and Nan, C.-W. (2015). Direct observation of lithium dendrites inside garnet-type lithium-ion solid electrolyte. Electrochemistry Communications *57*, 27-30.

102. Wang, Z., Li, X., Chen, Y., Pei, K., Mai, Y.-W., Zhang, S., and Li, J. (2020). Creep-enabled 3D solid-state lithium-metal battery. Chem *6*, 2878-2892.

103. Perdew, J.P., Burke, K., and Ernzerhof, M. (1996). Generalized gradient approximation made simple. Physical review letters *77*, 3865.

104. Scandolo, S., Giannozzi, P., Cavazzoni, C., de Gironcoli, S., Pasquarello, A., and Baroni, S. (2005). First-principles codes for computational crystallography in the Quantum-ESPRESSO package. Zeitschrift für Kristallographie-Crystalline Materials *220*, 574-579.

105. Giannozzi, P., Baroni, S., Bonini, N., Calandra, M., Car, R., Cavazzoni, C., Ceresoli, D., Chiarotti, G.L., Cococcioni, M., and Dabo, I. (2009). QUANTUM ESPRESSO: a modular and open-source software project for quantum simulations of materials. Journal of physics: Condensed matter *21*, 395502.

106. Vanderbilt, D. (1990). Soft self-consistent pseudopotentials in a generalized eigenvalue formalism. Physical review B *41*, 7892.

107. Makov, G., and Payne, M.C. (1995). Periodic boundary conditions in ab initio calculations. Physical Review B *51*, 4014.

108. Fletcher, R. (1970). A new approach to variable metric algorithms. The computer journal *13*, 317-322.

109. Li, C.-Y., Yu, Y., Wang, C., Zhang, Y., Zheng, S.-Y., Li, J.-F., Maglia, F., Jung, R., Tian, Z.-Q., and Shao-Horn, Y. (2020). Surface Changes of LiNi x Mn y Co1–x–y O2 in Li-Ion Batteries Using in Situ Surface-Enhanced Raman Spectroscopy. The Journal of Physical Chemistry C *124*, 4024-4031.

110. Tu, R., Liu, Z., Wang, C., Lu, P., Guo, B., Xu, Q., Li, B.-W., and Zhang, S. (2022). High-throughput growth of HfO 2 films using temperature-gradient laser chemical vapor deposition. RSC advances *12*, 15555-15563.

111. Dhanunjaya, M., Byram, C., Vendamani, V., Rao, S.V., Pathak, A., and Rao, S.N. (2019). Hafnium oxide nanoparticles fabricated by femtosecond laser ablation in water. Applied Physics A *125*, 1-7.

112. Wang, T., Jiao, X., Rao, L., Stout, M., Gibson, A., Kidner, N., Choi, J., and Kim, J.-H. (2023). Li0. 5La0. 5TiO3 as an Ionic Conducting Additive Enhancing the High-Voltage Performance of LiNi0. 8Mn0. 1Co0. 1O2 Cathodes in Lithium-Ion Batteries. ACS Applied Materials & Interfaces *15*, 39234-39244.

113. Llanos, P.S., Ahaliabadeh, Z., Miikkulainen, V., Lahtinen, J., Yao, L., Jiang, H., Kankaanpää, T., and Kallio, T.M. (2024). High Voltage Cycling Stability of LiF-Coated NMC811 Electrode. ACS Applied Materials & Interfaces *16*, 2216-2230.

114. Maleki Kheimeh Sari, H., and Li, X. (2019). Controllable cathode–electrolyte interface of Li [Ni0. 8Co0. 1Mn0. 1] O2 for lithium ion batteries: a review. Advanced Energy Materials *9*, 1901597.

115. Jabeen, M., Ren, Z., Ishaq, M., Yuan, S., Bao, X., Shu, C., Liu, X., Liu, X., Li, L., and He, Y.-S. (2023). Stable Operation Induced by Plastic Crystal Electrolyte Used in Ni-Rich NMC811 Cathodes for Li-Ion Batteries. ACS Applied Materials & Interfaces *15*, 51059-51071.

116. Zhang, S.S. (2020). Understanding of performance degradation of LiNi0. 80Co0. 10Mn0. 10O2 cathode material operating at high potentials. Journal of energy chemistry *41*, 135-141.

117. Zhang, H., Liu, H., Piper, L.F., Whittingham, M.S., and Zhou, G. (2022). Oxygen loss in layered oxide cathodes for Li-ion batteries: mechanisms, effects, and mitigation. Chemical reviews *122*, 5641-5681.

118. Dong, Y., and Li, J. (2022). Oxide cathodes: functions, instabilities, self healing, and degradation mitigations. Chemical Reviews *123*, 811-833.

119. Cheng, Y., Zhang, L., Zhang, Q., Li, J., Tang, Y., Delmas, C., Zhu, T., Winter, M., Wang, M.-S., and Huang, J. (2021). Understanding all solid-state lithium batteries through in situ transmission electron microscopy. Materials Today *42*, 137-161.

120. Marker, K., Reeves, P.J., Xu, C., Griffith, K.J., and Grey, C.P. (2019). Evolution of structure and lithium dynamics in LiNi0. 8Mn0. 1Co0. 1O2 (NMC811) cathodes during electrochemical cycling. Chemistry of Materials *31*, 2545-2554.

121. Zhang, D., Li, Y., Xi, X., Wang, S., Hao, S., Lei, T., Ren, X., Xiong, Y., Liu, S., and Zheng, J. (2022). Enhanced interfacial stability of Ni-rich cathode for Li-ion

batteries towards excellent high-voltage performance. Journal of Alloys and Compounds *906*, 164286.

122. Baazizi, M., Karbak, M., Aqil, M., Sayah, S., Dahbi, M., and Ghamouss, F. (2023). High-Valence Surface-Modified LMO Cathode Materials for Lithium-Ion Batteries: Diffusion Kinetics and Operando Thermal Stability Investigation. ACS Applied Materials & Interfaces *15*, 40385-40396.

123. Laskar, M.R., Jackson, D.H., Xu, S., Hamers, R.J., Morgan, D., and Kuech, T.F. (2017). Atomic layer deposited MgO: a lower overpotential coating for Li [Ni0. 5Mn0. 3Co0. 2] O2 cathode. ACS applied materials & interfaces *9*, 11231-11239.

124. Xu, C., Yang, W., Xiang, W., Wu, Z., Song, Y., Wang, G., Liu, Y., Yan, H., Zhang, B., and Zhong, B. (2020). Key parameter optimization for the continuous synthesis of Ni-rich Ni–Co–Al cathode materials for lithium-ion batteries. Industrial & Engineering Chemistry Research *59*, 22549-22558.

125. Huang, B., Liu, D., Zhang, L., Qian, K., Zhou, K., Cai, X., Kang, F., and Li, B. (2019). An efficient synthetic method to prepare high-performance Ni-rich LiNi0. 8Co0. 1Mn0. 1O2 for lithium-ion batteries. ACS Applied Energy Materials *2*, 7403-7411.

126. Wu, S., Li, C., Zhang, J., Wang, P., Zhao, D., Quan, Y., Sun, J., Cui, X., and Li, S. (2023). Inhibition of transition-metal dissolution with an inert soluble product interface constructed by high-concentration electrolyte. Iscience *26*.

127. Xu, J., Jia, C., Cao, B., and Zhang, W. (2007). Electrochemical properties of anatase TiO2 nanotubes as an anode material for lithium-ion batteries. Electrochimica acta *52*, 8044-8047.

128. Laoire, C.O., Mukerjee, S., Abraham, K., Plichta, E.J., and Hendrickson, M.A. (2009). Elucidating the mechanism of oxygen reduction for lithium-air battery applications. The Journal of Physical Chemistry C *113*, 20127-20134.

129. Hou, J., Yao, Y., Wang, Y., Yang, W., Wang, F., Dong, P., Wang, X., Zhang, Y., Li, X., and Zhang, Y. (2023). Application of two-dimensional lamellar lithium titanate in lithium-ion anode batteries. Electrochemistry Communications *156*, 107588.

130. McClelland, I., Booth, S.G., Anthonisamy, N.N., Middlemiss, L.A., Pérez, G.E., Cussen, E.J., Baker, P.J., and Cussen, S.A. (2023). Direct observation of dynamic lithium diffusion behavior in nickel-rich, LiNi0. 8Mn0. 1Co0. 1O2 (NMC811) cathodes using operando muon spectroscopy. Chemistry of Materials *35*, 4149-4158.

131. Rolandi, A.C., Pozo-Gonzalo, C., De Meatza, I., Casado, N., Mecerreyes, D., and Forsyth, M. (2023). Fluorine‐Free Poly (ionic Liquid) s Binders for the Aqueous Processing of High‐Voltage NMC811 Cathodes. Advanced Energy and Sustainability Research *4*, 2300149.

132. Zhang, Y., Katayama, Y., Tatara, R., Giordano, L., Yu, Y., Fraggedakis, D., Sun, J.G., Maglia, F., Jung, R., and Bazant, M.Z. (2020). Revealing electrolyte oxidation via carbonate dehydrogenation on Ni-based oxides in Li-ion batteries by in situ Fourier transform infrared spectroscopy. Energy & Environmental Science *13*, 183-199.

133. Li, Y., Dong, B., Zerrin, T., Jauregui, E., Wang, X., Hua, X., Ravichandran, D., Shang, R., Xie, J., and Ozkan, M. (2020). State‐of‐health prediction for lithium‐ion batteries via electrochemical impedance spectroscopy and artificial neural networks. Energy Storage *2*, e186.

134. Yao, W., Xu, J., Cao, Y., Meng, Y., Wu, Z., Zhan, L., Wang, Y., Zhang, Y., Manke, I., and Chen, N. (2022). Dynamic Intercalation–Conversion Site Supported Ultrathin 2D Mesoporous SnO2/SnSe2 Hybrid as Bifunctional Polysulfide Immobilizer and Lithium Regulator for Lithium–Sulfur Chemistry. ACS nano *16*, 10783-10797.

135. Hu, N., Lv, X., Dai, Y., Fan, L., Xiong, D., and Li, X. (2018). SnO2/reduced graphene oxide interlayer mitigating the shuttle effect of Li–S batteries. ACS applied materials & interfaces *10*, 18665-18674.

136. Li, X., Lu, Y., Hou, Z., Zhang, W., Zhu, Y., Qian, Y., Liang, J., and Qian, Y. (2016). SnS2-compared to SnO2-stabilized S/C composites toward high-performance lithium sulfur batteries. ACS applied materials & interfaces *8*, 19550-19557.

137. Yan, J., Liu, X., and Li, B. (2016). Capacity fade analysis of sulfur cathodes in lithium–sulfur batteries. Advanced Science *3*, 1600101.

138. Busche, M.R., Adelhelm, P., Sommer, H., Schneider, H., Leitner, K., and Janek, J. (2014). Systematical electrochemical study on the parasitic shuttle-effect in lithium-sulfur-cells at different temperatures and different rates. Journal of power sources *259*, 289-299.

139. Zeng, Q., Li, X., Gong, W., Guo, S., Ouyang, Y., Li, D., Xiao, Y., Tan, C., Xie, L., and Lu, H. (2022). Copolymerization of sulfur chains with vinyl functionalized metal− organic framework for accelerating redox kinetics in lithium− sulfur batteries. Advanced Energy Materials *12*, 2104074.

140. Wang, M., Fan, L., Tian, D., Wu, X., Qiu, Y., Zhao, C., Guan, B., Wang, Y., Zhang, N., and Sun, K. (2018). Rational design of hierarchical SnO2/1T-MoS2 nanoarray electrode for ultralong-life Li–S batteries. ACS Energy Letters *3*, 1627-1633.

141. Huang, Y., Lin, L., Zhang, C., Liu, L., Li, Y., Qiao, Z., Lin, J., Wei, Q., Wang, L., and Xie, Q. (2022). Recent advances and strategies toward polysulfides shuttle inhibition for high‐performance Li–S batteries. Advanced Science *9*, 2106004.

142. Lin, D., Liu, Y., and Cui, Y. (2017). Reviving the lithium metal anode for high-energy batteries. Nature nanotechnology *12*, 194-206.

143. Zerrin, T., Kurban, M., Dickson, M.M., Ozkan, M., and Ozkan, C.S. (2020). Suppression of the shuttle effect in Li–S batteries via magnetron sputtered TiO2 thin film at the electrode–electrolyte interface. ACS Applied Energy Materials *3*, 1515-1529.

144. Chen, J.-J., Yuan, R.-M., Feng, J.-M., Zhang, Q., Huang, J.-X., Fu, G., Zheng, M.-S., Ren, B., and Dong, Q.-F. (2015). Conductive Lewis base matrix to recover the missing link of Li2S8 during the sulfur redox cycle in Li–S battery. Chemistry of materials *27*, 2048-2055.

145. Liu, B., Huang, Y., Wen, Y., Du, L., Zeng, W., Shi, Y., Zhang, F., Zhu, G., Xu, X., and Wang, Y. (2012). Highly dispersive {001} facets-exposed nanocrystalline TiO 2 on high quality graphene as a high performance photocatalyst. Journal of Materials Chemistry *22*, 7484-7491.

146. Zhang, Q., Wang, Y., Seh, Z.W., Fu, Z., Zhang, R., and Cui, Y. (2015). Understanding the anchoring effect of two-dimensional layered materials for lithium–sulfur batteries. Nano letters *15*, 3780-3786.

147. Qiu, Y., Li, W., Zhao, W., Li, G., Hou, Y., Liu, M., Zhou, L., Ye, F., Li, H., and Wei, Z. (2014). High-rate, ultralong cycle-life lithium/sulfur batteries enabled by nitrogen-doped graphene. Nano letters *14*, 4821-4827.

148. Chen, S., Nie, L., Shi, H., Hu, X., Wang, Z., Zhang, X., Zhang, Y., Hu, Q., Gao, T., and Yu, Y. (2023). Ultrafast carbonized wood of electrode-scaled aligned-porous structure for high-performance lithium batteries. Transactions of Tianjin University *29*, 387-394.

149. Lee, J., Choi, C., Park, J.B., Yu, S., Ha, J., Lee, H., Jang, G., Park, Y.S., Yun, J., and Im, H. (2023). Optimally arranged TiO2@ MoS2 heterostructures with effectively induced built-in electric field for high-performance lithium–sulfur batteries. Journal of Energy Chemistry.

150. Xu, G., Li, L., Li, M., Xi, C., Yan, J., Li, R., Chao, Y., Yang, C., and Yu, Y. (2022). Suitable polysulfides adsorption and conversion on MoSe2@ g-C3N4 interlayer for advanced lithium-sulfur batteries. Applied Surface Science *604*, 154556.

151. Bai, Y., Nguyen, T.T., Chu, R., Song, H., Kim, N.H., and Lee, J.H. (2023). Heterostructured TiN/TiO2 on the hierarchical N-doped carbon for enhancing the polysulfide immobilization and sulfur reduction in lithium-sulfur battery. Chemical Engineering Journal *476*, 146581.

152. Bai, Y., Nguyen, T.T., Chu, R., Kim, N.H., and Lee, J.H. (2023). Core-shell hollow nanostructures as highly efficient polysulfide conversion and adsorption cathode for shuttle-free lithium-sulfur batteries. Chemical Engineering Journal *454*, 140338.

153. Yang, H., Li, L., Shan, Y., Chen, X., Zhao, Y., and Fan, S. (2023). CuO-ZnO heterojunction doped 2D ultrathin carbon nanosheet catalyzes rapid charge-transfer kinetics of lithium-sulfur batteries. Applied Surface Science, 157738.

154. Li, J., Xu, Y., Hou, W., and Yao, X. (2023). Loading Fe3O4 nanoparticles on N, S co-doped graphene suppressing polysulfides conversion toward high-performance Li–S batteries. Journal of Materials Science *58*, 4552-4564.

155. Mukherjee, S., Kavalsky, L., Chattopadhyay, K., and Singh, C.V. (2018). Adsorption and diffusion of lithium polysulfides over blue phosphorene for Li–S batteries. Nanoscale *10*, 21335-21352.

156. Xiang, Y., Wang, Z., Qiu, W., Guo, Z., Liu, D., Qu, D., Xie, Z., Tang, H., and Li, J. (2018). Interfacing soluble polysulfides with a SnO2 functionalized separator: An efficient approach for improving performance of Li-S battery. Journal of membrane science *563*, 380-387.

157. Qi, M., Liang, X., Wang, F., Han, M., Yin, J., and Chen, M. (2019). Sulfur-impregnated disordered SnO2/carbon aerogel core–shell microspheres cathode for lithium-sulfur batteries. Journal of Alloys and Compounds *799*, 345-350.

158. Deng, Z., Zhang, Z., Lai, Y., Liu, J., Li, J., and Liu, Y. (2013). Electrochemical impedance spectroscopy study of a lithium/sulfur battery: modeling and analysis of capacity fading. Journal of The Electrochemical Society *160*, A553.

159. Cao, D., Sun, X., Li, Q., Natan, A., Xiang, P., and Zhu, H. (2020). Lithium dendrite in all-solid-state batteries: growth mechanisms, suppression strategies, and characterizations. Matter *3*, 57-94.

160. Zheng, F., Kotobuki, M., Song, S., Lai, M.O., and Lu, L. (2018). Review on solid electrolytes for all-solid-state lithium-ion batteries. Journal of Power Sources *389*, 198-213.